Characterizing the encoding of dynamical olfactory inputs in single olfactory sensory neurons to remote control larval chemotaxis by means of optogenetics

Aljoscha Schulze

TESI DOCTORAL UPF / 2015

Thesis Supervisor

Dr. Matthieu Louis

SENSORY SYSTEMS AND BEHAVIOUR
EMBL/CRG SYSTEMS BIOLOGY RESEARCH UNIT
CENTRE FOR GENOMIC REGULACION (CRG)

For Federica, Lorenzo and Luigi

Every solution of a problem raises new unsolved problems;
the more so the deeper the original problem and the bolder its solution.
The more we learn about the world, and the deeper our learning,
the more conscious, specific, and articulate will be our knowledge
of what we do not know, our knowledge of our ignorance.
For this, indeed, is the main source of our ignorance – the fact
that our knowledge can be only finite,
while our ignorance
must necessarily be infinite.

(Karl R Popper 1963)

(Conjectures and Refutations. Routledge & Kegan Paul New York)

Science does not rest upon solid bedrock. The bold structure of its theories
rises, as it were, above a swamp. It is like a building
erected on piles. The piles are driven down from above into the swamp,
but not down to any natural or 'given' base; and if we stop driving
the piles deeper, it is not because we have reached firm ground.
We simply stop when we are satisfied that the piles are firm enough to carry the structure,
at least for
the time being.

(Karl R Popper 1992)

(The Logic of Scientific Discovery. Routledge London, 1992)

Acknowledgements

I want to thank Matthieu Louis for his brilliant supervision, his sagacious advice, insightful criticisms, and patient encouragement that aided the success of my thesis work. Not afraid of helping me hands-on troubleshooting arduous experiments Matthieu has been an extraordinary mentor and teacher throughout the years. It has been an inspiring endeavor and I feel privileged having worked in such an open-minded and thought provoking atmosphere that fostered so much creativity. I want to thank Julia, David, Andreas, Mariana, Alex, Vani, Moraea, Sam, Bala, Daeyeon, Elena, Ibrahim, Ajinkya, Elie, Nicole, Avinash, and David T. for being inquisitive, thoughtful, critical, and creative, always ready to engage. Julia and David helped me lay the foundation of my thesis work through their support of the development of the extracellular recording technique — I want to thank them for that. I am grateful to Alex and Vani for the many years of fruitful collaboration that was ultimately awarded a long awaited happy ending. Thanks to Vivek Jayaraman whose repeated support of this project was greatly needed and deeply appreciated. I would like to acknowledge Parvez Ahammad whose coding skills enabled me to spike sort my electrophysiology data. Likewise I am grateful to Marco Musy who performed the parameter optimization of the IFF/IFB model. I would also like to thank Mariana Lopez-Matas for backing me up in my countless fly pushing efforts throughout the years and keeping my back free from the logistics of the lab. The members of my Thesis Advisory Committee, Mark Isalan, Hernán López-Schier, Cristina Pujades, David Robbe, and Timo Zimmermann have open-handedly given

their time and expertise to advance my work. I highly appreciate their involvement and am grateful for their support. Likewise, I want to thank the members of my PhD Defense Panel, namely Stefan Pulver, Cristina Pujades, and Jérôme Solon for critically reading this thesis. Thanks to Christian Petzsche who provided technical support towards the light stimulation setup. Thanks to Elena for her critical reading and constructive scrutiny of my Thesis. And thanks to Bala for incessantly stirring up my scientific vigor through his sparkling and contagious creativity. I want to thank the vivid CRG community that was always prepared to fuel tireless efforts and activities, making life at the CRG worthwhile and stimulating.

I am truly grateful to my parents and my family for their boundless support, love, and encouragement throughout all these years. Finally, I would like to thank all colleagues, students, and teachers who assisted, advised, and supported my research and learning efforts over the course of my work.

And last but not least I want to thank the Centre for Genomic Regulation for giving me the opportunity to pursue the research for my doctoral study at this most wonderful place.

Abstract

Animals have to deal with an environment presenting vast amounts of ever-changing sensory information. What features of this information flow are captured by the sensory system? My thesis work examines how signals experienced during free olfactory behaviors are processed by first-order olfactory sensory neurons (OSNs) of the *Drosophila* larva. By combining a novel extracellular recording technique with a microfluidics control system to control odor delivery in time and space, the computational principles underlying the encoding of dynamical odor stimuli were explored in a single OSN. An optogenetic approach was used to explore the OSN coding space and mimic naturalistic odor responses. The results described herein suggest that relative changes of the stimulus and their temporal integration are captured in a single OSN. Finally, larval behavior was characterized in closed-loop virtual odor environments and dissected with respect to the influence of dynamic features of the stimulus. It emerged that the neural activity of a single OSN is firmly correlated with dynamic features, notably the derivative of the stimulus intensity. These findings link the neural activity of single sensory neuron to behavioral transitions. Taken together, the results of this work provide an entry point into the understanding of larval action selection during chemotaxis.

Resumen

Los animales tienen que hacer frente a un entorno caracterizado por un flujo variable y abundante de información sensorial. ¿Qué rasgos de este flujo de información son capturados por el sistema sensorial? Este trabajo examina como las neuronas olfativas sensoriales de primer orden (NOS) de la larva de *Drosophila* procesan las señales experimentadas durante comportamientos olfativos incondicionados. Mediante la combinación de una novedosa técnica de grabación extracelular y un sistema de control de microfluidos que permite controlar temporal y espacialmente el suministro de olor, se exploraron los principios computacionales que permiten codificar los estímulos dinámicos de olor en una sola NOS. Para explorar el espacio que codifican las NOS y recrear una respuesta olfatoria naturalista se utilizaron técnicas de optogenética. Los resultados de este estudio sugieren que tanto los cambios de estímulos relativos como su integración temporal son capturados en una sola NOS. Por último, se cuantificó la conducta larval en entornos de olor virtual de bucle cerrado (closed-loop virtual odor environment) y se analizó teniendo en cuenta la influencia de las características dinámicas del estímulo. Del análisis resultó que la actividad neuronal de una única NOS está firmemente correlacionada con características dinámicas, en particular con la derivada de la intensidad del estímulo. Estos hallazgos ponen de manifiesto vinculan la actividad neuronal de una sola neurona sensorial con transiciones del comportamiento. En conjunto, los resultados de este trabajo proporcionan un punto de partida para

comprender la toma de decisiones de las larvas durante la quimiotaxis.

Preface

The survival of animals vitally depends on their ability to receive sensory information from their adjacent environment. To appropriately react to new sensory information animals constantly adjust their behavior. What features within the sensory information stream lead to changes in an animal's behavior?

This work focuses on the sensorimotor basis of a behavior performed by *Drosophila* larvae ascending an odor gradient. This behavior, called 'chemotaxis' has been described in various species, but the sensorimotor basis of this phenomenon has seldom been studied in naturalistic contexts. First, the sensory experience during chemotaxis is characterized in a single olfactory sensory neuron (OSN) of the *Drosophila* larva. Through well-controlled odor stimulations it is shown that an OSN can act as a differentiator through a combination of integral feedback and feed-forward regulation of olfactory transduction. By taking advantage of molecular tools in conjunction with optogenetics experiments in an olfactory virtual reality are conducted both behaviorally and electrophysiologically, which reveal that high firing rates of the OSN suppress turning, whereas low firing rates facilitate turning. Using a generalized linear model, light is shed on the question of how sensory activity modulates the probability of switching from a run to a turn. This work clarifies the link between computations carried out in single OSNs and action selection underlying navigation during larval chemotaxis.

A note on author contributions

This work, as it stands, would never have been possible without the generous support of numerous collaborators to whom I am truly and deeply indebted: all the modeling was done by Matthieu Louis (IFF/IFB, GLM), Alex Gomez-Marin (IFF/IFB, GLM), and Shaul Druckmann (GLM). Marco Musy and James Sharpe performed the Simplex parameter optimization of the IFB/IFF motif, Madhusudhan Venkadesan developed the model for the diffusion of the odor inside the behavioral arena, while Parvez Ahammad wrote the code of the spike sorting software. Julia Riedl was the first person to try out the suction electrode recording technique and David Jarriault assisted me in its optimization. Vivek Jayaraman helped me to write scripts for the PSTH analysis and assisted me in the setup of the tungsten electrode recording technique. The closed-loop larval tracker was developed through the joint efforts of Gus Lott (machine vision algorithm), Eric Trautman (tracker controller algorithm), and Chris Werner (hardware development). Vani Rajendran helped me with the development of the Labview code controlling the various stimuli: the liquid- and air-phase odor delivery systems and the LED controller. She also managed to get the tracker up and running and performed the first open-loop optogenetic experiments on it. A very fruitful phase of collaboration was finally crowned by the publication of the eLIFE paper in June 2015: 'Dynamical feature extraction at the sensory periphery guides chemotaxis' (see Appendix for the full reference information).

Theory and Introduction

Why this work is not about plants: Animals and their need for sensory coding

Unlike plants, animals are able to actively move and explore their surroundings, without the need to grow extra branches. The combination of these animal-specific, self-induced movements can be characterized as behavior. In order to accomplish nature's most crucial task — survival — while moving and behaving, it is essential for each animal to assess the correct context for every type of behavior at all times. The context for every behavior, however, is in permanent flux, given the dynamic world it inhabits. A new danger (i.e. a predator or a falling rock) lurking behind a corner certainly provides a catastrophic change of context for a foraging animal. Thus, animals have to quickly assess changes of the context to react adequately and immediately to alterations in their immediate environment. On the surface this appears a seemingly impossible task given the multitude of possible stimuli to be tracked at all times. To accomplish an adequate reaction in all situations, animals thus need a system that allows them to interrogate their environment in not one, but multiple ways simultaneously to obtain trustworthy multi-dimensional information about it — in a timely manner. For multicellular organisms[1], nature's invention to solve this problem is known as the nervous system (Hill, Wyse et al. 2012) which is able to provide real-time information about the environment with varying degrees of complexity tailored to the specific needs of a

[1] All multicellular animals except sponges have neurons and nervous systems (Hill, Wyse et al. 2012).

given species. Yet not only does the nervous system gather real-time information from its environment and thus provides the context for all behaviors, it is also able to efficiently transport this information distance beyond the single cell level — a feature essential for multicellular organisms, where different cellular compartments are too far away from each other as to allow for communication based on diffusion alone. Similar to other biological systems, the nervous system seems to have evolved towards ever-increasing complexity over time, culminating in 86 billion neurons found in the average human brain (Herculano-Houzel 2009), a number that is still topped by the 251 billion neurons residing in an elephant brain (Herculano-Houzel, Avelino-de-Souza et al. 2014). This number is close but still significantly smaller than there are stars in our galaxy (Voytek 2013).

The sensory nervous system allows an animal to detect cues from its surroundings via a multitude of sensors or receptors, which are embedded in respective information channels, called sensory neurons. Each sensory neuron can be categorized with respect to the physical modality (or modalities) it is tuned to; temperature, mechanical stimulation (i.e. touch), electromagnetic radiation (i.e. light), sound, and volatile chemicals (odors). In humid environments even more specialization is going on: A wide variety of sensors have tuned their bandwidth towards the detection of various modalities confined to the liquid space: dissolved chemicals (taste), pH, CO_2, and humidity to name only a few amongst the most prominent (Grant 1996; Waldmann 1997; Clapham 2003).

When taking a broader perspective on sensory systems among the different species that populate our planet, it seems obvious that the

characteristics of a sensory system a given animal processes are highly customized to fit its individual behavioral capabilities in the context of its natural habitat. It is this recurrent feedback that an environment exerts on an organism's specialized neural subsystems (and the organism as a whole), which has allowed those same systems to evolve among a path of ever-increasing efficiency, flexibility, adaptability, and robustness (Csete 2002).

Although neurons themselves are intrinsically electrical in nature, it is important to emphasize that information transmitted across the nervous system is subject to extensive modulation by chemical signaling cascades, namely second messengers, and hormones to name only a few (Restifo and White 1990). Also, the communication amongst individual neurons happens mainly via distinct classes of chemical synapses, each class speaking a different neurotransmitter language. With neurotransmitters themselves being highly conserved across the animal kingdom, their employment within a given nervous system has been shown to vary greatly for across phyla (Ryan and Grant 2009). In insects, opposed to mammals, signals captured by the sensory system are propagated chiefly through cholinergic synapses (Masse, Turner et al. 2009), while synapses within the motorneurons appear to be mainly glutaminergic (Mahr and Aberle 2006).

Neural networks can be described as hierarchical structures, where the term hierarchy is meant to refer to a repeated encapsulation of smaller elements of neural networks in larger ones (Kaiser, Hilgetag et al. 2010), an organization often described as recursive or fractal (Sporns 2006). Sensory neurons send information they receive from

their surroundings (periphery) towards higher order neural hubs, where the signal is processed and split up towards different locations up in the neural hierarchy. Upon arrival at higher neural processing centers, external stimuli from various sensory modalities are integrated and compared with intrinsic sensory cues such as hunger or thirst (Marella, Mann et al. 2012). Through this process, the nervous system is able to establish the context that gives the animal the opportunity to adequately react to a given stimulus. Parts of the higher processing centers are also capable of memorizing relevant context specific information over various time scales. The tuning curve[1] of sensory neurons (Butts DA 2006), although largely species specific, can vary wildly depending on developmental or even seasonal factors. Another common theme among sensory systems is the high degree of adaptation[2] they illustrate, a property allowing them to provide a meaningful response over a broad intensity range. Yet, what are the features among the ever-changing flow of sensory information that are captured by the sensory system? How do sensory systems process information they obtain from their environment and how does this information modulate an animal's behavior? My thesis work addresses these questions by firstly analyzing freely moving larvae in a controlled odor environment to record behaviorally relevant odor concentration time courses. A representative odor time course was subsequently presented in electrophysiological experiments aiming to measure the corresponding OSN activity. The characterized neural activity was

[1] A *tuning curve* represents the average firing rate of a neuron as a function of relevant stimulus parameters (Butts DA 2006).
[2] *Sensory adaptation* is a change over time in the responsiveness of the sensory system to a constant stimulus (en.wikipedia.org/wiki/Neural_adaptation).

then reproduced by means of optogenetics and tested behaviorally in freely moving larvae navigating light induced virtual odor environments.

Throughout time, sophisticated olfactory systems have evolved to track temporal changes in the concentration of volatile odorant molecules — food odors, pheromones associated with the presence of conspecifics and substances signaling danger. Research on larval olfaction can be traced back to the Dutch scientist Jan Swammerdam who documented the behavior, anatomy, and life-cycle of the cheese fly larva *Piophila casei* already in the 17th century (Cobb 1999). However, during the past century, research in the fruit fly *Drosophila melanogaster* gained more and more momentum, culminating in *Drosophila* becoming one of the most studied model organisms in biology (Beckingham, Texada et al. 2005) *Drosophila's* success story may at least in part be attributed to it being a small, fast growing, and short lived animal with a relatively simple nervous system (Bellen 2010; Stephenson and Metcalfe 2013). At present, a rich genetic toolbox allows for an unprecedented genetic dissection of *Drosophila's* neural circuits, as is most prominently accomplished by the famous GAL4-UAS expression system — in some cases down to the level of single neurons (Luo, Callaway et al. 2008; Jenett, Rubin et al. 2012; Pfeiffer, Truman et al. 2012; Brand 1993).

Although *Drosophila* larvae possess an even simpler nervous system – comprising a total of less than 10,000 neurons (Nassif, Noveen et al. 2003) — they are capable of orchestrating an extraordinary repertoire of complex behaviors (Louis, Phillips et al. 2012). Their sensory system is well equipped to detect a wide variety of physical

dimensions such as light, smell, heat, taste, touch, and humidity. While larvae are strongly avoiding light stimuli detected by their visual system, it appears as though they are strongly attracted by odors detected by the olfactory system. In fact, they display a very stereotypic pattern of olfactory-guided orientation maneuvers allowing them to efficiently allocate food sources from a distance, as one would expect of an animal that literally eats all day long. Also, the *Drosophila* larval olfactory system seems to share the basic architecture not only with its adult counterpart but also with mammals (Gerber and Stocker 2007). Perhaps more surprisingly, larvae have been shown to perform Pavlovian conditioning — a learning process in which an innate behavioral response to a potent stimulus is elicited in response to a paired previously neutral stimulus (Pauls, Selcho et al. 2010; Eschbach, Cano et al. 2011; Galili, Ludke et al. 2011; Wessnitzer, Young et al. 2012). Contrary to adult flies, larval behavior, since they do not fly, is mostly limited to two spatial dimensions. Tracking of larvae is therefore a less complex task and can be readily automated. The combination of these features renders the *Drosophila* larva a perfect model organism to address the question of quantitative sensory coding at the peripheral sensory system.

Odor detection and foraging strategies among different species: From bacteria to multicellular organisms.

The detection of physical stimuli is by no means confined to complex multicellular organisms. All living cells are in some way

sensitive to chemicals in their immediate environment — a predisposition that likely led to the eventual evolution of specific receptor proteins, which later became the building blocks of ever more complex chemosensory organs of multicellular organisms (Ache and Young 2005).

Orientation in response to chemical cues can be classified into two major categories: *taxis* when the organism is capable of directional changes directly correlated with the stimulus, and *kinesis* (from ancient Greek κίνησις (kinesis), meaning 'movement, motion') when the organism undergoes directional changes in response to a stimulus, resulting in a reorientation towards a random direction. Organisms performing kinesis, although they exhibit no direct bias towards the stimulus source, over time tend to accumulate closer to the source of an attractive substance. This effect can be characterized as an emergent indirect bias of the organism towards the source. Bacteria have been shown to efficiently track chemical gradients by performing klinokinesis (from ancient Greek κλίνω (klino), meaning 'to bow, to incline one's self'). In doing so, they implement a strategy of straight swimming phases — called *runs* — interrupted by distinct, random changes in orientation — called *tumbles*. The overall reorientation rate has been shown to be governed by the nutrient concentration (Berg 1972). In spite of its simplicity, this orientation algorithm produces efficient gradient ascents through a biased random walk.

In the nematode *Caenorhabditis elegans*, a numerically simple neural network transforms odor information into orientation behavior. It was proposed that *C. elegans*' orientation behavior employs an

improved random walk search strategy to locate an attractive odor source (Pierce-Shimomura 1999). It was later discovered that chemotaxis in *C. elegans* is in fact a combination of kinesis and weathervaning[1] (Bargmann 2006; Iino and Yoshida 2009; Lockery 2011), a taxis control mechanism involving continuous correction of the orientation during runs (Iino and Yoshida 2009; Izquierdo and Lockery 2010).

Contrary to *bacteria* and *C. elegans*, many animals are equipped with even more sophisticated motor functions. The behavioral strategy that is enabled by this staggering increase in complexity is referred to as *taxis* and allows for a directional response to a given stimulus (from ancient Greek τάξις (taxis) meaning 'arrangement') (Kendeigh 1961). However, the term '*taxis*' is ambiguous, since it refers to different facts depending on the context of its use: Taxis behaviors are either defined according to the biophysical modality a given organism responds to (i.e chemotaxis, thermotaxis, or phototaxis)[2], or with respect to the means a sensory organ processes sensory stimuli. Examples following the latter definition of taxis are tropotaxis, which describes a strategy of an organism continuously comparing information detected via its bilateral sensory organ to infer the direction of a concentration gradient, and klinotaxis, which refers to a behavioral strategy of an organism receiving information from many sensory inputs that actively sample the environment to determine the strongest change in concentration. Apart from the

[1] *Weathervaning* refers to 'runs' during chemotaxis being slightly bent towards the direction of higher concentration (Iino and Yoshida 2009; Gomez-Marin and Louis 2014).
[2] One example of this ambiguity the term '*bacterial chemotaxis*', which refers to a behavior that can be more accurately described by the term *chemoklinokinesis*.

necessity to sense a change in concentration, animals performing klinotaxis also require some kind of memory, which allows them to continuously carry out successive comparisons of the present stimulus environment with the past stimulus environment (Gomez-Marin, Duistermars et al. 2010; Gomez-Marin and Louis 2012). To perform tropotaxis, memory is no prerequisite since concentration differences are compared spatially among different sensors, which renders temporal comparisons optional.

When following an appetitive smell, *Drosophila* larvae, not unlike humans, mice, or dogs, actively seek for cues guiding them to the source of the stimulus. Larval chemotaxis could thus be more accurately defined as chemoklinotaxis, since animals actively sample an odor gradient to locate the odor source (Gomez-Marin and Louis 2012; Gomez-Marin and Louis 2014).

How to control odor environments to study the interplay of sensory input and behavior

To embark upon the question of peripheral sensory coding it is indispensible to get a handle on the quantitative (naturalistic) stimulus time course that an animal experiences during unconstrained behavior. In the past, the ability of adult flies to measure minute differences between concentrations measured at their left and right antennae was tested in a miniaturized treadmill coupled to a customized olfactometer (Borst 1982). More recent solutions involving airborne olfactory stimuli mixed in laminar airflows have broadened the understanding of how rapidly changing odor stimuli are encoded by the peripheral olfactory sensory system of adult flies (French, Torkkeli et al. 2011; Gershow, Berck et al. 2012; Martelli, Carlson et al. 2013; Szyszka, Gerkin et al. 2014). To date, the creation of a tightly controlled odor environment remains a challenging task given the diffusible, and often turbulent nature of airborne odor stimuli (Vetter, Sage et al. 2006). However, previous work established a solution to this problem by allowing *Drosophila* larvae to behave in a static odor gradient formed by the diffusion from single odor droplets in an enclosed arena (Louis, Huber et al. 2008). The airborne concentration profile inside the arena was quantified by infrared spectroscopy and fitted to numerical simulations. Individual larval trajectories were subsequently mapped onto the odor profile to obtain the actual odor-stimulus-intensity-time-course for individual animals. Using this approach it was found that the duration of runs is strongly modulated by the sensory experience the larva undergoes: the average perceived change in

odor concentration before a turn steadily declines from an increasing concentration to a decreasing concentration. This observation was found to be valid for numerous odors over an ample range of concentrations (Gomez-Marin, Stephens et al. 2011; Gomez-Marin, Partoune et al. 2012). The time derivative of the stimulus is continuously normalized by the stimulus concentration,

$$\frac{1}{C} \times \frac{dC}{dt}.$$

As a result, runs heading towards the stimulus are elongated while runs heading away from the stimulus are shortened. In addition, larvae are able to distinguish spatial odor concentration information to such an extent as to accurately turn to the side of higher odor concentration first (Gomez-Marin and Louis 2012). A correction mechanism similar to weathervaning (similar to *C. elegans*) has also been shown to fine-tune the orientation of individual runs towards the stimulus (Gomez-Marin and Louis 2014; Ohashi, Morimoto et al. 2014). Interestingly, larval mutants, having only one pair of a functional single olfactory sensory neuron (OSN), exhibit no deficit in locating the odor source[1] by means of active sampling when compared to their wild type counterpart (expressing all 21 OSNs). Even animals expressing only one unilateral single OSN are able to locate the source, however, with a slight overall decrease in the accuracy of gradient sensing (Louis, Huber et al. 2008). These findings suggest that the signal encoded by one pair of OSNs transmits enough information to direct orientation of *Drosophila* larvae in an odor gradient.

[1] Note that single OSN functional larvae are only able to detect a limited subset of odors when compared to their wild type counterparts.

The mechanistic hypotheses about the control of larval chemotaxis outlined above (Gomez-Marin and Louis 2012; Gomez-Marin and Louis 2014), however, still lack a quantitative neural model of the underlying olfactory processing.

From sensory coding to behavior (and vice versa): An example of sensorimotor integration.

What features among the ever-changing flow of sensory information are captured by the sensory system? And how does this information modulate an animal's behavior?

What makes the assessment of sensory-motor systems challenging is the fact that the stimulus and its neural representation are naturally intertwined with an animal's interaction with its physical environment. The sum of all these interactions can be summarized as recurrent behaviors which ultimately close the sensory control loop by the generation of a continuous stream of sensory feedback (Fry, Rohrseitz et al. 2008). In the case of larval olfaction, a continuous olfactory stimulus is actively generated through a series of behavioral patterns, which are referred to as chemotaxis. To understand the neural representations, transformations, and circuit dynamics underlying the sensorimotor phenomena of chemotaxis, it has been proposed to characterize the transfer properties — i.e. how the neural representation of olfactory stimuli is transformed into behavior — to infer the systems' structure–function relationships (Huston and Jayaraman 2011).

When focusing on the neural activity aspect, it was found that in insects as in mammals, behaviorally relevant temporal relationships

of neural representations of sensory inputs could be simplified down to a dual principle:

(1) a rate or phase code where the firing or spike timing of OSNs is related to the odor concentration (Hopfield 1995; Abraham, Spors et al. 2004; Masse, Turner et al. 2009), or the temporal sequence of the response relative to some clock signal (i.e., stimulus onset);

(2) a combinatorial principle where increasing intensities of an odor either recruit the activity of more OSNs (Malnic and Hirono 1999; Wilson and Mainen 2006), or cause changes of the timing of neurons with respect to each other in a population (e.g., synchrony, neuronal activation sequences) (Bathellier 2010).

Although this combinatorial principle (2) has been shown to apply to the *Drosophila* larva, where increasing intensities of an odor recruit the activity of an increasing number of OSNs (Kreher, Kwon et al. 2005; Gerber and Stocker 2007; Kreher, Mathew et al. 2008; Asahina, Louis et al. 2009), past work has revealed that a combinatorial principle is by no means essential for chemotaxis: the information contained in a single pair of OSNs is sufficient to guide *Drosophila* larvae to the source of an odor gradient in a manner undistinguishable from wild type (WT) larvae (Fishilevich, Domingos et al. 2005; Louis, Huber et al. 2008; Asahina, Louis et al. 2009).

To successfully dissect sensorimotor systems, it is most useful to commence by characterizing the transformation of behaviorally relevant stimuli (stimuli experienced during free, naturalistic

behavior) into a neural response (stimulus to neural). In a second step recurrent behavioral transitions are modeled as the function of the neural response time course (neural to behavior). Huston and Jayaraman suggest to further simplify this approach by assuming the olfactory-to-motor integration to be a largely feed-forward process, with sensory inputs being transformed by successive banks of spatial and temporal filters (Huston and Jayaraman 2011).

Detailed studies of the signal transduction cascade underlying bacterial chemotaxis have demonstrated that even a single cell can compute temporal changes in the concentration of chemical stimuli. This mechanism relies on nearly perfect sensory adaption (Shimizu, Tu et al. 2010), which permits the cell to track changes in stimulus intensity over several orders of magnitude and achieve robust gradient ascents (Lazova 2011). OSNs in *C. elegans* have been shown to fire specifically to either positive or negative changes in concentration (Chalasani, Chronis et al. 2007; Lockery 2011) However, in adult *Drosophila*, single OSNs can extract much more complex features associated with the dynamics of olfactory stimuli. Here, the firing rates follow the time derivative of the stimulus in an analog manner over wide concentration ranges (Kim, Lazar et al. 2011; Szyszka, Gerkin et al. 2014). This analysis led Kim et al. to propose that fly OSNs operate according to an adaptive neural encoder.

Neurons are limited in the resolution (frequency range) with which they are able emit spikes. Therefore, a reduction in the response to sustained stimuli could serve to decrease the redundancy of a rate coded signals (Tkačik and Bialek 2014). In adaptation the relation

between the magnitude of the signal and a neuron's firing rate is changed. As a result, a sensory neuron is rendered relatively insensitive to small fluctuations of the background intensity without compromising its ability to encode larger fluctuations. In other words, adapted responses bear a strong resemblance to responses to lower odor concentrations. In the visual system of the blow fly it was found that the magnitude of the rescaling selected by the adaptation process optimizes information transmission (Brenner, Bialek et al. 2000). It was proposed that this optimization is largely achieved through the context dependence in the neural code that is established on an apparently continuous range of timescales from tens of milliseconds to minutes (Fairhall, Lewen et al. 2001). In the end, there may be multiple neural codes operating simultaneously at different temporal scales, with each code carrying complementary information (Fairhall, Lewen et al. 2001). Such multiplexed codes could provide several computational advantages, such as reducing the ambiguity inherent to single-scale codes and enhancing robustness of neural representations to environmental noise (Panzeri, Brunel et al. 2010).

Dissecting larval chemotaxis: Behavioral repertoire, behavioral classification

When observing larvae navigating in an odor gradient, there can be no doubt that they are efficiently making their way to the highest odor concentration. Larvae crawl forward with peristaltic (rhythmic) head and body movements. From time to time they stop to swing

their head around, rapidly sampling their immediate surrounding, to resume crawling into a new direction. Although larval behavior during chemotaxis is very complex with regards to the various motor programs coordinating crawling, peristalsis, and head movements all at the same time, the overall search behavior appears to be relatively simple when studied in greater detail. Previous work, by using a high-resolution single animal-tracking algorithm, established that only a small number of behavioral classifiers are sufficient to account for a large part of the behavioral repertoire during chemotaxis. Reported behavioral categories include straight runs, stops, turns, and episodes of active head casting (sampling) preceding a turn (Figure 1) (Gomez-Marin, Stephens et al. 2011; Gomez-Marin and Louis 2012).

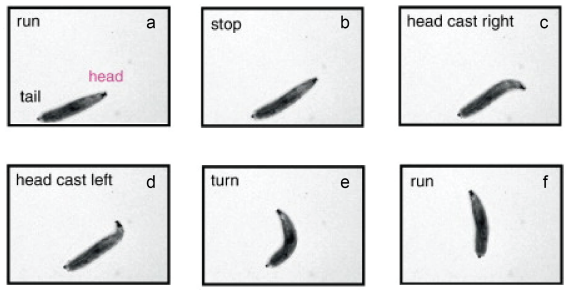

Figure 1. Top view of larval body posture changes as seen during chemotaxis. A larva is seen to interrupt its run (a) to stop (b), sample right (c), sample left (d), turn (e), and start a new run (f). Pictures courtesy of Balaji Iyengar, adapted from Gomez-Marin and Louis 2012.

The transition between the different behavioral categories is governed by changes in the odor-stimulus-time-course immediately preceding a transition event (see previous section). A prolonged

decrease in the perceived odor concentration at the timescale of several seconds triggers an animal to stop (type I decision: when to turn) and quickly sample its environment at a sub-second timescale (type II decision: which side to turn to), followed by a turning event in the direction of increasing concentration (~70% success rate) (Figure 1) (Gomez-Marin, Stephens et al. 2011; Gomez-Marin and Louis 2012).

This work's main focus lies on the control of the duration of a run (type I decision), a behavioral mechanism common to bacteria, *C. elegans* and *Drosophila*. This behavior is ideally suited to study how dynamical changes in odor concentration can be used to regulate whether an ongoing run is maintained or a turning maneuver is initiated.

The larval olfactory system's architecture

How does the sensory system achieve the transmission of information from the periphery to higher processing centers in the brain?

The main structure of the olfactory system is fairly conserved among all insects and in its core architecture (Figure 2) it is very similar to the vertebrate olfactory system. Chemical stimuli enter the larval chemosensory system bilaterally via the dorsal organ — a tiny, balloon-like structure at the tip of the larval head. The dome, containing the profuse dendritic tree of 21 OSNs, forms the center of the dorsal organ. It is perforated at its base and also its cuticular wall contains many pores through which odorants can enter the

sensillum lumen to make contact with olfactory dendrites (Chu and Axtell 1971; Singh 1984). Odorant binding proteins present in the hemolymph of the dome are thought to be involved in the uptake and transport of hydrophobic odorant molecules through the sensillum lymph (Steinbrecht 1997). The 21 sensory neurons protrude the dome in 7 bundles of triplets, which host the 25 olfactory receptors. Binding of the odorant molecule to the receptor leads to activation of the OSN in the form of spikes. The dendrites of each OSN express mostly one type of odorant receptor (OR) in conjunction with the *odorant receptor co-receptor* (*Orco*) (Larsson, Domingos et al. 2004; Bargmann 2006; Benton, Sachse et al. 2006). The cell bodies of the sensory neurons are located inside the dorsal ganglion (Singh 1984; Python and Stocker 2002; Stocker 2008). Being the source of all OSNs, the dorsal organ is widely regarded as the equivalent of the vertebrate nose. Embedded in this structure, OSNs form the peripheral layer within the olfactory system serving to convert chemical stimuli from the environment into electrical signals. Each of the 21 OSN axons targets a unique glomerulus[1] each of which represents a segregated anatomical structure within the larval antennal lobe (AL). The AL embodies a complex sensory relay circuitry and is often referred to as the insect-equivalent to the vertebrate olfactory bulb.

[1] *Glomerulus* is a common term used in anatomy to describe globular structures of entwined vessels, fibers or neurons. 'Glomerulus' is the diminutive of the Latin *glomus* meaning 'ball of yarn' (en.wikipedia.org/wiki/Glomerulus).

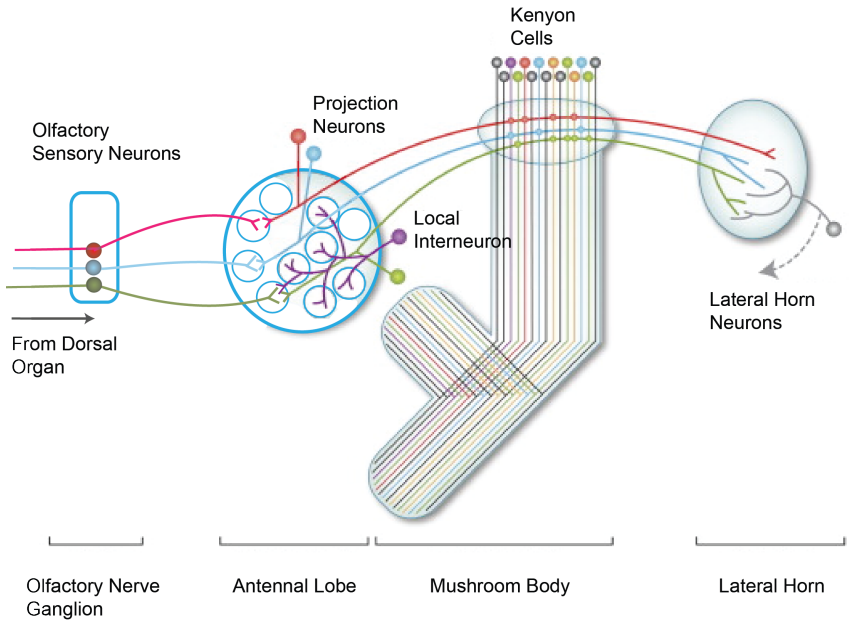

Figure 2. Schematic Representation of the Olfactory System of the *Drosophila* larva (adapted from Cachero and Jefferis) (Cachero and Jefferis 2008).

In each glomerulus a single OSN forms synapses with the second layer neurons of the olfactory system — projection neurons (PNs), which pass the information on to higher brain centers, and local interneurons (LNs), which distribute information among glomeruli for purposes of signal enhancement and gain control (Masuda-Nakagawa, Gendre et al. 2009) (Figure 2). LNs are a heterogeneous cluster of neurons interconnecting a large number of heterogeneous neurons within the antennal lobe (Das, Sen et al. 2008). In *Drosophila* larvae it has been shown that lateral inhibition between glomeruli is mediated by GABAergic inhibitory local interneurons (iLNs) (Asahina, Louis et al. 2009). In the adult fly additional subpopulations of LNs have been characterized. Here, in addition to

lateral inhibition and gain control, signal amplification is reported to happen by excitatory local interneurons (eLNs) (Shang, Claridge-Chang et al. 2007). A recent study suggests an even more complex framework of connectivity within the antennal lobe of the adult *Drosophila*: It reports that part of the adult glutaminergic LNs (Glu-LNs) may in fact inhibit GABAergic LNs (GABA-LNs), while excitation of PNs is solely achieved through electrical coupling of LNs to PNs (Yaksi and Wilson 2010). In contrast, Glu-LNs are reported to directly inhibit not only PNs, yet also GABA-LNs, thus disinhibiting PNs. Inhibition in such a network topology is achieved on different spatial and temporal scales. The authors suggest that this functionality could allow for more robust gain control and rapid transitions between network states akin to the wiring of many cortical circuits in vertebrates where corecruitment of excitation and inhibition is a common motif (Liu 2013). There, it was reported that the recruitment of interneurons via feedforward and/or feedback excitatory projections leads to inhibition proportional to local and/or incoming excitation (Isaacson and Scanziani 2011). In this context, the right balance of these two opposing synaptic conductances appears to play a crucial role in maintaining proper cortical function (Isaacson and Scanziani 2011).

In contrast to the abundant connectivity shared with LNs, most AL glomeruli are connected to only one single PN (although a few PNs form connections to more than one glomerulus (Das, Gupta et al. 2013)), each of which makes contact with hundreds of Kenyon cell dendrites at the level of the mushroom body (MB) calyx, the neuronal substrate underlying olfactory learning and memory

(Ramaekers, Magnenat et al. 2005) (Figure 2). PNs also project to the lateral horn, a distinct region in the brain involved in the orchestration of innate behaviors (Stocker 1994; Marin 2002; Luo, Axel et al. 2010; Ruta, Datta et al. 2010).

The full receptor repertoire of the larval olfactory system has been thoroughly functionally characterized in the past most notably by (Kreher, Kwon et al. 2005). Olfactory receptors show a predominantly excitatory response to a specific chemical; in fewer cases responses have been shown to be inhibitory. While some receptor neurons respond to a wide array of different odorants, others appear to be more narrowly tuned, sensitive to only a small number of odorant molecules. The sensitivity to an individual odorant varies greatly between different odor receptors, and the response dynamics of various odor responses seem to be different in both duration and onset kinetics as well. With higher odor concentration, more and more receptors become activated (Hallem and Carlson 2004; Kreher, Kwon et al. 2005; Hallem and Carlson 2006). However, as mentioned previously, a concerted activation of different OSNs is not indispensable to guide gradient ascent during larval chemotaxis (see 'How to control odor environments to study the interplay of sensory input and behavior').

The transformation of a chemical into an electrical signal: Olfactory transduction in ORs

'To transduce' means to convert something from one form into another. In the context of odor transduction it describes the process of transforming a chemical signal of odorant molecules into an electrical signal travelling along a neuron.

Electrical activity within neurons consists of the movement of ions through channels embedded in neuronal surface membranes. The major charge carrying ions are sodium (Na^+), potassium (K^+), chloride (Cl^-) and calcium (Ca^{2+}). The surface membranes of neurons are primarily composed of lipids, which pose an efficient barrier to the ionic flow. The ability of ion channels to enable ion flow is most prominently governed by the electrical potential that exists across the membrane, the gradient of ions set up by membrane pumps, and the semi permeable nature of the channels. In *Drosophila*, as in most other higher organisms, electrical information within a neuron travels in the form of spikes. A spike is generated once the membrane potential of a neuron passes a certain threshold (depolarization) thus activating a critical number of voltage-sensitive ion channels. The recruitment of these ion channels leads to an abrupt and transient change of membrane voltage that propagates to other neurons via the long cellular protrusion called axon (Izhikevich 2007). The voltage dependence of channel opening (activation) is steep and sigmoidal, as determined in voltage clamp studies where membrane potential is the only parameter varied (Jan and Jan 1989). In their pioneering studies, Hodgkin and Huxley proposed that this steep voltage

dependence arises from three or four voltage-sensitive components that function as voltage sensors that are embedded within the membrane (Hodgkin and Huxley 1952). Over time, it became clear that a voltage change exerts an electrostatic force on these voltage sensors triggering conformational changes that result in a channel opening (Jan and Jan 1992; Jiang, Lee et al. 2002; Long, Tao et al. 2007). The movements of charges intrinsic to the cation channels (gating current) have since been examined electrophysiologically and have been modeled extensively (Armstrong 1981; Jan and Jan 1989; Hille 2001).

In vertebrates olfactory transduction starts from a G-protein-coupled seven-transmembrane odorant receptor, which transduces the message via a complex multilayered metabotropic signaling cascade in a rather slow manner — typically on the order of 100 ms (Bhandawat 2005; Shusterman, Smear et al. 2011). In contrast, olfactory transduction in insects works differently and happens at a much faster time scale with a response latency of only 10 ms (Nagel and Wilson 2011). Although the overall transduction process is still largely unknown, some parts of this complex puzzle have started to emerge. The short response latency observed in insects may be attributable to an ionotropic[1] component speeding up the overall transduction process. As a result, invertebrates compared to vertebrates encode odors up to 10 times faster (Bhandawat 2005; Nagel and Wilson 2011). Similar to vertebrate olfactory receptors, *Drosophila* ORs are seven-transmembrane proteins (Benton, Sachse et al. 2006), which were originally thought to be G-protein coupled

[1] *Ionotropic receptors* are 'ligand-gated transmembrane ion channels' (interactive-biology.com/3974/ionotropic-vs-metabotropic-receptors/).

receptors. However, they exert an inverted membrane topology, an intracellular N- and an extracellular C-terminus allowing them to function as ligand-gated ion channel (Benton, Sachse et al. 2006; Lundin, Käll et al. 2007). In insects, odorant receptors (ORs) are not functional all alone; instead they need a co-receptor — *Orco* — that is necessary for both localization and stabilization of ORs in dendritic membranes, and the formation of the OR-*Orco* complex — a functional odorant-gated cation channel mediating the ionotropic signal transduction (Sato, Pellegrino et al. 2008). In addition to the primary response, it has been suggested that either G-protein-mediated potentiation or modulation of the ionotropic response could be taking place. Insect ORs may thus represent a distinct class of receptors belonging to both ionotropic and metabotropic receptors. However, there seems to be no evidence for an ionotropic *Orco*-based mechanism of pheromone transduction in *Manduca sexta* (Stengl 1994; Nolte 2013), raising the question whether the finding that *Orco* acts as an ionotropic receptor is truly universal to all insects (Sato, Pellegrino et al. 2008; Nichols, Chen et al. 2011; Pask, Jones et al. 2011; Nakagawa, Pellegrino et al. 2012). Second messengers such as cyclic nucleotides or inositol (1,4,5)-trisphosphate (IP3) establish a link of the metabotropic part of the olfactory transduction to *Orco*. In adult *Drosophila* IP3 has been shown to act on *Orco* indirectly via the inositol (1,4,5)-trisphosphate receptor ($InsP_3R$) (Murmu, Stinnakre et al. 2010) whereas cyclic adenosine monophosphate (cAMP) levels within the OSN appear to be positively correlated with an increase in neural activity exclusively in the presence of *Orco* (Deng, Zhang et al. 2011). The discussion on whether *Orco* functions via an ionotropic or metabotropic activation

implies that a combined activation of both pathways (ionotropic and metabotropic) could contribute to the olfactory transduction cascade in single OSNs (Wicher, Schäfer et al. 2008; Nakagawa and Vosshall 2009; Wicher 2010; Martin 2011; Stengl and Funk 2013; Wicher 2013).

The fact that the physiology of olfactory adaptation in insect OSNs looks qualitatively similar to the adaptation seen in vertebrate OSNs hints towards the notion that a metabotropic signaling cascade might directly contribute to modulating the odor response in insects (Shirsat and Siddiqi 1993; Hildebrand and Shepherd 1997). In this context, it seems that calcium is playing a key role mediating a negative feedback (Berridge 1995) causing olfactory adaptation in numerous species (Matthews and Reisert 2003). In *Drosophila*, it has been proposed that a change in Ca^{2+} levels affects both onset of and recovery from adaptation through a yet unknown Ca^{2+} channel present in the membrane of olfactory neurons (Deshpande 2000). In amphibians[1] crucial components of the Ca^{2+} signaling cascade in sensory neurons have already been identified for years (Leinders-Zufall, Rand et al. 1997; Leinders-Zufall, Greer et al. 1998; Leinders-Zufall 1999; Zufall and Leinders-Zufall 2000; Munger, Lane et al. 2001). Here, Ca^{2+}/ calmodulin-dependent protein kinase II (CaMKII) plays a role in determining the temporal response properties of ORNs during odor adaptation. However, only adaptation induced by sustained odor pulses was impaired by an inactivation of CaMKII, whereas adaptation induced by brief odor pulses was not. The study concluded that different kinetic forms of

[1] Experiments done in tiger salamanders.

odor adaptation exist in single ORNs which are likely controlled by separate molecular mechanisms (Leinders-Zufall 1999). In *Drosophila*, although many results hint towards the presence of a multi-layered, mixed ionotropic and metabotropic transduction cascade (Wicher, Schäfer et al. 2008; Nakagawa and Vosshall 2009; Wicher 2010; Martin 2011; Stengl and Funk 2013; Wicher 2013), the overall mechanism of odor transduction remains still open.

The manipulation of neural systems by synthetic optical actuators: Optogenetics

Channelrhodopsin-2 (ChR2) is a light-gated, non-selective cation channel in the single-cell green alga *Chlamydomonas reinhardtii* that has become an important tool in neuroscience paving the path to an entirely new field — referred to as optogenetics (Dugue, Akemann et al. 2012). ChR2 conducts H^+, Na^+, K^+, and Ca^{2+} ions. In contrast to olfactory receptors, which form heterodimers with the co-receptor *Orco*, channelrhodopsin channels are homodimeric (Muller, Bamann et al. 2011; Kato, Zhang et al. 2012). Similar to ORs, they are ionotropic, seven transmembrane proteins, and they likely do not couple to a heterotrimeric G-protein (Nagel, Szellas et al. 2003; Kato, Zhang et al. 2012). Instead, they contain the light-isomerizable chromophore all-*trans*-retinal[1], allowing for an extremely fast response time. ChR2 is most efficiently activated by blue light at an absorption maximum of 480 nm (Figure 3).

[1] To render ChR2 functional in *Drosophila* larvae, all-*trans* retinal has to be added to the fly food since insects are unable to synthesize all-*trans*-retinal on their own.

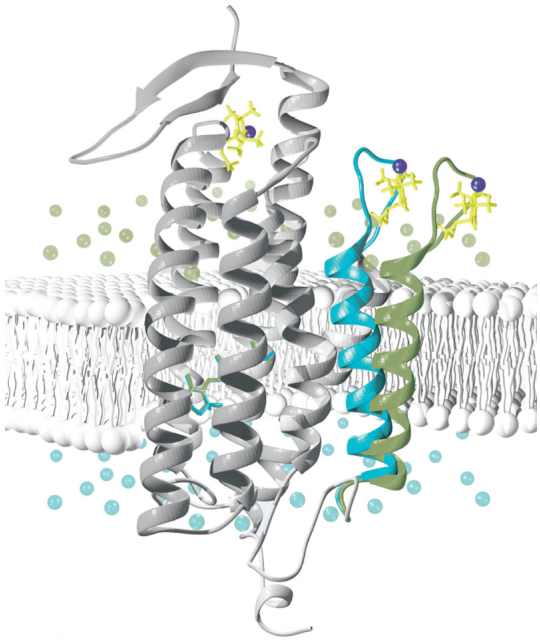

Figure 3. A channelrhodopsin-2 molecule before and after exposure to light: The protein's amino acid chain forms an α-helix measuring seven times the diameter of the cell membrane. When exposed to incident light, helix 2 (cyan) twists out (green), opening the ion channel for calcium (green spheres) and sodium ions (cyan spheres). In the middle of the channel, the small, photo-sensitive retinal (green/cyan) is bound to the protein Image courtesy: (Sattig 2013).

Once the all-*trans*-retinal complex absorbs a photon, a short-lived conformational change is elicited which transiently opens the pore of the channel. As a result, cations surge through the channel, depolarize the neuron and evoke spikes (Muller, Bamann et al. 2011; Kato, Zhang et al. 2012).

ChR2 can be expressed in virtually any cell type in vertebrates and invertebrates to serve as a light switch triggering the firing of neurons in a highly controlled manner (Schoenenberger, Scharer et al. 2011).

In contrast to the difficulty of creating tightly controlled odor environments, optogenetics offers an alternative way to reverse engineer odor stimuli through the creation of controlled virtual light environments. In the *Drosophila* larva, a virtual reality environment has been successfully applied to elicit basic innate olfactory behaviors (Bellmann, Richardt et al. 2010), as well as associative olfactory memory (Schroll, Riemensperger et al. 2006; Honda, Lee et al. 2014). In adult flies, it was exploited to investigate the use of bilateral comparisons between left and right antennae (Gaudry, Hong et al. 2013). In *C. elegans* optogenetics was used to evoke genuine orientation behavior by modulating the activity of interneurons in the neural pathway that controls chemotaxis (Kocabas, Shen et al. 2012).

At present there exist many modified forms of ChR2 with enhanced characteristics for research purposes. The ChR2 version used for this project — ChR2-H134R (Pulver, Pashkovski et al. 2009) — carries a single point mutation at position H134 and displays increased photocurrents, a modest reduction in desensitization, and a slight increase in light sensitivity compared to the wild-type (Nagel, Brauner et al. 2005; Berndt, Schoenenberger et al. 2011; Lin 2011) ChR2. The off kinetics of ChR2-H134R with 18 ms is slightly slower compared to the wild type version of ChR2 (Yizhar, Fenno et al. 2011).

In this project, instead of using pulsed light to evoke neural activity in one OSN through ChR2, the light intensity itself was used as a proxy to simulate changes in odor concentration detected by one OSN. Since the maximum neural activity elicited by light is slightly

lower than the one elicited by an odor it was important to adjust the odor concentration range to be in good agreement with the light stimulation. The reverse engineering of olfactory activity was achieved through stimulation protocols at an intensity range of 15-207 W/m^2, an intensity level allowing for a neural activity reminiscent of real odor responses (Kocabas, Shen et al. 2012) (see 'Results section; Neural firing and adaptation: Dose response').

Chapter 1 - Materials and Methods

Physiology

Extracellular recordings of single OSNs (suction electrode recording technique)

Every multi cellular organism relies on the well-controlled propagation of signals within and among cells or cellular compartments, a task that is widely accomplished through means of chemical messengers. However, chemical signals come with the caveat that they are limited in the temporal resolution they can achieve. It is electrical activity that solves this problem by facilitating a rapid flow of information among spatially separate cell populations of cells within complex organisms. In order to listen to the content of these fast electrical signals we need to intercept the message at cells that are specialized in performing this task — the neurons.

By measuring the membrane potential of a neuron one can listen in to the electrical message transmitted within it — typically in the form of spikes. However, even in non-spiking neurons of *C. elegans* one can record the passive propagation of the electrotonic potential. Measuring the membrane potential is achieved through electrophysiology — the study of the electrical properties of biological cells and tissues. Electrophysiology is all about measuring voltage changes or electric currents on a wide variety of scales, but it is most prominently applied in the context of action potential activity of spiking neurons. The simplest of all electrophysiological

recording techniques are extracellular recordings. Here, tiny extracellular signals arising from the flow of an ionic current through the extracellular fluid are recorded via a chlorinated silver wire inside a fine glass electrode that is backfilled with extracellular saline.

In the past several groups have successfully recorded odor responses in the larval olfactory system: Oppliger et al. used a drawn out glass capillary with a 1 um closed tip which was back-filled with Kaissling sensillum lymph ringer as the recording electrode. They inserted the electrode at the rim of the dome of the dorsal organ or in the terminal organ, whereby the tip of the electrode broke on entry and the recording was initiated (Oppliger, P et al. 2000). Kreher et al. took a comparable approach where they recorded the extracellular electrical activity of sensory neurons by inserting an electrode into the lumen of the dome sensillum (Kreher, Kwon et al. 2005). A similar method was also used by (Hoare, McCrohan et al. 2008).

To probe the response properties of a single OSN, a new extracellular recording technique based on the suction of the antennal nerve into a glass pipette downstream from the dorsal organ (DO) ganglion was developed in collaboration with Julia Riedl and David Jarriault (Figure 4). This approach enables the acquisition of excellent extracellular recording data with a low signal to noise ratio. However, since it is essential to keep the recording electrode immersed in a saline bath, it is necessary to deliver odor stimuli in the liquid-phase.

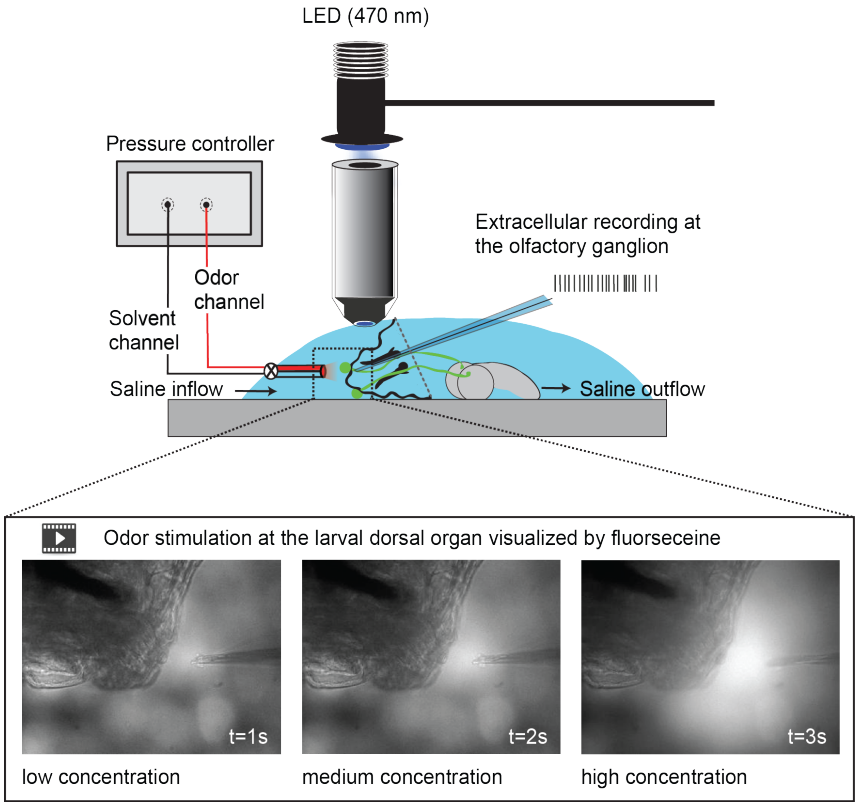

Figure 4. Illustration of the preparation used for suction electrode recordings of single functional OSNs expressing channelrhodopsin (ChR2). The preparation is bathed in saline to prevent the dehydration of the dorsal organ ganglion to which the recording electrode is attached. Controlled odor stimulations are achieved in liquid phase with a customized mass-flow controller system.

Larvae (3rd instar) expressing the co-receptor *Orco* in only one OSN (*Or42a*-Gal4>Orco) were raised on standard fly food containing 0.5 mM all-*trans*- in an incubator in complete darkness. Prior to the dissection they were transferred into 15% (w/V) glucose solution washing them free of food. The larval dissection was carried out in

cold extracellular saline (Singleton and Woodruff 1994)[1] on a Sylgard coated petri dish. The larval head was dissected away from the body using a 3 mm Vanna spring scissor (Fine Science Tools, Germany) leaving the brain intact and attached to the head. A small amount of tissue glue (Histoacryl, B. Braun, Germany) was applied onto the round glass cover at the bottom of a small volume perfusion chamber (Bioscience Tools, USA) using a pulled glass pipette. Remaining saline was carefully dipped off the head before it was glued centric onto the glass slide. A drop of saline was immediately added on top of the larval head to avoid dehydration. The cuticle covering the mouth hook was carefully removed using the above mentioned Vanna spring scissors to allow the recording electrode access to the dorsal organ ganglion. In addition, the dorsal organ itself was now perfectly visible allowing for a precise positioning of the odor delivery pipette. The perfusion chamber containing the larval head immersed in extracellular saline was connected to two syringe pumps (Aladdin2-220, World Precision Instruments, USA), to ensure the perfusion of the prep with extracellular saline and to continuously clear odor molecules out of the chamber. To preserve the integrity of the preparation, the DO was maintained in a saline solution and odors were presented in liquid phase.

In close vicinity of the dorsal ganglion the antennal nerve was sucked into the recording pipette by applying a negative pressure of -20 kpa. Recordings were performed in 'current clamp' mode where

[1] Composition of external saline according to Singleton and Woodruff 1994:
108 mM NaCl, 5 mM KCl, 2 mM CaCl2, 8.2 mM $MgCl_2$, 4 mM $NaHCO_3$, 1 mM NaH_2PO_4, 5mM trehalose, 10 mM sucrose, 5 mM HEPES [pH 7.5, 265 mOsm].

the membrane potential is free to vary, and the amplifier records whatever voltage is resulting from action potential generated by the neurons inside the suction electrode. Recording electrodes were pulled (P97, Sutter instruments, USA) out of glass capillaries (1.5mm / 1.12mm OD/ID, World Precision Instruments, USA) with a 10 um open tip and back-filled with 3 uL extracellular saline. The recording electrode was connected via a chlorinated silver wire (0.38 mm in diameter) to a head stage (Axon MultiClamp 700B, Molecular devices, USA), mounted on a micromanipulator (ROE-200 & MPC-200, Sutter instruments, USA), which in turn was connected to a microelectrode amplifier (Axon MultiClamp 700B, Molecular devices, USA). The signal was amplified 100×, visualized on an oscilloscope (Tektronix, USA), and recorded at a sample rate of 20 kHz in a PC equipped with the free data acquisition software SpikeHound (Lott III 2009).

In the extracellular recordings single spikes could be readily detected due to a strongly reduced spontaneous activity of OSNs in the *Orco* null background (Hoare et al., 2008). However, also non-olfactory sensory neurons are likely to contribute to the activity monitored from the DO ganglion. In addition to the co-receptor *Orco*, channelrhodopsin 2 (ChR2) was expressed in the single functional OSN (Pulver, Pashkovski et al. 2009). Brief light flashes were applied to elicit ChR2-evoked spikes in a nearly deterministic manner within the *Or42a* OSN, providing the wave-form template for the spike-sorter (Figure 5). The spike-sorting step ensured that only spikes originating from OSNs were included in the dataset, while non-OSN specific spikes were filtered out (see 'Materials and

Methods section; Data acquisition, analysis, spike sorting, and spike yield analysis'). Odor ramps with controlled temporal features were produced with an olfactometer mixing two aqueous flows — pure saline and saline mixed with isoamyl acetate (IAA) — directed onto the dorsal organ. Both flows were mixed in complementary proportions while maintaining the resulting flow constant at all times (see 'Materials and Methods section; Odor stimulation in liquid-phase). This setup similar in design to past olfactometers (Borst 1982) (Kim, Lazar et al. 2011) was designed to produce aqueous stimulus time course on the timescale of a typical run.

Data acquisition, analysis, spike sorting, and spike yield analysis

The extracellular signal obtained from the antennal nerve was amplified 100×, visualized on an oscilloscope (Tektronix, USA), and recorded at a sample rate of 20 kHz in a PC equipped with the free data acquisition software SpikeHound (Lott III 2009). A custom Matlab based spike-sorting algorithm (OpSIN) developed and written by Parvez Ahammad was used to analyze the extracellular recording data obtained from single-electrode recordings. The spike-sorting algorithm is based on the finding that waveforms of light-driven spikes and odor-driven spikes elicited in the OSN are indistinguishable from each other while spikes originating from non-OSN neurons correspond to waveforms with a waveform that is distinct (Figure 5C). In every recording, precisely timed short-latency light-driven spikes were used to elicit activity in the *Or42a*>ChR2 OSN. During this light stimulation phase the

OpSIN algorithm parsed the extracellular recording data and collected candidate ChR2-evoked spikes based on simple amplitude thresholding and local non-maximum suppression (Figure 6).

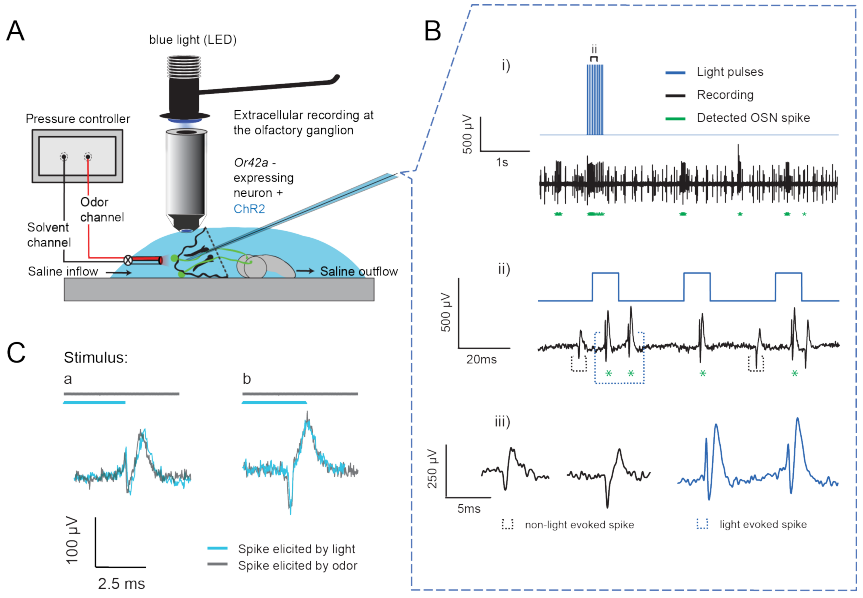

Figure 5. (A) Illustration of the preparation used for suction electrode recordings of single functional OSNs expressing channelrhodopsin (ChR2). The preparation is bathed in saline to prevent the dehydration of the dorsal organ ganglion to which the recording electrode is attached. Controlled odor stimulations are achieved in liquid phase with a customized mass-flow controller system.

(B) ChR2-triggered activity observed in an *Or42a*-expressing olfactory sensory neuron (OSN) in response to brief pulses of blue light (10 ms) shown at an increasing temporal resolution (Bi-Biii).

(C) Superimposition of light- and odor-evoked spike waveforms observed in the same OSN (two different recordings in a and b). Spike waveforms associated with the light stimulation intervals (blue spikes) were superimposed on spike waveforms of spikes collected during an odor stimulation episode (gray spikes). Although light- and odor-evoked spike waveforms are very similar to each other during the same recording, the overall shape of the spike waveforms varied across recordings.

All spikes collected during this process were clustered into groups of similar waveforms using an affinity propagation algorithm (Frey and Dueck 2007). From these clusters, the experimenter identified the cluster containing the highest number of spikes as the one representing the template waveform specific to the OSN of interest (corresponding solely to ChR2-evoked activity) (Figure 5B). For the spike sorting process template spike waveforms derived from ChR2-evoked spike clusters were then used to identify OSN specific spikes throughout the entire recording. This spike selection was accomplished by comparing candidate waveforms identified throughout the recording to the ChR2 derived waveform template by transforming candidate waveforms to appear as similar as possible to the template via dynamic time warping (Berndt and Clifford 1994). The residual difference between the warped candidate and the original template was taken as the pair-wise distance between the two waveforms. Finally, the probability of spike occurrence at every candidate location was estimated by warping the residual distance between the candidate waveform and the chosen set of spike templates. A spike-probability-histogram-based cut-off was applied across the entire recording to select the correct spikes and assign identities.

$$d(T,X) = \sqrt{\left(X - DTW(T \rightarrow X)\right)^2}$$

A spike-probability-histogram-based cut-off was applied across the entire recording to select the correct spikes and assign identities.

$$p(T, X_i) = e^{\left(\frac{d(T,X_i)}{K}\right)}$$

where K is the median of all the pair wise distances computed across the set of spike-candidates.

$$p(T) = \max\left(p(T, X_i)\right)$$

where the spike candidate's probability is based on its best matched template.

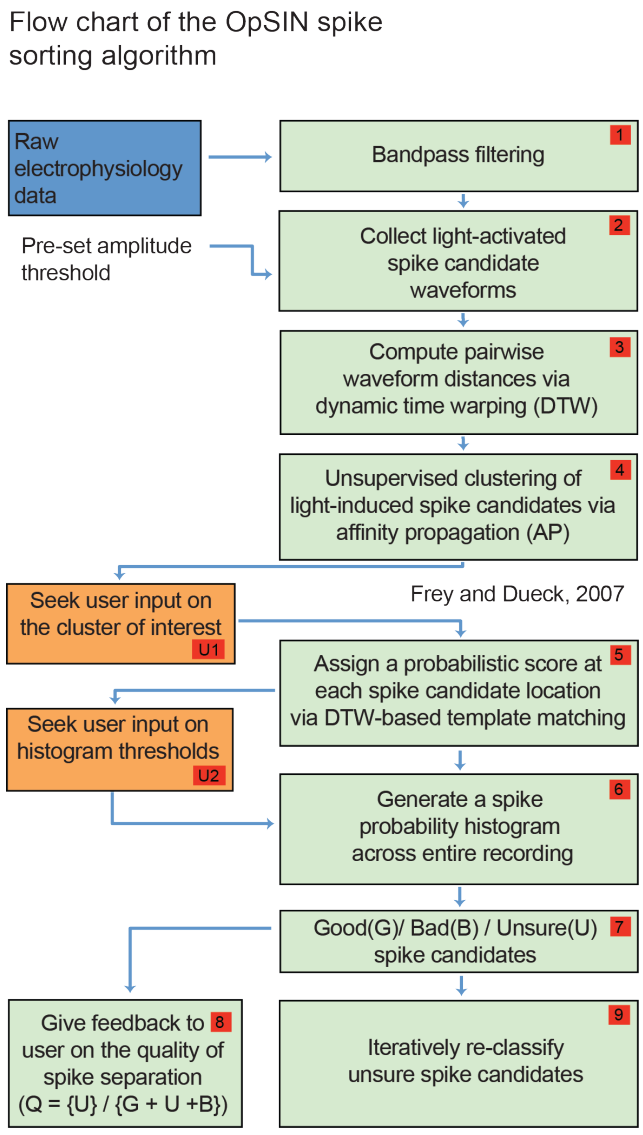

Figure 6. Flow chart of the functions underlying the spike-sorting algorithm. Spike candidates were selected during light-activation episodes based on simple amplitude thresholding and local non-maximum suppression. Spike selection was accomplished by comparing candidate waveforms identified throughout the recording to the ChR2-derived waveform template by transforming candidate waveforms to appear as similar as possible to the template via dynamic time warping (DTW).

To quantify ChR2 driven neural activity of the OSN, the spike yield of animals (*Or42a*-Gal4>UAS-Orco,UAS-ChR2-H134R;*Orco*$^{-/-}$) raised with retinal was compared to the yield of those raised in normal food without added retinal (negative controls) by analyzing a total of 35 recordings for either case. However, due to the lack of light evoked activity in the OSNs of the controls that were raised in normal food, the recording in this condition was started with short odor pulses, which served to elicit OSN specific activity. Template spikes in the control condition were thus collected during the odor stimulation phase.

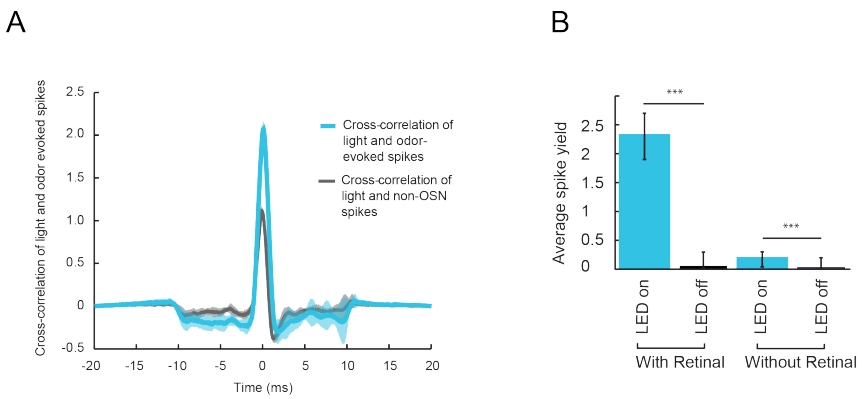

Figure 7. (A) Cross-correlation of light- and odor-evoked spikes (blue), and cross-correlation of light-evoked to spontaneous background spikes (gray). The similarity in the shape of the waveform is larger between the light- and odor-evoked spikes compared to light-evoked and background spikes. Light-evoked spikes were collected from time windows during a light stimulation interval; odor-evoked spikes were collected during the odor stimulation interval; background spikes were collected from intervals devoid of light and odor stimulations.

(B) Average spike yield of the *Or42a*-expressing OSN measured in a 58ms time window with and without light stimulation. The data was obtained by analyzing 35 recordings.

The spike yield for the light-stimulation condition was obtained by analyzing the time window during which blue light was pulsed (33 ms pulse duration) plus a 25 ms cushion after the light pulse was switched off (total time window of analysis was 58 ms). In the non-stimulation case, the 58 ms time window was chosen right before the onset of the light stimulation.

Figure 7B illustrates the spike yield during the light stimulation in animals raised in all-*trans* retinal food compared to animals raised in normal fly food. The spike yield during the light stimulation window was found to be 2.30 +/- 0.40 spikes in animals raised in the presence of all-*trans* retinal. The corresponding spike latency was 6.96 ms +/- 1.02 ms. For the negative controls (animals raised in normal fly food) the spike yield during the light stimulation window was found to be 0.17+/-0.13 spikes a value significantly different from the positive controls (Wilcoxon signed-rank test, $p<0.001$). The corresponding spike latency was 33.08 ms +/- 13.67ms. The corresponding instantaneous firing rate during the time window of analysis during a light flash was found to be 39.61 Hz for the positive controls and 2.91 Hz for the negative controls. During a light flash, animals raised in food containing all-*trans* retinal show a 13.53 fold increase in spike yield compared to the negative controls.

In the absence of light stimulation the spike yield of animals raised in all-*trans* retinal food was 0.057 +/- 0.24 spikes. For the negative controls (animals raised in normal fly food) the spike yield in the absence of light was 0.029 spikes +/- 0.17 spikes. The instantaneous firing rate during the time window of analysis without any light stimulation was found to be 0.98 Hz for the positive controls and

0.49 Hz for the negative controls. In the absence of light, animals raised in food containing all-*trans* retinal showed a two-fold increase in the spike yield compared to negative controls.

Comparing the spike yield during light stimulation to the non-stimulation condition it was found that animals raised in all-*trans* retinal food showed a 79.31-fold increase from the non-stimulation to the light stimulation case, while negative controls showed a mere six-fold increase from the non-stimulation to the light stimulation case (Figure 7B).

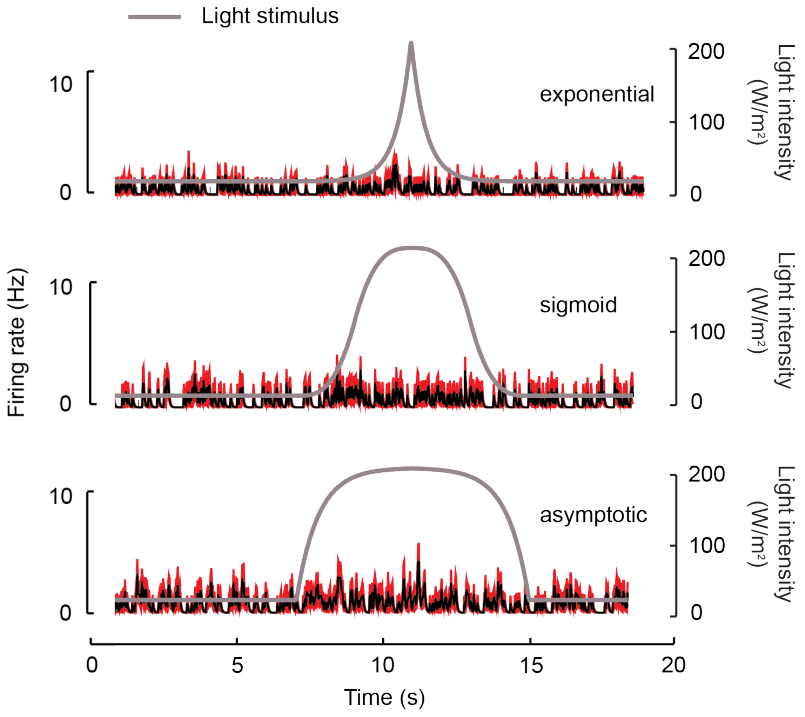

Figure 8. OSN activity in response to three light ramps recorded in larvae raised in the absence of all-*trans* retinal. The absence of all-*trans* retinal renders the OSN non responsive to light.

Thus, a noticeable light sensitivity seems to be present even in larvae raised in normal fly food without retinal added to it (negative controls). However, in those animals the light response was much less pronounced compared to the light response observed in the positive controls. In fact, when comparing the magnitude of the change of the spike yield, the observed change was 13.22 times greater for the positive control compared to the negative control. Figure 8 illustrates the firing rate recorded in OSNs of larvae raised in fly food lacking all-*trans* retinal. Here, the observed OSN activity remained reasonably constant throughout the light stimulation phase.

Peristimulus time histogram (PSTH) analysis

A peristimulus time histogram (PSTH) is an analysis tool used to transform discrete spiking events into a continuous representation of neural activity in the form of a frequency. This frequency or instantaneous firing rate depends on the average inter-spike-interval (ISI) — the time, which passes between two individual spiking events — within a certain time window of analysis. Individual spikes from a continuous spike train are collected into fixed time bins over which the average spike frequency is subsequently calculated. The time window or bin size over which the average spike frequency is calculated has to be chosen carefully. A small time window will allow assessing the frequency almost instantaneously, in that it will at the minimum only depend on the spike preceding and following the a given spike. However, since spikes are fundamentally

stochastic events (Lecar and Nossal 1971; Lecar and Nossal 1971), the resulting frequency will be very noisy (the lower the frequency — the noisier). A large bin size on the other hand will smoothen out small differences of the individual ISIs resulting in a less noisy spike frequency.

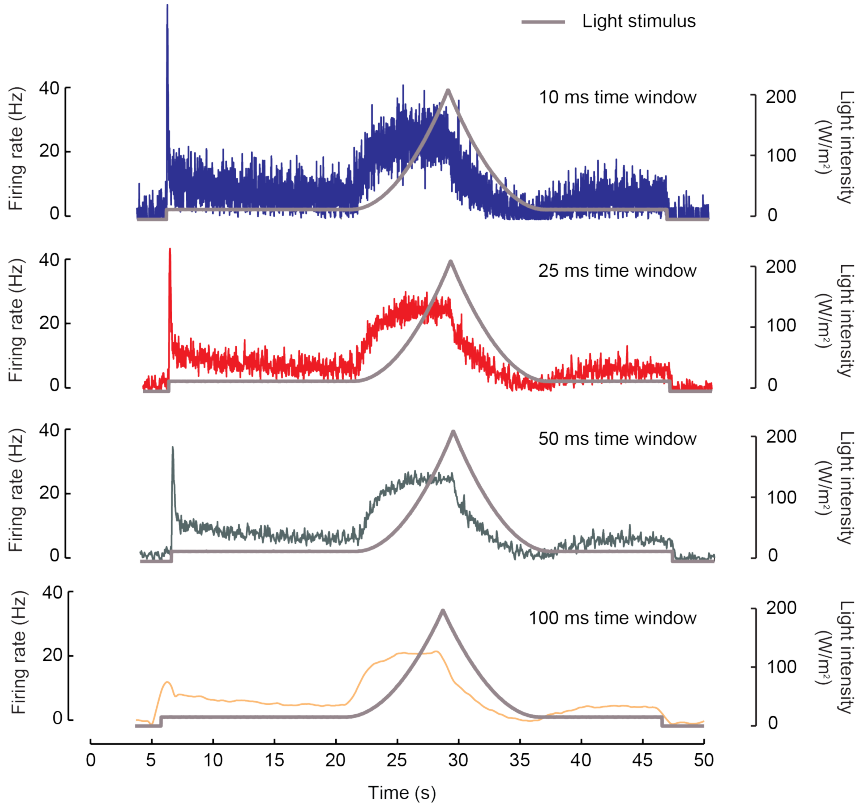

Figure 9. OSN response to a quadratic light ramp analyzed with bin sizes of different durations ranging from 10 ms, 25 ms, 50 ms, and 100 ms. Based on this analysis the bin size was set to 50 ms. The PSTH was computed on a pool of minimum 10 recordings conducted on minimum 10 preparations.

Here, an average is calculated on the basis of a larger number of spikes. In this work the optimal bin size for the PSTH analysis was assessed experimentally. A sample dataset (quadratic light stimulation) with bin sizes of different durations ranging from 10 ms, 25 ms, 50 ms, and 100 ms was analyzed. From Figure 9 it can be seen that the calculated spike frequency from a bin size of 10 ms fluctuates greatly resulting in a very noisy spike frequency. However, with increasing bin sizes the resulting spike frequency becomes less noisy. It was found that by the using a 50 ms time window the noise level of the resulting spike frequency was at acceptable levels. Also, by using a 50 ms bin size, the overall resolution of the spike train (25 Hz) was kept close to the sampling rate of stimulus (30 Hz).

To reduce the overall noise level of the final firing data, the PSTH was mildly low-pass filtered using a Savitzky-Golay filter (3rd degree, over 21 frames), which is based on a local least-squares polynomial approximation. A Savitzky-Golay filter provides the advantage of reducing noise while maintaining the shape and height of waveform peaks resulting in smoothing without loss of resolution (Press 1988; Schafer 2011).

Light stimulation: setup and calibration

For the light stimulation a blue light emitting diode (LED) (LCS-0470-03-22, Mightex Systems, Canada) was mounted in a lighthouse (U-DULHA, Olympus, Japan) and integrated into the light path of the microscope (BX51, Olympus, Japan) allowing for localized

stimulation of the larval head through a 40x immersion objective. The light intensity arriving at the larval head was estimated by measuring the photocurrent under the objective with a photodiode (SM05PD7A, Thorlabs) connected to a bench top photodiode amplifier (PDA200C, Thorlabs). The active area of the photodiode was 4.8 mm^2 while the spectral responsivity of the photodiode at 470 nm was provided by the manufacturer of the photodiode as

$$0.09\ \frac{A}{W} \text{ at } \lambda{=}470 \text{ nm.}$$

The diameter of the in focus light spot was measured to be 1 mm. The photocurrent arriving at the larval head was determined to be 270 uA. The area of the in focus light spot was calculated accordingly.

$$A = \pi(0.5\ mm)^2 = 0.7854\ mm^2$$

The measured photocurrent (I_{rig}) was then converted into units of light intensity (W/m^2).

$$Light\ Intensity = \frac{I_{rig}}{0.09\ \frac{A}{W}}$$

The transformation function at the electrophysiology rig (driving voltage (V) to light intensity (W/m^2)) was obtained from the calibration curve shown in Figure 10A. At the electrophysiology rig, the LED was controlled by a custom Labview (National Instruments, USA) interface. The current controlling the LED was fed into the data acquisition software, where it was recorded along with the signal from the suction electrode.

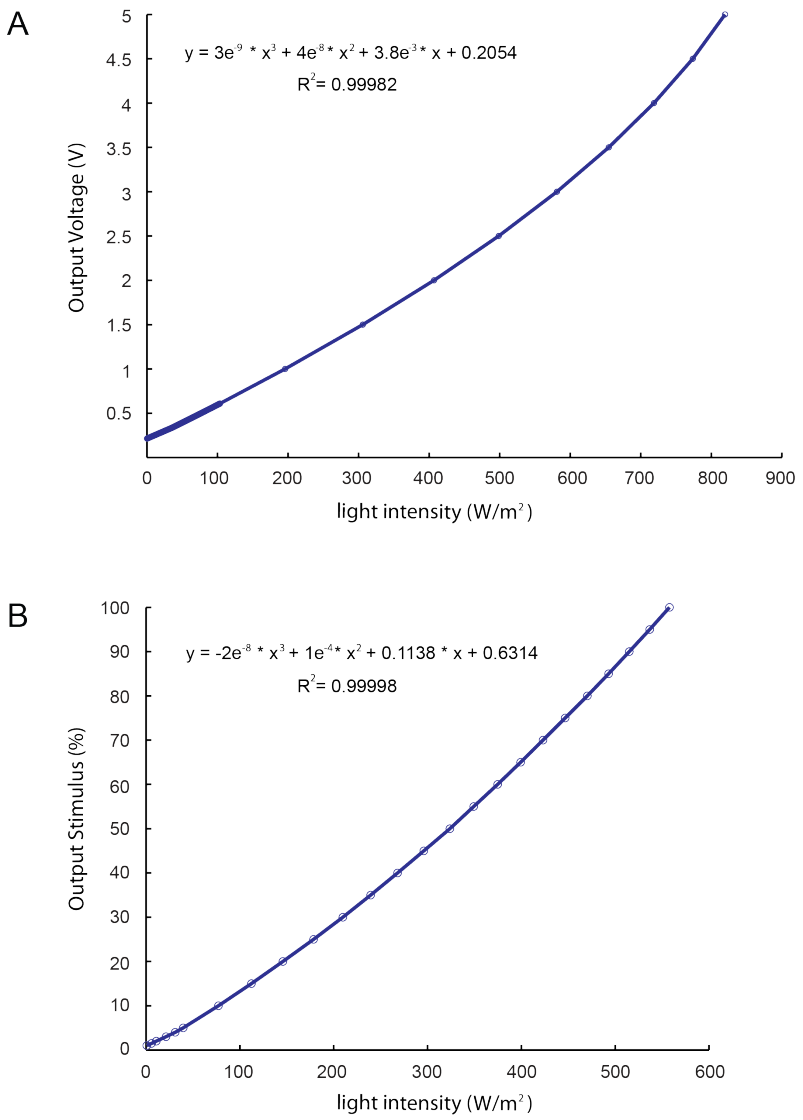

Figure 10 Light calibration and polynomial transfer function at the electrophysiology rig (A) and the larval tracker (B).

At the larval tracker, the photodiode was placed in equal distance to all LEDs in plane with the tracking arena and placed in the spot of the highest light intensity at a driving current of 750 mA while keeping the light beam of each LED focused onto the measurement plane. The calibration curve obtained at the larval tracker (stimulus (%) to light intensity (W/m^2)) is shown in Figure 10B. The light intensity range used for behavioral and electrophysiological experiments ranged from 15 - 207 W/m^2. This intensity range was established by analyzing the elicited activity level of the *Or42a* OSN over a broad spectrum of light intensities (see 'Results section; Neural firing and adaptation: Dose response').

Odor stimulation in liquid-phase

The objective for the odor delivery system was to generate rapidly fluctuating odor time courses on a fixed larval preparation. The resulting odor stimulation replay had to be quantitatively and temporally and reminiscent of what a larva would experience during chemotaxis in real odor gradients. The limiting factor of this approach was set by the sample rate of the pressure-driven flow controller, which reached its maximum at 10 Hz.

The final odor concentration used at the electrophysiology rig was taken from animals behaving in an odor gradient (unconstrained behavior). The concentration experienced by a larva during chemotaxis was mapped on the reconstructed odor gradient landscape and recorded over the time of the experiment. The resulting concentration time course was then transformed from air-

phase concentration values (uM) to liquid phase concentration values (uM) via a scaling factor that was obtained by quantitatively relating well-controlled air-phase and liquid-phase odor responses through means of functional imaging.

Two-barrel pipettes (1.5 mm / 0.84 mm OD/ID, World Precision Instruments, USA) were pulled using a PMP-107 Multipipette Puller (MicroData Instrument, USA) resulting in a two-barrel tip with a 5 μm OD. One barrel was back-filled with the odor solution (IAA dissolved in extracellular saline), the other with extracellular saline alone. An injection needle (0.51mm / 0.26mm OD/ID, Becton, Dickinson and Company, USA) was inserted into the back of each barrel and airtight sealed using hot-melt adhesive. Each barrel was subsequently connected to separate channels of a pressure-driven flow controller (Microfluidic Control System (MFCS), Fluigent, France). The tip of the odor stimulation pipette was placed and maintained at a distance of 10 um in front of the larval dorsal organ with a micromanipulator (ROE-200 and MPC-200, Sutter instruments, USA). The output pressure and with it the flow of each individual channel of the odor delivery pipette was controlled at a temporal resolution of 10 Hz via a custom Labview interface (National Instruments, USA). The Labview program allowed for an arbitrary control of the stimulus time course through individual pre-loaded input files (CSV files) that contained the corresponding pressure time course driving individual channels of the pressure-driven flow controller. The stimulus time course contained in the input file was either derived from reconstructed odor time courses of behaving animals or based on linear and non-linear functions

(depending on the objective of the individual experiment). Rapid concentration changes of the odorous stream were achieved by varying the flow between the empty channel and the odor channel while keeping the overall flow constant at a set value of 0.00032 mL/s (measured flow rate corresponding to a 320 mbar output pressure).

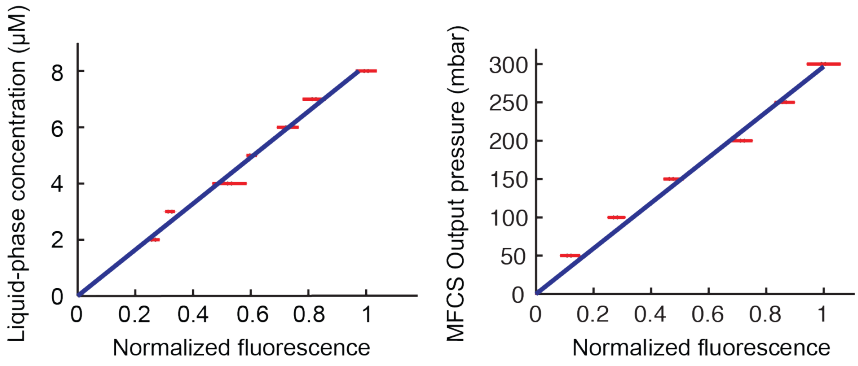

Figure 11. Calibration of fluorescein in liquid phase (left) showing a linear relationship of the fluorescein concentration and the measured change in fluorescence. The calibration on the right illustrates a linear relationship of the output pressure of the flow controller and the observed change in fluorescence. Error bars represent the standard deviation.

The liquid phase odor stimulation system was calibrated using a dilution series of the fluorescent dye fluorescein, which was expelled at a constant pressure

$$p_{max} = 320\ mbar$$

into a perfusion chamber (Bioscience Tools, USA) while imaging the tip of the pipette with a high-speed camera (Andor, United Kingdom).

The relationship between the fluorescein concentration and the measured fluorescence was best fitted by a linear function (Figure 11 left) where a denotes the slope of the function.

$$S_{fluores} = a * c_{Fluorescein}$$

When varying the output pressure while keeping the concentration of fluorescein constant (corresponding to $S_{fluores} = 1$ as determined in Figure 11 left) the observed fluorescence could be mapped to the output pressure using a linear function (Figure 11 right) where b denotes the slope of the function.

$$S_{fluores} = b * p_{Fluorescein}$$

The concentration arriving at the dorsal organ was quantified by comparing the fluorescence measured at the tip of the odor delivery pipette ($\Delta F(ROI_{tip})$ to the fluorescence measured right at the dorsal organ ($\Delta F(ROI_{dorsal})$. Assuming that the fluorescence measured at the tip of the odor delivery pipette represents the undiluted concentration, the dilution factor (d) was calculated according to:

$$d = \frac{\Delta F(ROI_{tip})}{\Delta F(ROI_{dorsal})}$$

Given that the overall pressure is kept constant at $p_{max} = 320\,mbar$ throughout the stimulation, the final concentration hitting the dorsal organ can be calculated according to:

$$c_{dorsal} = \frac{c_{pipette}}{d} * \frac{p_{odor}}{p_{max}}$$

where p_{odor} denotes the pressure of the odor channel. However, when comparing the pressure time courses of the odor and the solvent channel it became clear that the MFCS pump produced a small but notable departure from the ideal assumption that the overall pressure would be kept constant. During rapid transitions, the closing time of the valve seemed longer compared to its opening time. The resulting small alteration of p_{odor} and $p_{solvent}$ (pressure of the solvent channel) were therefore accounted for by using the real (measured) pressure of the odor and solvent channel for all time points as the basis of the final concentration calculation throughout the stimulation time course:

$$c_{dorsal} = \frac{c_{pipette}}{d} * \frac{p_{odor}}{p_{odor} + p_{solvent}}$$

In Figure 12 it can be seen that the departure of the concentration from the ideal conditions while almost absent for slow transients (Figure 12A shallow linear stimulation), slightly increases for very fast transients as seen for steep linear slopes (Figure 12B) and even more so for an exponential stimulation (Figure 12C). Comparing the adjusted output signal (the same as the one shown in Figure 12C) to the measured fluorescence for the most drastic change in concentration — the exponential stimulation — leads to a decent fit, indicating the relevance of considering the pump's departure from ideal conditions (Figure 12D) when analyzing the final stimulus time course truly hitting the larval dorsal organ.

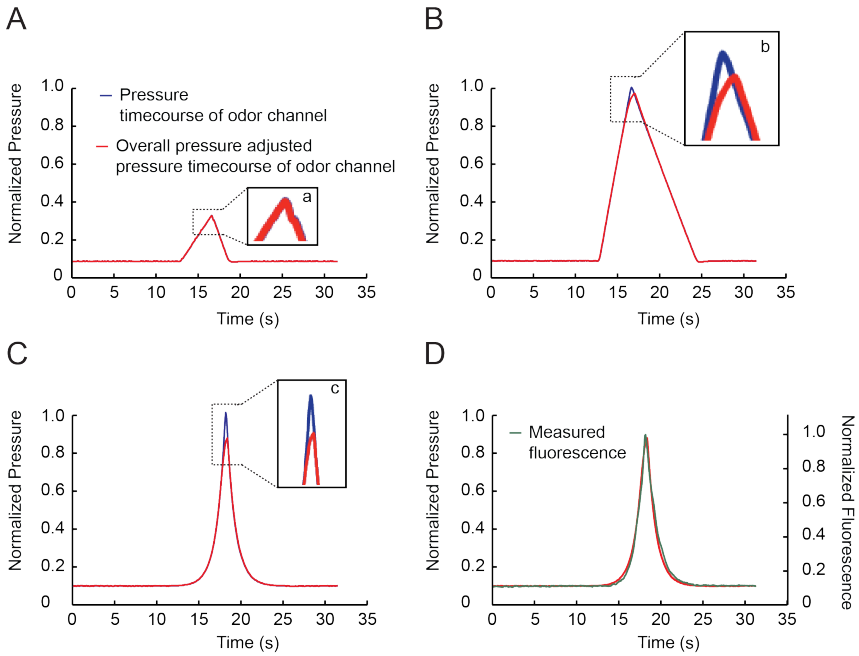

Figure 12. (|A) Normalized ideal (blue) vs. normalized adjusted (red) concentration time course of a shallow linear ramp. In this example, the adjusted concentration time course is almost identical to the ideal time course (see close-up view in inlet a).

(|B) Normalized ideal (blue) vs. normalized adjusted (red) concentration time course of a steep linear ramp. The adjusted concentration time course departs slightly from the ideal time course (see close-up view in inlet b).

(C) Normalized ideal (blue) vs. normalized adjusted (red) concentration time course of an exponential stimulation. The adjusted concentration time course departs from the ideal time course (see close-up view in inlet c).

(D) Normalized adjusted odor time course (red) compared to the measured change in fluorescence (green).

The time lag between the pressure output and the actual odor stimulus arriving at the dorsal organ was quantified by computing the cross correlation between the recorded output pressure of the MFCS and the fluorescence signal measured at the larval dorsal organ. The shift of the peak of the cross correlation with respect to the peak of the autocorrelation of the pressure output signal was

taken as the indicator for the time lag in each experiment. The estimated lag ranged between 500 and 600 ms; the final lag was estimated to be 500 ms (Figure 13).

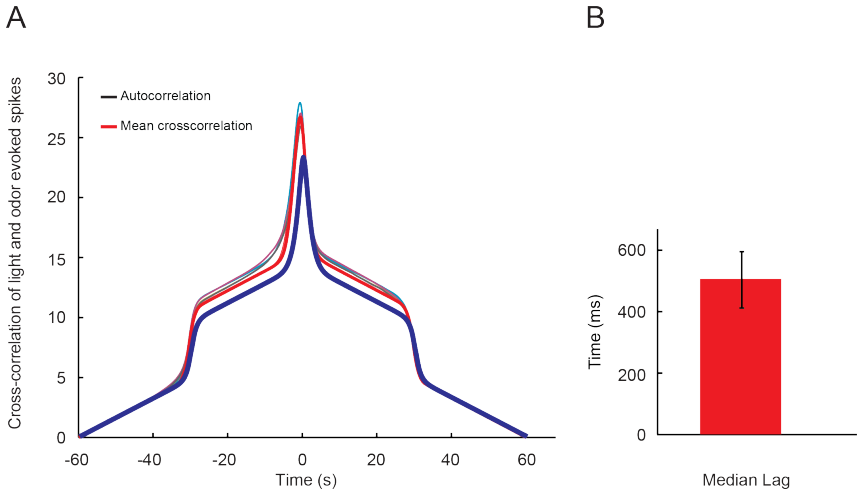

Figure 13. (A) Autocorrelation (blue) of the pressure signal and cross correlation (red) of the pressure and the measured fluorescence signal (other colors indicate the cross correlation derived from individual fluorescein experiments). To compute the time lag of the odor stimulation, the shift of the peak of both correlations with respect to each other was computed.

(B) Median lag estimated over 7 experiments (exponential fluorescein stimulation). The error bar represents the standard deviation.

Odor stimulation in gas-phase

The gas-phase odor stimulation was achieved by means of a custom olfactometer delivering a continuous stream of air (510 mL/min). The air stream, regulated by two mass flow controllers (Cole-Parmer, USA), was humidified, and subsequently passed through the odor solution after which the odorized air stream was delivered to the tip of the larval head — the site of the dorsal organ. Rapid

concentration changes of the odorized stream were achieved by varying the flow between the empty channel and the odor channel while keeping the overall flow constant. A custom Labview protocol (analogous to the one driving the MFCS during liquid phase odor stimulations) was used to control the flow rate of the individual mass flow controllers in real time at a sample rate of 30 Hz. This setup is similar in design to past olfactometers (Borst 1982; Kim, Lazar et al. 2011) and it was adapted to produce a stimulus time course on the timescale of the typical run produced by a larva.

Gas-phase odor calibration: Determining the absorption coefficient of isoamyl acetate (IAA) using IR spectroscopy

Fourier Transform-Infrared Spectroscopy (FT-IR) takes advantage of the fact that molecules absorb specific frequencies that are characteristic of their structure. The infrared spectrum of a sample is recorded by passing an infrared light beam through a sample. When the frequency of the IR is the same as the vibrational frequency of a bond, absorption occurs. Examination of the transmitted light reveals how much energy was absorbed at each frequency or wavelength. During a measurement, the whole wavelength range is measured at once and then an absorbance spectrum is generated. Analysis of the position, shape and intensity of peaks in this spectrum reveals details about the molecular structure and concentration of the sample.[1] The advantage of FT-IR spectroscopy lies in the precision of its quantitative measurements. Using this

[1] https://en.wikipedia.org/wiki/Infrared_spectroscopy

technique, odor concentrations of pure odors can be measured directly as opposed to the relative measurements obtained by a photoionization detector (PID). However, the temporal resolution of FT-IR spectroscopy is much slower than the above-mentioned PID. In FT-IR spectroscopy, absolute odor concentrations are calculated by applying the Beer Lambert law, which states that the absorbance (A) of an absorbing chemical species is directly proportional to the path length (l) and concentration (c) of the chemical. Absorbance (A) is a measurement without any units, obtained at a particular wavelength of light.

$$\varepsilon = \frac{A}{c * l}$$

$$\varepsilon = \frac{4894.7M^{-1}}{10.2cm}$$

A gas-flow cell was used to assess the molar extinction coefficient of the odor in gaseous phase. The average odor concentration along the light path was estimated using the Beer-Lambert law (Swinehart 1962). The odor (IAA) was mixed with the solvent n-hexane[1] in different proportions and injected directly into the gas flow cell by using a 10 uL Hamilton syringe. To minimize errors, the volume injected into the cell was fixed to 10uL. The quantities of odor tested were 0, 0.01, 0.1, 0.2, 0.25, 0.5 and 1 mL. In all cases, the absorbance was measured by calculating the height of the absorption peak at the wave number 1765 cm^{-1} — a wavelength specific to IAA (Freeman 2006). In order to reduce the noise of

[1] Hexane represents a substance, which does not absorb light at the wavelength specific to IAA.

each measurement, absorption spectra were calculated from multiple scans (90 – 100 scans). Between trials, the gas flow cell was disassembled and all parts were rinsed with n-hexane. In addition, the chamber was constantly evacuated by connecting the exhaust to a 20 kpa vaccum connection in between each measurement and wash.

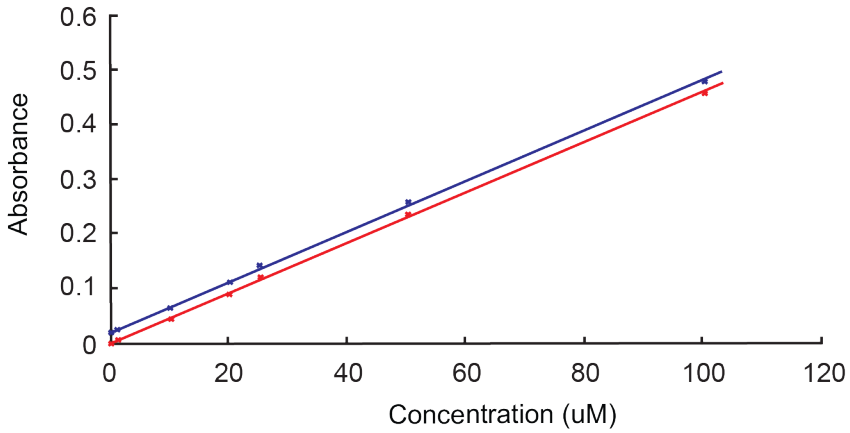

Figure 14. Absorbance of isoamyl acetate (IAA) at different concentrations. The data corresponds to the maximum peak height for each measurement.

The experimentally measured absorbances are presented in Figure 14. In the absence of odor, it was found that the absorbance at 1765 cm^{-1} was not zero but 0.0199 (red square). This marginal absorption might have been due to the presence of some residual odor on the wall of the flow cell after the wash and/or weak absorption by hexane at 1765 cm^{-1}. To account for this offset, the absorption measured in the presence of odor was corrected by the value observed in the presence of the solvent only (Figure 14).

To estimate the absorption coefficient, the three highest dilutions were taken into consideration — the very same concentrations used by Louis, Huber, et al. and Asahina et al. (Louis, Huber et al. 2008; Asahina, Louis et al. 2009). Considering the geometry of the gas-flow cell (height: 10.2 cm, radius: 1.4 cm), the absorption coefficient was estimated to be 479.87 M^{-1} cm^{-1} at 25° C (Figure 15).

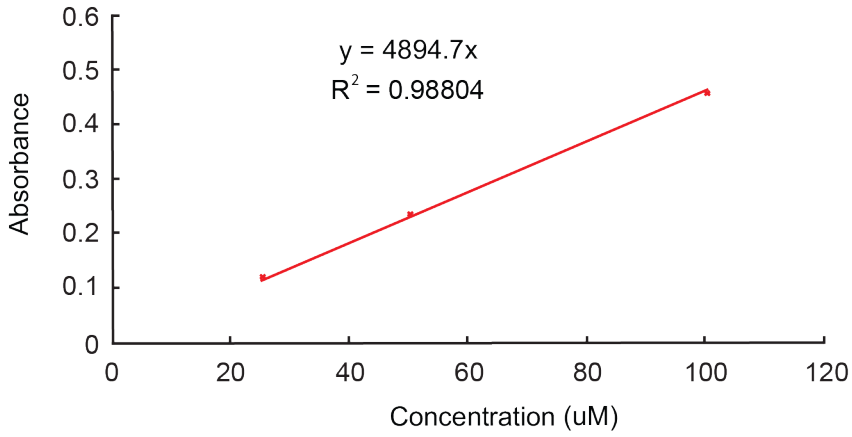

Figure 15. Estimation of the absorption coefficient based on least-square error fit. By using the slope of the absorbance, the absorption coefficient was calculated: $\varepsilon=4894.7/10.2=479.87$ M^{-1} cm^{-1}.

When injecting an excess of 5 uL of pure odor into the cell some part of the liquid odor remained visible on the bottom of the cell meaning that the odor did not fully evaporate. Thus, it was assumed that purely saturated odor vapor was present inside the gas cell and this condition was chosen to estimate the concentration of saturated odor. The measurement was initiated right after the injection of 10 uL odor and performed for 15 min during which the absorbance increased monotonically. After this point, the absorbance saturated at a value close to 1.36 (offset corrected) (Figure 16). Using the

absorption coefficient, the concentration of the saturated vapor was estimated to be 278.45 uM.

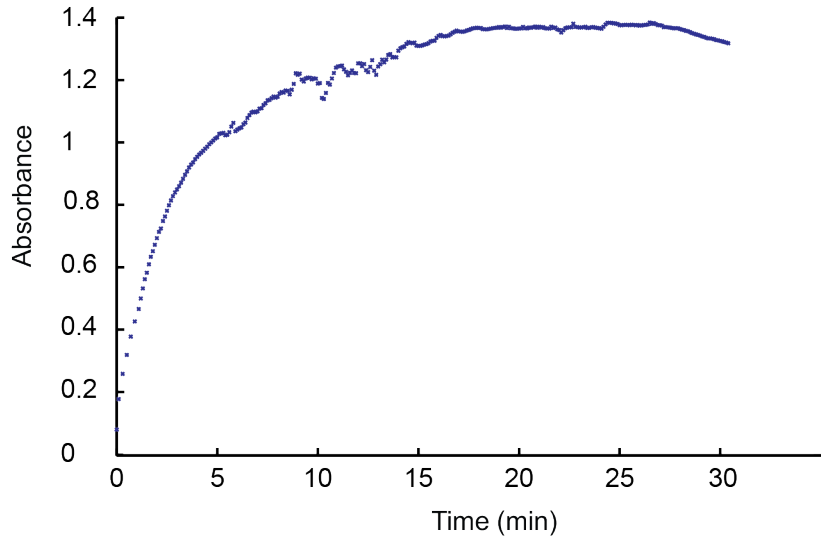

Figure 16. Estimation of the concentration of saturated odor vapor. The measured absorbance can be seen to saturate around 20 min into the experiment indicating that the vapor inside the cell was saturated.

Gas-phase odor calibration: Estimating the saturation concentration of the airborne odor flow using IR spectroscopy

To establish the saturation concentration of air passing through pure IAA the odor stream was directly injected into the gas flow cell. However, for unknown reasons, the absorbance exceeded the measurable range. To lower the resulting concentration, the airborne flow was diluted by clear air in the following ratios: $\frac{1}{10}$, $\frac{1}{20}$, and $\frac{1}{80}$ (Table 1). These ratios were approximated in a fixed resulting flow of 950 mL/min — a flow rate also compatible with the suction of

the photoionization detector used for the calibration described in 'Materials and Methods; Gas-phase odor calibration without artifacts: Measuring the airborne odor concentration with a photoionization detector (PID)'.

Table 1. Estimation of the odor concentration of a saturated odor flow (IAA).

Dilution	Absorbance	Predicted absorbance for pure odor	Predicted concentration of saturated vapor
1/83 (0.06V)	0.0183	1.521	310.66 uM
1/38.5 (0.13V)	0.0373	1.436	293.47 uM
1/19.2 (0.26V)	0.0847	1.626	332.12 uM
1/10 (0.52V)	0.0163	1.630	333.05 uM

After a short initial rise, the absorbances quickly saturated at a plateau value. These plateau values were taken to infer the absorbance expected for an undiluted flow. The corresponding airborne odor concentrations were calculated by using the absorption coefficient derived from Figure 16.

The estimated odor concentrations of the saturated vapor were clearly larger than the value measured upon injection of 10 uL of pure odor in the cell (278.445 uM). How did this discrepancy arise? One possible explanation is that a constant flow of odorized air funneled through the gas cell results in condensation of IAA at the gas cell's glass wall leading to a steady rise of the measured absorbance largely exceeding the values measured with static,

odorized air. This hypothesis was subsequently tested by measuring the absorbance of an airflow containing purely saturated vapor (Figure 17). In this experiment the air passing through 10 mL of pure IAA was kept at a constant flow. However, this time, the measurements were initiated before the injection of the saturated airflow into the flow chamber was initiated. Upon injection of the odor flow, the measured absorbance rose continuously well above the levels measured in the experiments where 10 uL of pure IAA were injected into the gas cell. The absorbance reached values as high as 2.54, two fold the value measured for saturated vapor, and showed no sign of saturation when the experiment was stopped, thus corroborating the notion of continuous odor condensation at the gas cell's wall.

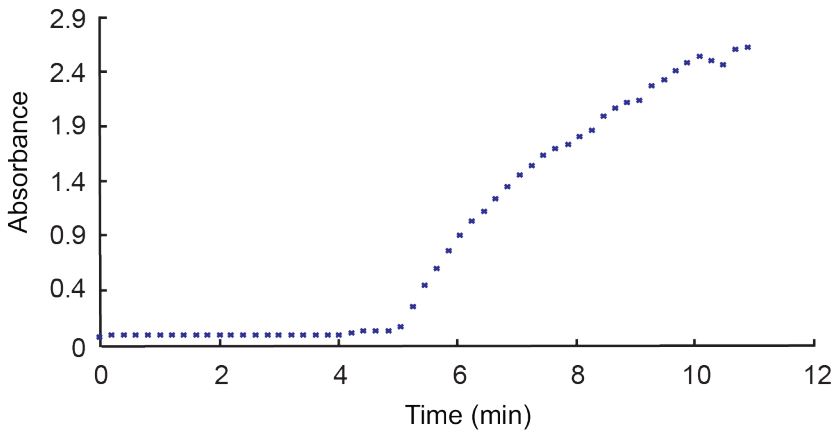

Figure 17. Measuring the absorbance of a saturated odor flow (IAA): The measured absorbance rises steadily and never saturates due to condensation or adsorption of the odor.

In light of this artifact specific to the FT-IR-Spectroscopy it was decided to use the PID to measure the concentration of the odorized air stream.

Gas-phase odor calibration: Measuring the airborne odor concentration with a photoionization detector (PID)

In a photoionization detector (PID) air is continuously sucked into a compartment where an UV lamp excites gaseous odor molecules into positively charged ions. As a result the gas becomes electrically charged and the ions produce an electrical signal, which is reported by the detector. With increasing concentrations of an airborne odor, more ions are produced, leading to a stronger signal at the detector. The PID is not capable to measure absolute odor concentrations, but rather relative differences of odor concentrations. The voltage readout that it provides needs to be calibrated by odorized air with known concentration.

To calibrate the PID, the air stream was passed through pure IAA to obtain saturated vapor. However, since the PID signal saturated at very high concentrations of airborne IAA, it was necessary to dilute the airflow down to a measurable range. The saturated vapor was obtained with the olfactometer in the same experimental conditions as described in the previous section (see 'Materials and Methods section; Gas-phase odor calibration with artifacts: Estimating the saturation concentration of the airborne odor flow using IR spectroscopy'). The concentrations of the diluted air stream

were calculated assuming a 278.445 uM saturation concentration as determined by IR spectroscopy.

Table 2. Air-borne odor concentrations used for the calibration of the PID.

Dilution	Air-phase Concentration [uM]
∞	0 uM
1/83 (0.06V)	3.35 uM
1/38.5 (0.13V)	7.23 uM
1/19.2 (0.26V)	14.50 uM
1/10 (0.52V)	27.84 uM

The estimated concentration values of the diluted air stream used for the PID calibration are reported in Table 2, while the calibration curve is shown in Figure 18. It can be seen that the PID voltage s_{PID} and the airborne odor concentration followed can be estimated by a linear function with a slope of $a = 5.5444$ 5. The concentration of IAA in the odorized air stream could be estimated as follows:

$$c(IAA)_{air} = a * s_{PID}$$

$$c(IAA)_{air} = 5.5444 * s_{PID}$$

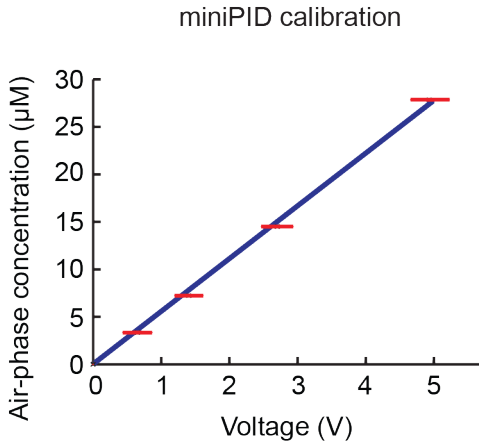

Figure 18. Calibration of the photoionization detector (PID) with airborne odorant stimuli showing a linear relationship between the odor concentration and the measured voltage change. Error bars represent the standard deviation.

Calcium imaging of single OSNs at the level of the antennal lobe

The OSN activity was monitored by means of calcium imaging at the axon terminal of the OSNs at the level of the larval antennal lobe (*Or42a*>GCaMP3) using a high-speed camera (Andor, United Kingdom) and a fluorescence microscope (BX51 mounted with 40x water immersion objective, Olympus, Japan) at a sample rate of 30 Hz. The OSN activity was measured during odor stimulation in gas and liquid phase, respectively.

Tungsten electrode recordings

In contrast to the suction electrode recording technique where the delicate antennal nerve within the glass electrode requires the whole prep to stay in contact with extracellular saline at all times, the

tungsten electrode recording technique — since the signal is recorded by the tungsten wire directly — does not require a liquid recording environment and can be carried out while the larva is exposed to the air. However, due to the dry recording environment, the larval head cannot be dissected when using tungsten electrodes to record from the OSN, as doing so would lead to immediate dehydration of the tissue. As a result, the olfactory nerve is much more difficult to target with the electrode and a strong neural signal is hard to record. To facilitate the acquisition of a strong signal, recordings were carried out in larvae having all OSNs functional. Attempts to record in single functional larvae did not yield a meaningful response. In my tungsten electrode recording experiments I was able to record the local field potential of the OSN while the detection of spikes was only successful in very few recordings and were only obtained in a thoroughly filtered dataset.

Recordings were carried out with etched uncoated tungsten electrodes with a tip size of ~3 - 5 um. Etching was carried out in accordance to the protocol by Pellegrino et al. (Pellegrino, Nakagawa et al. 2010). A raw (un-etched) tungsten electrode was inserted (from above) into an upright standing 50 mL falcon tube filled with 0.5 M potassium hydroxide while applying a constant dc voltage (7 V). The anode was connected to the tungsten electrode, while the cathode was connected to the etching solution. Approximately 10 alternating cycles of immersing either 1/3rd of the length of the electrode or only the very tip into the etching solution were carried out. The cumulative time of tip etching was 6 - 7 min, while the cumulative time of 1/3rd length etching was 3 - 4 min.

Etching of multiple tungsten electrodes at once lead to a slight increase in the time that was necessary to complete the etching process.

The blunt end of an etched tungsten wire was inserted into a slightly shorter boroscillate glass capillary filled with 1% agarose (in H_2O). The back end of the electrode pointing out of the glass capillary was then inserted into the electrode holder and finally carefully wrapped around the gold connector pin. The boroscillate glass capillary greatly enhanced the stability and thus the movement precision of the long tungsten wire. The tip of a 10 uL plastic pipette tip was cut at the back to get a piece that was ~10 mm in length. The larva was inserted at the rear end of the pipette tip which was in turn inserted into a 10 mm long cut silicone tube (Novosil 1x3 mm) that was finally connected to a 50 mL syringe filled with extracellular saline (Singleton and Woodruff 1994. Applying a pressure of approximately 500 mbar through the syringe, the front end of its mouth hook was allowed to point out of the pipette tip. While applying a constant pressure with the syringe in order to expose the larval mouth hook at the front of the pipette tip, the tissue around it was glued to the pipette tip by mouth-pipetting around 5 ul of histoacryl using a broken boroscillate glass pipette. The reference electrode, a chlorinated silver wire connected to a CV-7 headstage, was inserted from the back end of the silicone tube connected to the pipette tip and moved forward until it slightly touched the rear end of the larva. Finally, a pulled and subsequently broken boroscillate glass pipette was inserted into the remaining end of the silicone-tubing-larva-containing-pipette-tip (next to the silver reference

electrode) to fix it with the pipette holder. The pipette holder was connected to the pressure-driven flow controller to allow the application of a constant pressure on the larva keeping the mouth hook immobilized end exposed to the air. A typical working pressure ranged from 100 – 700 mbar. Typically, the pressure was set to a value where all movements of the mouth hook ceased and the larva appeared to be completely immobilized. A sketch of the recording setup is shown in Figure 19.

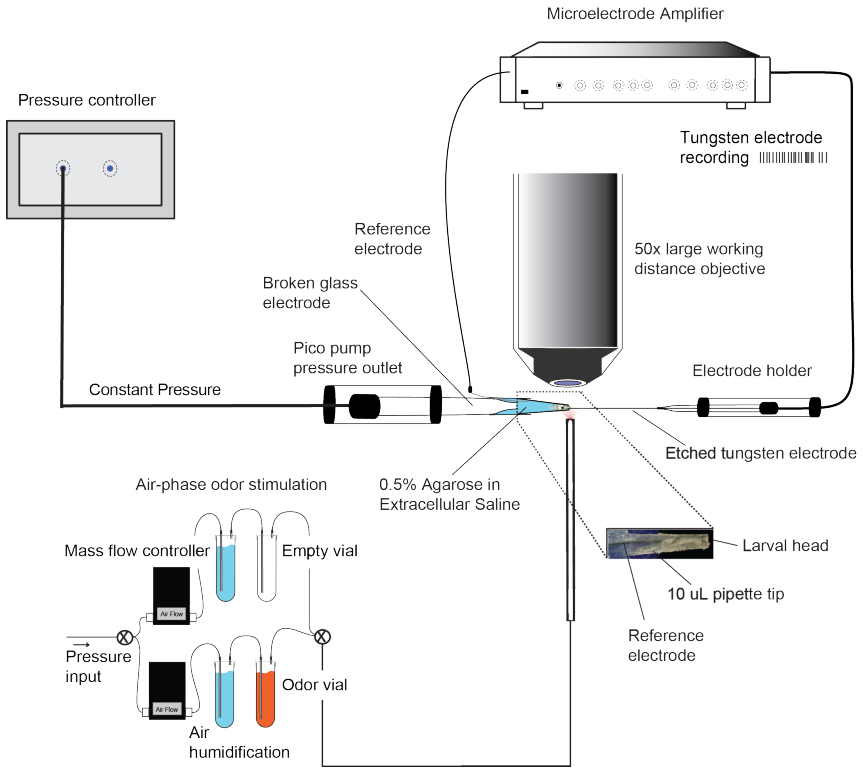

Figure 19. Tungsten electrode recording setup with air phase odor delivery system.

The tungsten electrode was moved into the vicinity of the larval dorsal organ (frontal) using the 10× magnifying objective, while the actual targeting of the antennal nerve ganglion was carried out using a 50× long working distance objective. GFP expression in the OSNs used as a beacon to guide the tungsten electrode towards the cell bodies within the dorsal organ's dome. Recordings were carried out in the dome both close do the dendrites as well as near the cell bodies at the antennal nerve ganglion where the local field potential (LFP) of the neural activity was detected. Figure 20 illustrates the LFP in response to a linear stimulation of IAA recorded in an animal in which all OSN were functional (WT – W1118). All recordings were carried out with Multiclamp in current clamp mode (100× AC membrane potential, 500 mOhm, Gain = 1) with a 10 kHz bessel filter. The signal was recorded at a sample rate of 20 kHz in a PC equipped with the free data acquisition software SpikeHound (Lott III 2009). Air-phase odor ramps of IAA were delivered using a constant airflow generated by a custom built olfactometer controlled by Labview (as described in 'Materials and Methods section; Odor stimulation in gas-phase'). The overall flow rate was monitored before the actual experiment using an electronic mass flow meter. It was noted that the tungsten recording method was more prone to picking up electrical artefacts and much more sensitive to electrical noise compared to the suction electrode recording technique.

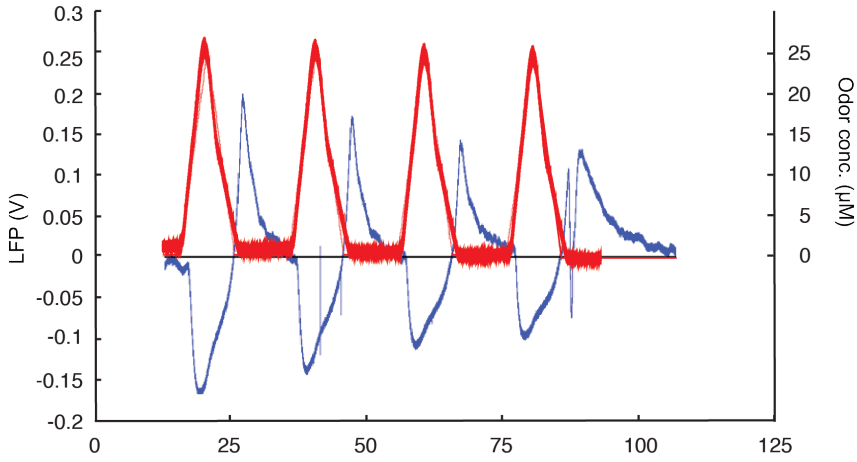

Figure 20. LFP recorded in WT larva response to linear IAA odor ramps (blue). The odor concentration, which was measured separately, is reported in red. It can clearly be seen that the LFP changes with negative values in response to the odor. Over the time course of the odor stimulation pattern the OSN response decreases in amplitude – a hallmark of adaptation.

Behavior

The closed-loop larval tracker: A versatile tool to record and classify behavior at high temporal and spatial resolution

The behavior of single larvae was studied in a closed environment with a droplet of IAA placed on the 'ceiling' of the arena. These experiments were carried out in the larval tracker, which contained a large glass arena covered by an agarose slab (Figure 21A). The video camera was mounted on a moving stage following the behaving larva in the middle of the three blue LEDs (LCS-0470-03-22 LED, Mightex Systems, Canada), and delivered images at a resolution of 800x800 pixels with a frame time interval of 23 ms. Below the arena was a red LED backlight providing the necessary illumination. The camera was equipped with a high-pass filter to filter out any blue light from the blue light stimulation. The larval tracker stimulation module consisted of three blue LEDs, connected in serial and whose angle and position were fixed to maximize the light intensity at the arena within the camera's field of view. The LEDs were connected to an LED controller (Mightex Systems P/N: SLA-1200-2) whose output current limit was set to 750 mA. The controller's output current was changed in direct proportion to the analog voltage fed to the controller.

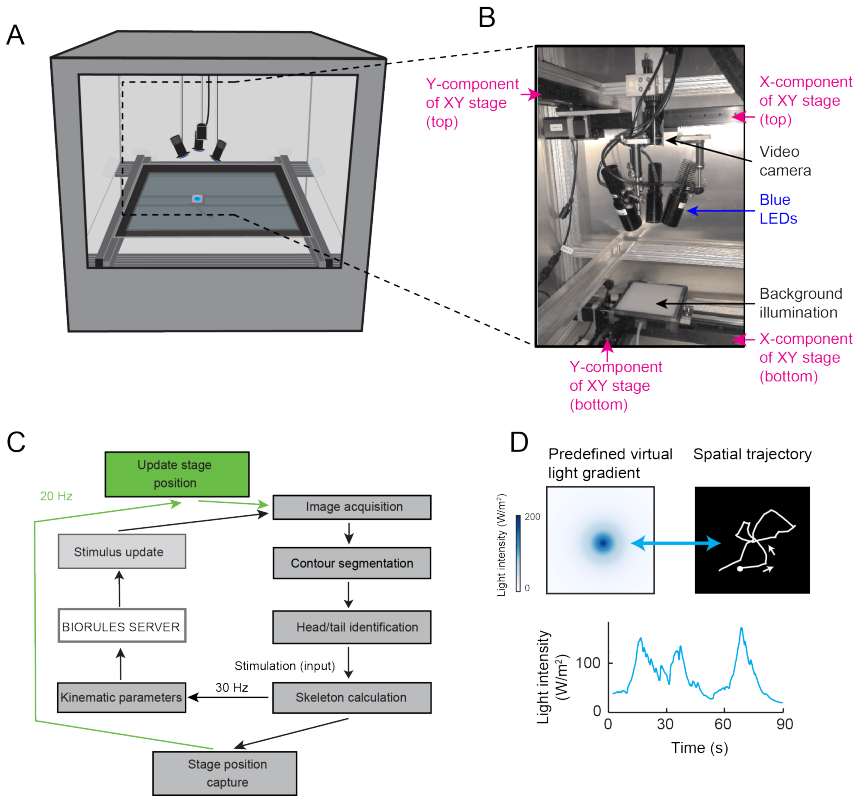

Figure 21. (A) Schematic drawing of the closed-loop tracker. The blue LEDs and the camera are mounted on a moving stage that follows the larva while it crawls on an agarose slab (40x40 cm or approximately 120x120 body lengths of the larva).

(B) Depiction and description of the moving camera stage equipped with three LEDs.

(C) Flow chart outlining the interaction of the core modules of the tracking software.

(D) Illustration of the spatial trajectory generated by an *Or42a*>ChR2 larva upon stimulation by a virtual light gradient. (Top-left) Predefined light landscape with a geometry approximating the odor distribution produced by a point source. During the behavioral tests, the full gradient is not projected onto the arena: the larva is illuminated by the LEDs at an intensity determined by its position in the virtual light gradient. (Bottom) The light intensity is updated based on the motion of the larva, which forms the temporal evolution shown in the graph. (Top-right) The spatial trajectory described by an *Or42a*>ChR2 larva in the virtual light gradient.

The larval tracker control unit (LTCU) represented the main hardware interface responsible to drive both LEDs and a video camera. While the camera was controlled via a transistor–transistor logic (TTL) signal, a 12-bit digital-to-analog converter (DAC) output was used in sending the control signals (0 – 5 V analog signal) to the LED controller. An In-Circuit Debugging (ICD) Port was used for connecting the LTCU to an ICD3 Programmable Interface Controller (PIC) via a registered jack (RJ11) connector interface, while an USB Port enabled the LTCU's communication to the PC. An embedded program written in C is used to run the LTCU. This C program enables the LTCU to respond to the commands issued by the PC. The software interface of the tracking and image analysis software interfacing the LTCU was written in JAVA.

Kinematic variables and behavioral mode classifiers

Alex Gomez-Marin, Matthieu Louis, and Moraea Phillips performed the work on the definition of all kinematic variables and behavioral mode classifiers.

In a first attempted turning events were detected in an off-line analysis by setting a threshold on the reorientation rate of the larva. Although this method led to satisfactory results in previous studies, the higher resolution of the closed loop tracker analysis made it unsuitable for the conditions tested. Therefore, a geometrical approach based on the topology of the physical trajectory described by the larva was adopted. In a first step, the trajectory was parsed into segments of equal sizes. Next, the angle between successive

segments of the trajectory was calculated. Finally, the distribution over these angles was computed. This distribution had the characteristics of a long-tailed exponential. The threshold was set at the location of the 'kink' of the distribution. Turning events were associated with positions where the trajectory curled at an angle larger than the threshold. Good results were obtained for trajectory segments of 5 mm and an angular threshold of 20 degrees. The results of the behavioral classification were insensitive to the exact value of the trajectory segments and the angular threshold. The turn identification was based on the trajectory of the midpoint. To distinguish runs from non-runs, empirical filters based on three sensorimotor features were defined:

The first feature was the head angle between the direction of the body axis and the neck axis (midpoint-head). The second feature was the instantaneous velocity vector measured at the tail position (vector v_{tail}), and the third feature the angle between the tail velocity vector and the direction of the body axis (unitary vector 1_m) (Figure 22A). Transitions from a run to a non-run state take place as soon as (1) the head angle is larger than a threshold t_1 or (2) the dot product of the tail velocity vector and unitary vector corresponding to the direction of the body axis is smaller than t_2 (condition C1) (Figure 22B). The first condition on the head angle identifies head casts while the second condition on the dot product identifies sequences of behavior associated with a stop or a forward run. Transitions from a non-run to a run take place when the following two conditions are verified: (3) the head angle must be lower than the threshold value t_3 and (4) the dot product of the tail velocity and

unitary vector along the body axis must be larger than t_2 (condition C2). The thresholds of the conditions (1-4) were set at a value that maximizes the difference in the cumulative distribution of the run and non-run state along the relevant sensorimotor feature (head angle or dot product) for the two possible types of behavioral state transitions (run → non-run or non-run → run) (Figure 22B). Distributions of the frame-by-frame sensorimotor features were constructed by pooling the annotated frames from 4 representative trajectories. The manual ground-truth annotation was achieved by Vani Rajendran and Matthieu Louis. The value of the thresholds used in the analysis were: t_1=18 degrees, t_2=0.0065 and t_3=13 degrees. Figure 22C bottom shows a frame-by-frame manual classification of run/non-run behavior achieved by the two trained annotators (A1 and A2) in comparison to the computational classification obtained by the filters described in panel B. The table reports the percentage of true positives (frames classified as a run by both the annotator and the algorithm) and false negatives (frames classified as a run by the annotator and a non-run by the algorithm). This good match validates the use of the computational classifiers in real-time experiments. Due to the high sampling rate of the tracker and the inherent noise of the stepper motors, the position of the points of interest were subject to minute jittering.

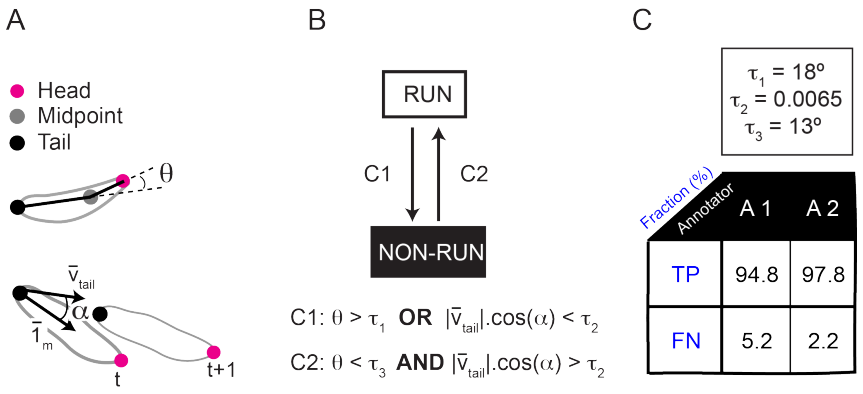

Figure 22. Annotation of behavioral classifiers defining run and non-run states. (A) Definition of runs and non-runs: (1) the head angle between the direction of the body axis (tail-midpoint) and the neck axis (midpoint-head); (2) the instantaneous velocity vector measured at the tail position (vector v_{tail}) and (3) the angle a formed between tail velocity vector and the direction of the body axis (unitary vector 1m).

(B) Illustration of definitions of thresholds of the conditions governing behavioral transitions from run to a non-run state.

(C) (Top) Report of values of the thresholds used in the analysis. (Bottom) Comparison of frame-by-frame manual classification of run/non-run behavior achieved by the two trained annotators (A1 and A2) versus the computational classification obtained by filters described in panel B.

To get rid of these artifacts, the trajectories were smoothened with a Savitzky-Golay filter (Press 1988; Schafer 2011). This gentle filtering removed the fluctuations on small spatial scale irrelevant to the motion of the larva. The geometric approach was used to classify the data from all closed-loop experiments. For all open-loop experiments turns were identified by the online classifier implemented in the tracker software.

Virtual light environments: Closed-loop and open-loop tracking conditions

The larval tracker was used under two conditions:

(1) closed-loop, where the motion of the larva was directly driving the stimulation pattern, thereby closing the sensorimotor loop;
(2) and open-loop, where the motion of the larva had no influence on the stimulation pattern.

For closed-loop experiments (1) involving a virtual light landscape (Figures 60, 62, and 67), the light intensity was updated based on the position of the head of the larva mapped on a predefined light landscape. The light landscape was loaded in the software controller environment as a matrix with a spatial resolution of 1x1 mm. Since the position of the larva was monitored at a higher resolution, the intensity of the spatial landscape was redefined by using a bi-linear interpolation along the x and y-axis. The position of the center of the light gradient was automatically adjusted at the beginning of the experiment in such as way that every larva started in a direction facing the center of the gradient at a fixed distance of 9.6 mm from the center for the exponential light gradient (Figures 61 and 63A) and a distance of 17.1 mm for the family of light landscapes (Figure 67). The minority of trajectories from which larvae failed to detect the presence of the light gradient was discarded from the dataset.

In open-loop conditions (2) on the other hand, the LED intensity was updated in accordance to a predefined temporal light stimulus (by randomly selecting either a pre-defined light stimulation function or continued baseline stimulation) only when a larva is in a run mode. During a run, the motion of the larva had no influence

on the intensity of the stimulus. A predefined run-based light stimulation was stopped and returned to its baseline value as soon as a larva terminated its run to initiate a turn.

In chemotaxis experiments involving real odors the tracker was purely tracking larval behavior in the odor gradient without executing any light stimulation at all.

Creation of controlled odor gradients to study larval chemotaxis

The controlled odor environment was created in a 120 mm x 120 mm x 12 mm arena consisting of a polystyrene dish (the lid of a Greiner square dish, Sigma-Aldrich, USA) standing on a 2% w/V agarose surface inside the closed-loop tracker (Figure 23). A 3 uL 0.25 M IAA odor droplet was placed inside a plastic reinforcement ring at the center of the dish (internal diameter of odor droplet: 5 mm). Inside the arena, an odor gradient formed by the diffusion from the source for 30 s prior to the introduction of a single larva. This step required briefly opening the arena. The tracking of single animals was then initiated and lasted for a minimum duration of 3 min.

Quantification and modeling the odor diffusion underlying the odor gradient during chemotaxis

Diffusion from an odor droplet creates a radially symmetric gradient that can be approximated by a Gaussian distribution (Louis, Huber et al. 2008; Asahina, Louis et al. 2009; Gomez-Marin, Stephens et al.

2011). However, unlike in previous work, it was found that the reduced volume of the source leads to a non-stationary gradient that could not be adequately approximated by a static Gaussian distribution. In fact, the Gaussian profile was slowly flattening out over the time course of several minutes. Larvae performing chemotaxis were exposed to an odor gradient that slowly changed over time. Therefore, a precise quantification of the dynamics of the odor diffusion process was needed, to correlate the behavior of the larva with a faithful reconstruction of the odor gradient. To this end, Madhusudhan Venkadesan developed a model for the diffusion of the odor inside the behavioral arena. The diffusion process was modeled based on a system of partial differential equations (PDEs) that included realistic boundary conditions.

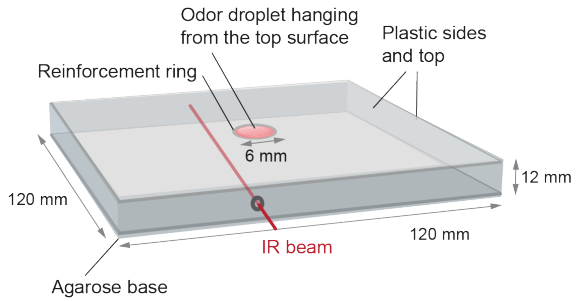

Figure 23. Configuration of behavioral arena used in the model consisting of a rectangular transparent plastic box sitting on a surface of agarose. The odor source consisted of a solution of IAA mixed with paraffin oil.

The parameters of the PDE model were optimized to fit the IR measurements (Figure 24). The reconstructed odor gradient then served as a template to infer the stimulus time course experienced by the larva during real trajectories (Figure 26 and 27).

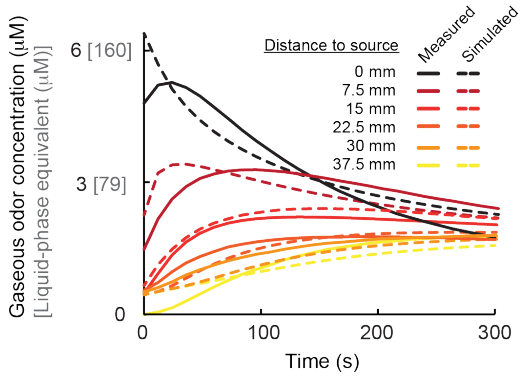

Figure 24. Physical model of odor diffusion in behavioral arena. Infrared spectroscopy was used to estimate the absorbance and thereby the average concentration along sections of the arena (IR beam depicted in panel A). The time course of the cumulated concentration was determined for 7 sections at a distance from the source ranging from 0 to 45 mm (only first 6 are shown in the graph). Measurements were made for a source of 1.0 M. The parameters of the model were estimated by optimizing the fit of the model with the average concentration profiles along the 7 sections of the arena. The PDE model led to a good fit of the temporal profiles of the average concentrations after an initial transient phase of 30 s.

All behavioral experiments were conducted at a concentration of 0.25 M. At this low concentration and due to the small volume of the source, accurate temporal profiles of the average odor concentration could not be obtained through infrared spectroscopy for all sections of the plate. Therefore, the gradient was estimated by using a source concentration of 1 M assuming that the gradient forming inside the arena scaled linearly with the source concentration. This assertion however, could only be validated at the area where the concentration was highest — directly under the source (Figure 25).

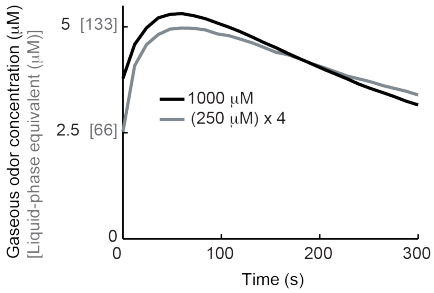

Figure 25. Behavioral experiments were conducted with a 3 uL odor droplet at a concentration of 0.25 M. Under the source, it was found that the average concentration of the odor scaled as a function of the source concentration. The gradient reconstructed at 1.0 M was scaled by a factor 0.25.

Using Fourier transform–infrared (FT-IR) spectroscopy, the odor concentration time course along the length of the single-odor-source device was measured for various cross sections (one every 7.5 mm) of the behavior chamber to reconstruct the two-dimensional geometry of the odor gradient (Louis, Huber et al. 2008) (experimental setup described in 'Materials and Methods section; Creation of controlled odor gradients to study larval chemotaxis'). The measurements were taken after the odorant was placed in the chamber following the exact same protocol used for the behavioral experiments. From these 7 sections, the average concentration was measured continuously over a time interval of 360 s (Figure 24).

The parameters underlying this physical model were estimated by model-based estimation techniques. The process was modeled as a 3D diffusion, with separate diffusion constants for air and the droplet. Exposed plastic surfaces of the chamber were treated as adsorptive boundary conditions. Since the odor gradient was initially established in the arena for 30 seconds before the introduction of a larva, the model also included non-zero initial concentration of the

odor in the air, agarose and plastic chamber. COMSOL Multiphysics v4.3 was applied to solve the diffusion equation.

The geometry of the experimental arena is described in Figure 23. The radius r_{ring} of the odor ring confines the liquid droplet so that the radius of the flat face is equal to r_{ring}. The volume V_{drop} of the droplet, made up of odor and solvent, is fixed to be 3 uL. The formula of a sphere is given as

$$V_{drop} = \frac{\pi}{6} h_{drop}\left(h_{drop}^2 + 3r_{ring}^2\right)$$

with h_{drop} as the droplet height. The agarose layer at the bottom of the chamber was modeled as a two-dimensional sheet with an independent diffusion constant.

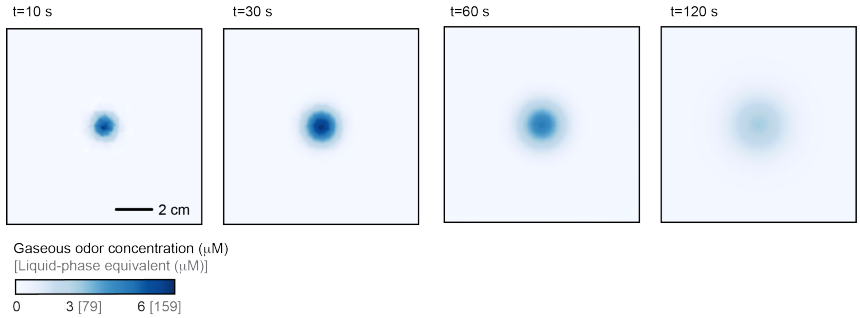

Figure 26. The numerical integration of the PDE model allowed for a reconstruction of the temporal evolution of the odor gradient experienced by the larva at arbitrary spatiotemporal precision. The reconstruction was saved at time steps of 1s. Between defined sections the gradient was linearly interpolated. Over time, the gradient tended to flatten out, an effect caused by a gradual depletion of the source.

Parameter estimation was achieved using the MATLAB/Optimization toolbox by solving a nonlinear least squares problem. For a given set of parameters based on an initial guess about the order of magnitude, the diffusion process was simulated, and integrals of the concentration along the sections corresponding to the experimental measurements were evaluated. The objective function to be minimized for estimating the parameters was the root mean squared error of the average concentration at each of the seven locations and at all times.

The results of the dynamic gradient reconstruction are shown in Figure 26. The difference between the static and the dynamic temporal odor profiles shown in Figure 27 underlines the importance of the dynamic gradient reconstruction for the experimental conditions.

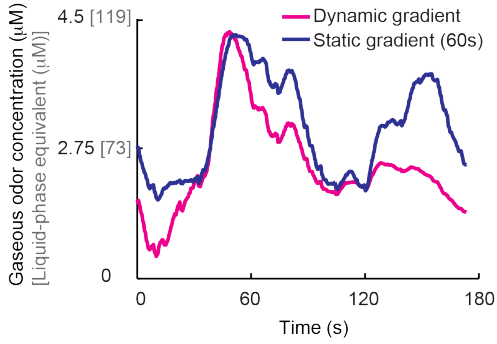

Figure 27. Reconstruction of the concentration time course experienced during a representative trajectory (the one shown in Figure 29, panels A and B). The magenta trace was obtained after mapping the behavior on the dynamic reconstruction of the gradient shown in Figure 26. In contrast, the blue trace was obtained after mapping the behavior on the gradient computed 60 s after the onset of the odor diffusion.

There were two simultaneous diffusion processes, both of which were modeled using the partial differential equation (PDE):

$$\frac{\partial x}{\partial t} = D_i \nabla^2 x$$

The diffusion constant D_i depended on whether the medium i is air or droplet. At the droplet-air boundary, a flux continuity condition was used — as a result the odorant could not accumulate at this boundary. As a result of the flux continuity at the droplet-air boundary, and because diffusion through air was substantially faster than through the droplet, the odor developed a radial profile in the droplet despite starting with a homogenous initial concentration. This process serves as approximation of the coupled evaporation-diffusion process. Since modeling the diffusion limited evaporation process (Kelly-Zion, Pursell et al. 2011) would render this problem intractable in the context of a model-based parameter estimation, the overall evaporation process was approximated while ignoring natural convection, concentration-dependent changes in volatility, and chemical interactions with the solvent. Although inaccuracies could arise from this approximation, the model was able to match experimental measurements with good fidelity as seen from the results of the model-based estimation (Figure 24).

The top flat face of the droplet that contacts the plastic cap was treated as a no-flux boundary. Flux continuity is imposed on the spherical interface with air. The remaining boundaries, air-agarose and air-plastic, were modeled as Robin boundary conditions to accommodate the possibility of adsorption-desorption. Although

the standard way of treating adsorption reactions would be to use a reactive boundary condition where the odorant is treated as free in the air or bound to the boundary, these boundaries were modeled as a Robin boundary condition, which reduces the number of parameters to be considered. This simplification of the boundary conditions was necessary to estimate the associated parameters with a single experiment.

Considering a diffusing chemical species with concentration $x(t, \vec{r})$ that varies with time t and location $\vec{r}$ within the chamber, the flux vector $\vec{J}$ of this chemical is given by $\vec{J} = -D\vec{\nabla}x$, where D is the diffusion constant in air. If the normal direction to the boundary under consideration denoted as $\hat{n}$, the Robin boundary condition relates to the normally incident flux to the boundary reaction by $-\hat{n}.\vec{J} = k_i(x_{0,i} - x)$, where k_i is related to the reaction rate at the boundary i (agar or plastic), and $x_{0,i}$ is the saturation concentration of the odorant on this boundary. This reaction drives the flux towards the saturation concentration of the boundary. For example, if the concentration of the odorant in air is lower than the saturation concentration, the boundary would become an odor-source by undergoing desorption, with a rate governed by k_i. Conversely, a higher concentration of the odorant in air would lead to adsorption at the boundary.

To minimize the objective function, Sequential Quadratic Programming (SQP) as implemented by the function fmincon in MATLAB v8.2 was used. The Jacobian of the cost function with respect to the parameters being estimated was computed using finite

differences. All physical parameters were constraint to be greater than 0. None of these inequality constraints were active for the converged solution. From 20 random initial guesses that were tried out, one included a condition in which all parameters were set to 0. Once the optimization converged, the converged estimates were perturbed using random numbers. The perturbed estimates were fed back to the estimator, and ran again until convergence. 20 such restarts were carried out, and all of them converged to the same estimates, which are shown in Table 3.

Table 3. Parameters of PDE model for odor diffusion. The parameters were optimized for IAA under the experimental condition outlined described in Figure 23.

Parameter	Physical description	Converged value
$D_{\mathbf{air}}$	Diffusion constant in air	8.9377 x 10^{-7} m^2s^{-1}
$D_{\mathbf{drop}}$	Diffusion constant in droplet	8.7859 x 10^{-11} m^2s^{-1}
$c_{0,\mathbf{air}}$	Initial odorant concentration in air	4.0492 x 10^{-7} mol L^{-1}
$c_{0,\mathbf{drop}}$	Initial odorant concentration in droplet	0.0450 mol L^{-1}
$k_{\mathbf{agar}}$	Robin rate for air-agar boundary	1.5762 x 10^{-6} ms^{-1}
$k_{\mathbf{plastic}}$	Robin rate for air-plastic boundary	5.8025 x 10^{-5} ms^{-1}
$c_{0,\mathbf{agar}}$	Saturation concentration of agar	3.6817 x 10^{-5} mol L^{-1}
$c_{0,\mathbf{plastic}}$	Saturation concentration of plastic	5.7921 x 10^{-7} mol L^{-1}

Fly stocks

Previous work has demonstrated that larvae are very sensitive to light in that they actively avoid it (Xiang, Yuan et al. 2010). Light sensors that are mediating the light avoidance response are located in the larva's bolwig's organ (the larval 'eye'), and in class IV multidendritic neurons along the larva's body wall. In order to make larvae insensitive to light the 410-amino acid apopotosis-inducing protein hid was ectopically expressed in the bolwig's organ (*GMR*>hid) — the larval eye — rendering all photoreceptor neurons dysfunctional even in animals expressing only one copy of the gene (Haining 1999). In addition, by introducing a deletion of the *dtrpA1* gene (*dtrpA1[1]*), the light sensitive class IV multidendritic neurons along the larval body wall lost their sensitivity to light. For this work, all behavioral experiments were achieved in double blind 3rd instar larvae (*GMR*>hid/+;*dtrpA1[1]*) (Kwon, Shim et al. 2008) (Xiang, Yuan et al. 2010) which expressed both the co-receptor *Orco* and the light gated ion channel Channelrhodopsin-2 (ChR2-H134R) in only one OSN(*Or42a*-Gal4/UAS-Orco,UAS-ChR2-H134R;*Orco*$^{-/-}$) (Fishilevich, Domingos et al. 2005). The UAS-ChR2-H134R transgene was a gift from Stefan Pulver and Leslie C. Griffith (Pulver, Pashkovski et al. 2009). The complete genotype of all larvae used in the experiments (both electrophysiology and behavior) was

Or42a-Gal4,GMR>hid/UAS-Orco,UAS-ChR2-H134R;
dtrpA1[1],Orco$^{-/-}$

For the control experiments in larvae with a functional olfactory system (WT background) blind glass^{60j} mutant larvae were used

instead of GMR>hid (*Or42a*-Gal4>UAS-ChR2-H134R;*gl[60j];dtrpA1[1]*) (Moses, Ellis et al. 1989).

Larvae used in all functional imaging experiments expressed the calcium indicator GCaMP3 exclusively in the *Or42a* neuron (*Or42a*-Gal4>UAS-GCaMP3) while having the rest of the olfactory system intact (all OSNs were functional).

All flies were raised on standard fly food[1] containing 0.5 mM all-*trans*-retinal in an incubator in complete darkness (food vials wrapped in aluminum foil) to minimize exposure to ambient light until the experimental test. Approximately 96 hours after egg-laying, 3rd instar larvae were taken out of the food and immersed in a 15% (w/V) glucose solution from where they were taken to participate in a given experiment.

[1] 3% (w/V) molasses; 2% (w/V) yeast; 5% (w/V) corn meal; 0.26% (w/V) agar; 1.5% (w/V) Tegosept/Nipagin; 0.5% (w/V) propionic acid; 87.74% H_2O (V/w).

Chapter 2 - Results

Physiology

Phase conversion of liquid-phase odor concentration to gas-phase odor concentration

While behaving larvae detect odor in air, all electrophysiological experiments were conducted in liquid phase. It was therefore essential to determine the liquid phase equivalent of the air-phase concentration experienced by larvae during chemotaxis. To this end, the calcium indicator GCaMP3.0 was expressed in the *Or42a* neuron (*Or42a*>GCaMP3) and functional imaging at the axon terminal at the level of the larval antennal lobe was performed. The neural activity was measured during odor stimulation in gas and liquid phase, respectively (Figure 28 panels A-C).

The final phase correlation (liquid-phase odor concentration to airborne odor concentration) was established for a 8 s exponential ramp. In liquid phase, both background and maximum concentration were fixed to the pre-existing experimental conditions used for the electrophysiology: they corresponded to a range spanning between 50 mM and 530 mM. The corresponding $\frac{\Delta F}{F}$ of the OSN response ranged between 10% and 60% in liquid phase. The background and maximum concentration of the airborne ramp was adjusted to obtain an activity profile with a $\frac{\Delta F}{F}$ matching the liquid-phase stimulations. According to the measurements performed with the PID, the concentration estimate of the final air-

phase exponential odor time course ranged from 2.20 to 20.13 uM and led to an OSN response whose $\frac{\Delta F}{F}$ ranged between 10% and 59%. It was found that the ratio of the maximum $\frac{\Delta F}{F}$ in both gas and liquid phases was 0.98. The ratio of the integral of $\frac{\Delta F}{F}$ over the full time course of the stimulation was 0.87. The calcium responses elicited by an exponential ramp in the *Or42a* OSN with a concentration range of 50-530 uM in liquid phase was found to be equivalent to a concentration range of 2.20 to 20.13 uM in gas phase. The measured OSN response dynamic was almost equivalent for both phases.

To map the concentration range of 2.20-20.13 uM in gas phase onto the concentration range of 50-530 uM in liquid phase, the ratio between the peak concentrations of the ramp in liquid and gas phases was established:

$$r_{liquid} \rightarrow r_{gas}\colon\ \rho^{\text{liquid-gas}} = \frac{\max\left(c_{liquid}\right)}{\max\left(c_{gas}\right)}$$

$$r_{liquid} \rightarrow r_{gas}\colon\ \rho^{\text{liquid-gas}} = \frac{530\ uM}{20.13\ uM} = 26.73$$

This conversion was applied to predict the behavior of the larva in airborne odor gradient on the basis of a model for the OSN activity developed for liquid-phase stimulations. It was concluded that for the same concentration, the effective number of odorant molecules reaching the odorant receptors had to be 26.73 times higher in gas than in liquid phase. The phase mapping, was not perfect since the relationship $C_{liquid} \approx C_{gas}$ * 26.73 does not hold for the minimum concentration of the ramp (50 uM in liquid and 2.20 uM for gas phases). However, overall the calcium imaging results suggest that response dynamics of the *Or42a*>ChR2 OSN are comparable upon odor stimulations in liquid and in gaseous phases (Figure 28D).

To account for the same level of neural activity achieved in the *Or42a* OSN, the odor concentration measured in gas phase was transformed into the liquid phase equivalent via the following relationship:

$$x_{liquid} = x_{gas} * \rho^{\text{liquid-gas}}$$

where x_{gas} denotes the gas phase odor concentration present during all behavioral experiments, and x_{liquid} denotes the liquid phase concentration as it was present in all electrophysiological experiments. Ultimately, x_{liquid} was used as the input to the IFF+IFB model predicting the neural activity (model introduced in Figure 40).

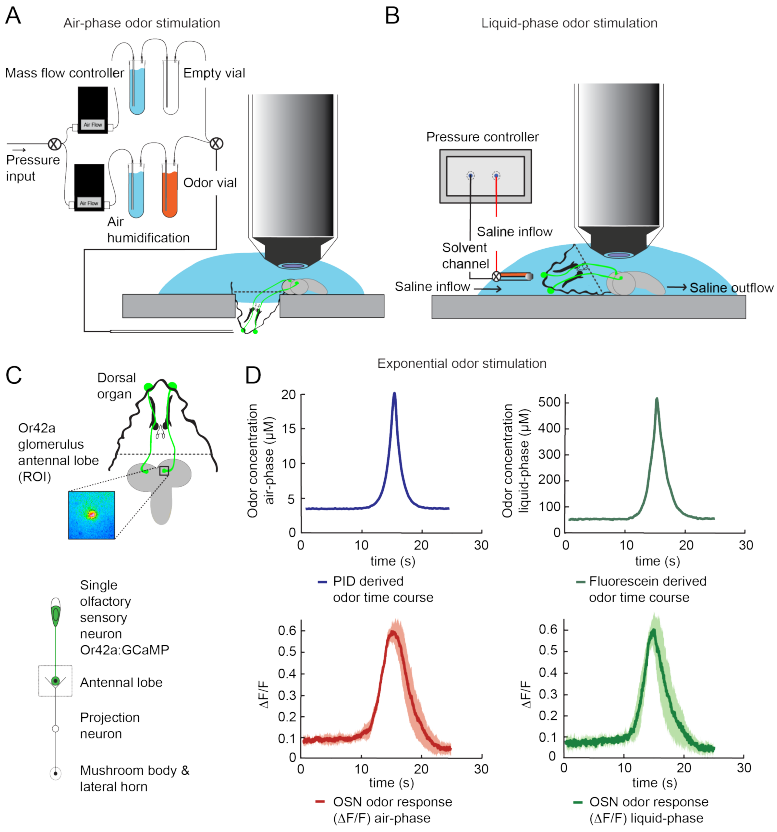

Figure 28. (A) Schematic illustration of the single OSN imaging setup: air-phase odor stimulation of the larval dorsal organ with a custom-built olfactometer. A continuous stream of air (510 mL/min) was regulated by two mass flow controllers. The odorous air stream was delivered to the larval dorsal organ.

(B) Liquid-phase odor stimulation of the larval dorsal organ with a pressure controller connected to a two-barrel pipette. The fixed larval head was perfused by a constant flow of extracellular saline while the odorous solution was delivered via the glass pipette.

(C) Schematic illustration of the imaging site: The OSN activity was recorded by imaging the GCaMP activity elicited in the axon terminal of the *Or42a* OSN at the level of the antennal lobe (*Or42a* glomerulus).

(D) Odor response profile ($\frac{\Delta F}{F}$) of the *Or42a* OSN in response to an exponential odor stimulation in the air-phase (left) and liquid-phase (right). The response amplitude and overall dynamics are conserved between the two phases. The shade represents the standard deviation. The data comes from a total of 6 experiments that were conducted on 3 different preparations. Other functions that were tested in both phases (sigmoid and linear) did not yield as good results as the exponential.

Neural firing in real odor environments: OSN response to naturalistic stimuli

How does the *Or42a*>ChR2 OSN respond to a concentration ramp that replicates the stimulus time course experienced by freely behaving larvae during chemotaxis? This question was addressed by stimulating larvae with a representative odor time course derived from an animal performing chemotaxis (Figure 29, panels A and B). The concentration experienced by the larval head and midpoint during this trajectory is shown in Figure 29C. Electrophysiological recordings of this three-minute stimulation pattern (derived from the stimulus time course experienced at the larval head) in different preparations led to consistent patterns of neural activity (Figure 30A). Although the OSN activity appears to follow the envelope of the stimulus time course, closer examination reveals that the input-output relationship underlying the OSN activity does not follow a simple linear function. The firing rate displays a clear amplification of the changes in stimulus intensity — a phenomenon clearly visible during the first 40s of the stimulus time course. The complexity of the OSN transfer function can be illustrated in the activity corresponding to two consecutive runs, R1 and R2, highlighted in blue in Figure 1A. Run R2 brings the larva close to and then beyond the peak of the gradient. The corresponding stimulus time course displays a 10-s rising phase followed by a falling phase. The neural activity elicited by run R1 and R2 is shown in Figure 30C.

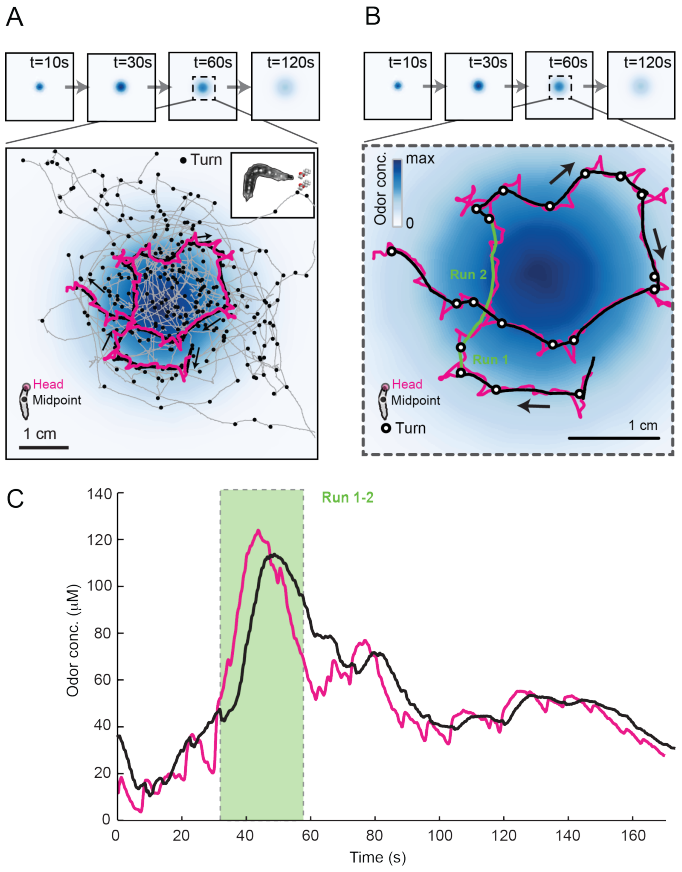

Figure 29. (A) Superimposition of 10 consecutive trajectories observed in an odor gradient of IAA. Trajectories of the midpoint with turns are indicated by small black circles. Arrows indicate the direction of motion. The odor gradient shown in the background corresponds to the reconstructed snapshot 60 s after the onset of the diffusion process.

(B) Illustrative trajectory of a larva freely moving in an attractive odor gradient (IAA, source concentration: 0.25 M). Position of the midpoint shown in black; position of the head shown in magenta. Two run segments, R1 and R2, are underlined in green. Turns are depicted as white disks. Black arrows indicate the direction of motion. The odor gradient in the background was reconstructed from the numerical simulations of the odor diffusion modeled by a PDE system with realistic boundary conditions (snapshot of the gradient 60 s after onset of the odor diffusion).

(C) Concentration time course corresponding to the trajectory of the head (magenta) and midpoint (black) position depicted in panel A. The reconstructed sensory experience is based on mapping the head positions (magenta) and midpoint positions (black) on the reconstructed odor gradient computed upon integration of the PDE system for the entire duration of the trajectory.

The maximum concentration of the odor is observed around 45 s throughout the ramp when the larva is closest to the gradient's peak. Remarkably, the OSN activity reaches its maximum earlier than the stimulus intensity. The firing rate to decrease more than 5 s before the stimulus does. Moreover, small fluctuations in the stimulus intensity are dramatically amplified in the pattern of OSN activity (see time points denotes by a '*' symbol in Figure 30C).

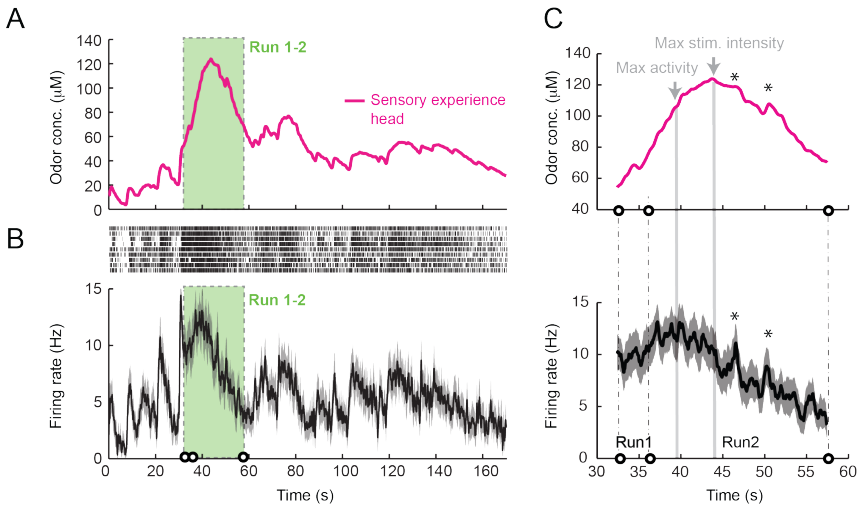

Figure 30. (A) Concentration time course corresponding to the trajectory of the head position depicted in Figure 29B. The reconstructed sensory experience is based on mapping the head positions on the reconstructed odor gradient computed upon integration of the PDE system for the entire duration of the trajectory.

(B) Raster plot of 9 suction electrode recordings for the *Or42a*>ChR2 OSN stimulated by the concentration shown in panel A (5 preparations). (Bottom) PSTH of the OSN response to the concentration time course shown in panel A with the shade representing the standard deviation.

(C) Close-up view of the sensory experience (top) and OSN response (bottom) corresponding to the illustrative runs R1 and R2 shown in panel Figure 29B (green box). Black circles on the abscissa denote turns. The input-output relationship driving the dynamics of the OSN activity is more complex than a proportional detector: the maximum firing rate is attained before the stimulus intensity reaches its maximum.

Neural firing and adaptation: Dose response

How does an OSN respond to most simple odor stimuli? To characterize the response of the OSN to the simplest kind of stimulation, binary odor pulses were used. This approach is similar to the one utilized in the characterization of OSN responses in both adult and larval *Drosophilae* (Hallem & Carlson, 2006; Kreher, Mathew, Kim, & Carlson, 2008).

Each odor pulse lasted 20 s. The OSN exhibits a transient peak in activity at the onset of the pulse (Figure 31), but then rapidly relaxes to a steady state — a clear sign of adaptation to the stimulus. The concentration range of the pulses was chosen to cover the minimum and maximum intensities observed in the odor gradient used in the behavioral experiments. Figure 31A illustrates the response elicited by odor pulses of increasing concentrations of IAA. Over the concentration range considered, the adapted steady state activity increases in a nearly linear way with the pulse concentration (Figure 33). However, this linear dose-response relationship cannot account for the response elicited by the naturalistic stimulus of Figure 30A.

A similar procedure was undertaken to obtain the responses to static light stimuli of increasing intensity evoked by ChR2. By increasing the light intensity of the pulses, an increase of the neural activity similar to the one observed for odor responses was found.

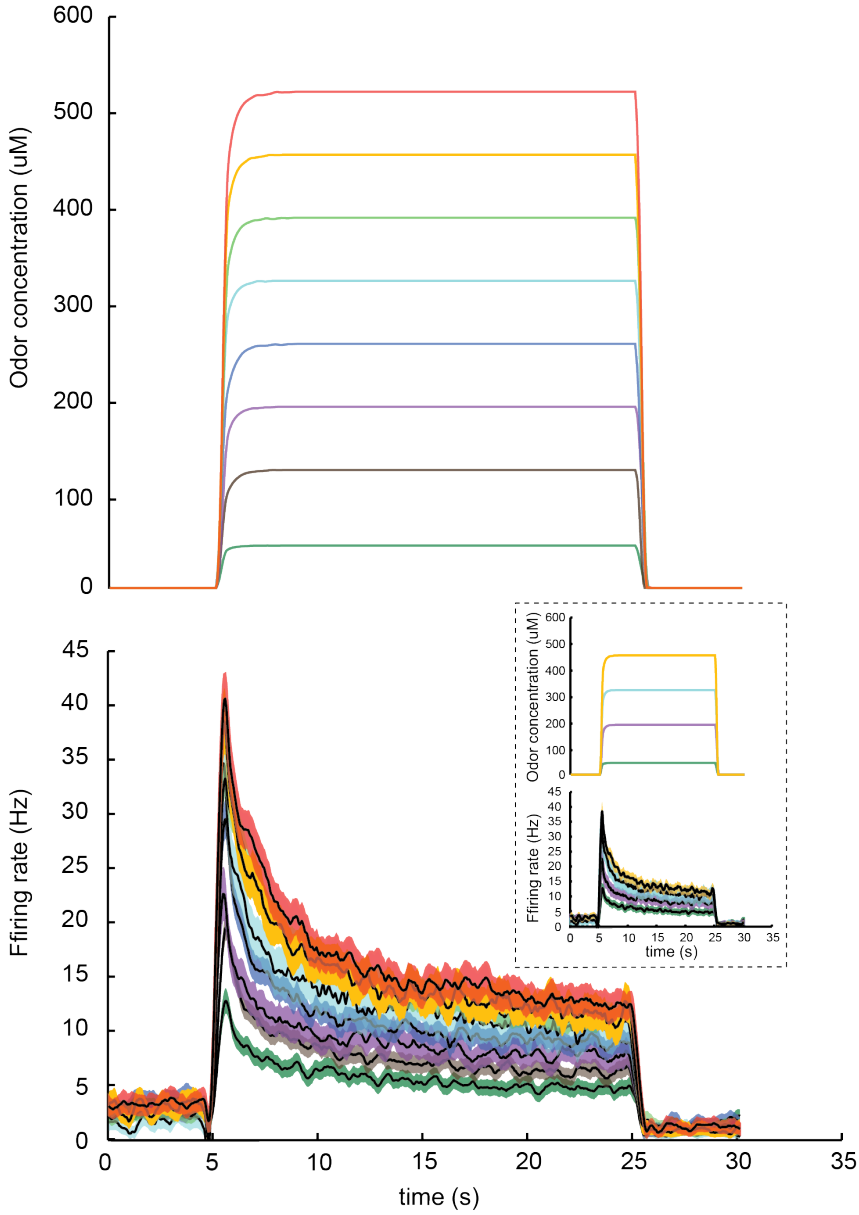

Figure 31. Dose response of the *Or42a*-expressing OSN stimulated by step pulses of increasing odor concentrations (52-522 uM). (Inset) Reduced subset of traces for clarity (same data as main figure). The data was obtained from 15 recordings conducted in 5 different preparations. Throughout the figure, shades surrounding PSTHs represent standard deviations.

The OSN adapted faster in response to light stimulation and the elicited activity was slightly weaker compared to the odor response, yet the overall response dynamics looked similar. Figure 32 illustrates the response to pulses of increasing light intensity (25 - 500 W/m^2).

In conclusion it can be seen that the neural activity in response to static odor or light stimuli does not perfectly adapt. In contrast, the steady state activity seems to scale linearly with the stimulus intensity over the range of concentrations that were tested. Although the odor dose response is hyperbolic, no saturation was observed du to the truncated odor concentration range that was used. One (technically) limiting aspect was the decreased reliability of the spike sorter with regards to very high firing rates, exemplified by odor responses to very high concentrations of IAA.

In the case of the light stimulation the neural steady state activity can be seen to saturate for higher light intensities at an activity level below the one that is observed for the odor stimulation. The light dose response also served as an important reference point for the selection of the light intensity range for all subsequent dynamic light stimulation protocols (see 'Results section; 'Linearly evolving stimuli: the influence of speed' and 'Non-linearly evolving stimuli: the influence of both speed and acceleration').

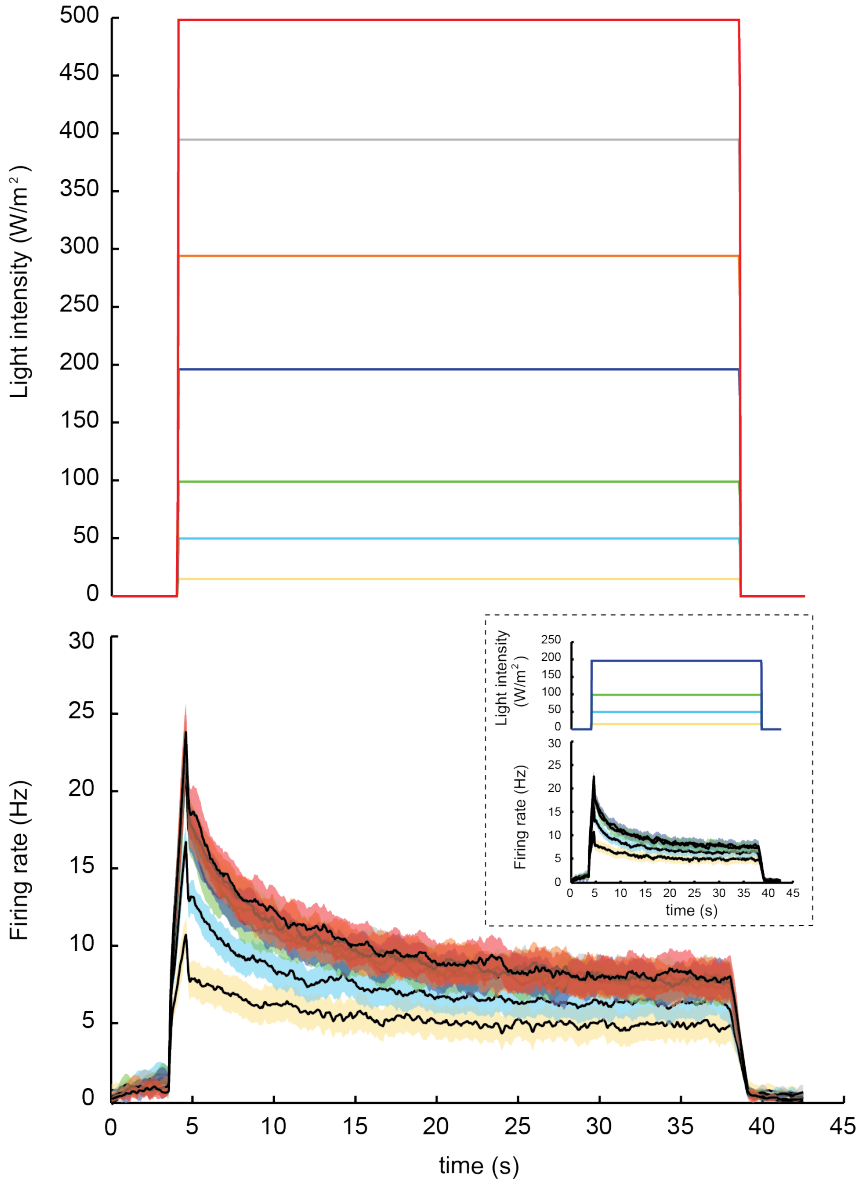

Figure 32. (B) Dose response of the *Or42a*-expressing OSN stimulated by pulses of increasing light intensities (25-500 W/m2). (Inset) Reduced subset of traces for clarity (25, 50, 100, and 200 W/m², same data as main figure). For all conditions the PSTHs were computed on a pool of 12 recordings conducted on minimum 4 preparations. Throughout the figure, shades surrounding PSTHs represent standard deviations.

They were explicitly defined for an intensity range not leading to a saturation of the ChR2-evoked light response (15 - 250 W/m^2). Following this approach it was possible to achieve light-evoked neural response profiles in response to both linear and non-linear functions that looked very similar to odor-evoked activity.

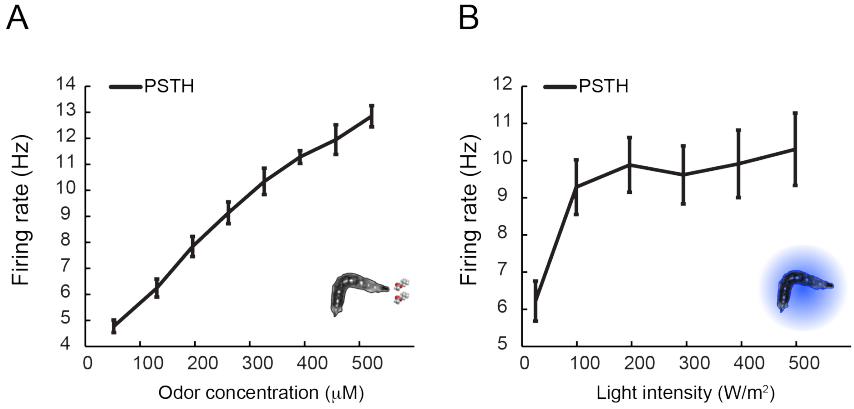

Figure 33. Experimental dose-response of the *Or42a*-expressing OSN stimulated by prolonged stationary stimulus pulses of odor and light.

(A) Odor: OSN stimulated by pulses of increasing odor concentrations (52 - 522 mM). The mean activity was measured over a 5 s-time window after relaxation of the neuron to steady state activity (computed on the data shown in Figure 31).

(B) Light: OSN stimulated by pulses of increasing light intensities (25 – 500 W/m^2). The mean activity was measured over a 10 s time window after relaxation of the neuron (computed on the data shown in Figure 32). Throughout the figure: Error bars represent the standard deviation.

Linearly evolving stimuli: the influence of speed

To systematically address how the *Or42a*>ChR2 OSN encodes changes of the stimulus time course, a property often referred to as slope sensitivity, linear odor ramps with symmetrical 8 s rising and falling phases were tested. As shown in Figure 34, the neural activity

abruptly increases during the onset of the ramp before reaching a plateau value. Increasing or decreasing the slope of the rise in stimulus by a factor 2 (Figure 35A) indicated that the plateau value reached by the OSN activity scaled with the slope of the stimulus increase. This observation suggested that the OSN is sensitive to the derivative of the stimulus intensity (speed). During the falling phase of the ramp, the neural activity rapidly drops at the transition from the rising to the falling phase before following the evolution of the stimulus value (Figure 34).

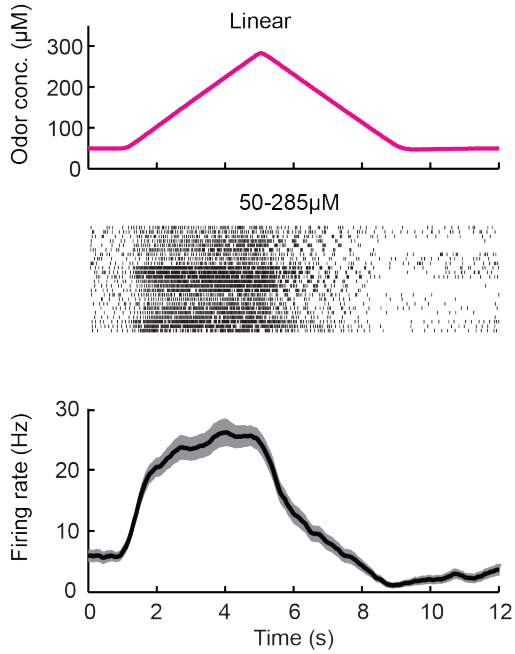

Figure 34. Response to a linear odor ramp with an equal rise and fall time of 4 s. The odor concentration (magenta) is computed from the flow ratio measured experimentally based on the flow-controller outputs. PSTH computed on a pool of minimum 24 recordings conducted in 8 different preparations. The variability across different preparations and animals can be appreciated from the raster plot. The inter-animal variability seems higher than the variability across preparations performed in the same animal. The shade surrounding PSTH represents the standard deviation.

The end of the falling phase coincides with a period of neural inhibition below baseline activity. However, the firing rate appeared to be more directly driven by the stimulus intensity rather than the stimulus derivative, suggesting that the response properties of the OSN depend on the sign of the stimulus derivative.

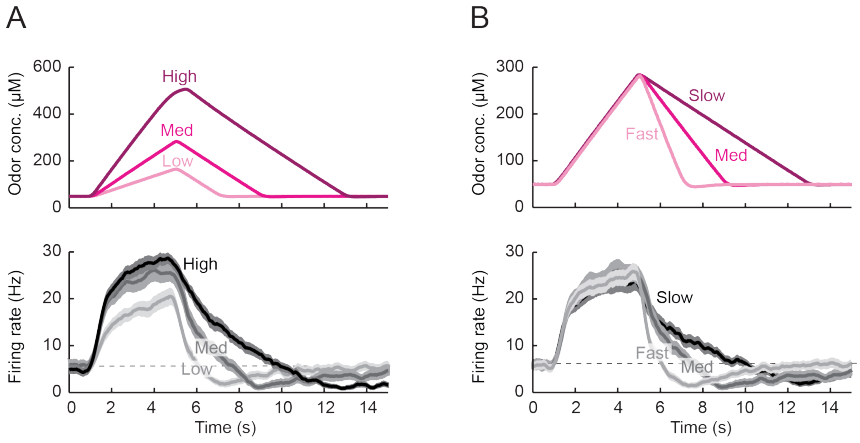

Figure 35. (A) Response to three linear ramps with variable slopes during the rise phase and equal slope during the fall phase. The 'low' ('high') ramps have a positive slope that is twice slower (faster) than the medium ramp. During the rise phase of the ramp, the activity of the OSN reaches a peak value that scales with the slope of the ramp.

(B) Response to three linear ramps with variable slopes during the fall phase and equal slope during the rise phase. The 'slow' ('fast') ramp has a negative slope that is twice slower (faster) than the medium ramp. During the rise phase of the ramp, the plateau reached by the OSN activity grows with the slope of the ramp. During the fall phase of the ramp, the activity of the OSN is more directly driven by the stimulus intensity. For the three ramps, the OSN activity becomes inhibited when the ramp terminates. Throughout the figure: The odor concentration (magenta) is computed from the flow ratio measured experimentally based on the flow-controller outputs. The PSTH is computed on a pool of minimum 24 recordings conducted on minimum 8 preparations; shades surrounding PSTHs represent standard deviations.

Variations in the slope of the falling phase corroborated this qualitative model (Figure 35B) — the more abrupt the decrease of the odor stimulation — the stronger the decline of the respective neural activity in response to the stimulus decrease.

Non-linearly evolving stimuli: the influence of both speed and acceleration

To test the sensitivity of the OSN to higher order changes of the stimulus, a series of nonlinear ramps — a quadratic, exponential, sigmoid, and asymptotic (odor and light) stimulation was tested. In the selected ramps the stimulus speed varies over time, different for each function.

For the quadratic ramp, the stimulus speed varies linearly over time: however, its second derivative (acceleration) is stationary. In response to a quadratic ramp (Figure 36B), the OSN activity can be seen to increase sharply before reaching a plateau value approximately 4 s throughout the rising phase. In comparison to the linear ramp (Figure 36A) also the decrease in neural activity is steeper in the case of the quadratic ramp.

Is there a function that is able to trigger a steady increase of the OSN activity throughout the rising phase of the ramp? This phenomenon was obtained by stimulating the OSN with an exponential ramp, featuring a monotonically increasing stimulus derivative throughout the rising phase of the ramp (Figure 36C). This acceleration correlated with a continuous increase in OSN activity.

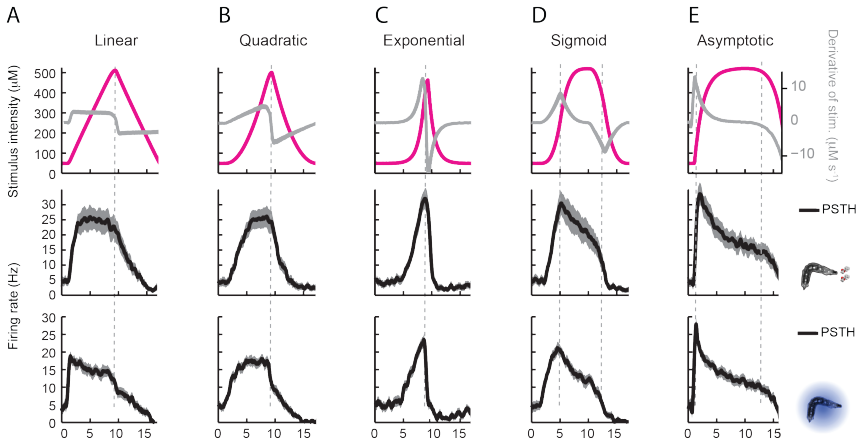

Figure 36. Response to nonlinear ramps based on a symmetrical 8s-rise and 8s-fall profiles. The ramps tested have the following characteristics: (A) linear ($\propto t$), (B) quadratic ($\propto t^2$), (C) exponential ($\propto e^{-8}(e^t-1)$), (D) sigmoid ($\propto t^3/(t^3+4^3)$), and (E) asymptotic ($1-e^{(-t/1.5)}$) with the time given in s. The odor concentration (magenta) (top panels) is computed from the flow ratio measured experimentally based on the flow-controller outputs. The same (idealized) profile was used for the light stimulation with an intensity ranging between 15 W/m² and 207 W/m². The time derivative of the concentration time course (top panels) is represented according to the y-scale on the right of the graph (gray). The derivative (top panels) was computed after mild smoothening of the stimulus input. The PSTH of the *Or42a*-OSN odor response (panels in the middle) was computed on a pool of minimum 16 recordings conducted on minimum 9 preparations. The PSTH of the light ramps (bottom panel) was computed on a pool of minimum 10 recordings conducted on minimum 10 preparations. Throughout the figure, shades surrounding PSTHs represent standard deviations.

The results suggest that the OSN is sensitive to the acceleration of the stimulus. During the falling phase of the ramp, the neural activity decreases abruptly from a peak value to a value below baseline (Figure 36C).

To individually address the sensitivity of the OSN to changes in the speed and the acceleration of the stimulus, a sigmoid and an asymptotic ramp was tested. These functions feature changes of the first and second derivative, which happen in distinct periods during the stimulation. The sigmoid displays a change in the sign of the

second derivative during the rising phase of the ramp (acceleration), which switches from positive (5-9 s) to negative (9-13 s) values (Figure 36D). The first derivative stays positive throughout the entire rising phase (5-13 s). The change in acceleration is accompanied by a transition from a temporal increase to a decrease in the OSN activity contrary to the fact that the overall stimulus increases for another 4 s (Figure 36D). The OSN adapts so fast, that the activity is unable to catch up with a decelerating stimulus increase. As a result, the OSN firing rate peaked with the first derivative and not the absolute intensity of the stimulus. During the falling phase of the ramps, the OSN firing rate behaved in a way that could not be predicted from the slope sensitivity observed during the rising phase.

In the case of the asymptotic ramp, the first derivative remains (decreasingly) positive throughout the rising phase (5-13 s), only turning negative during the falling phase whereas the second derivative starts off with a strong almost instant transition from positive to negative values at the 5 s mark approaching zero at the 13 s mark to then turn negative again (Figure 36E). Accordingly, the OSN activity continuously decreases over time as dictated by the second derivative of the stimulus. The decrease of the neural activity slows down around the 13 s mark, an observation clearly coinciding with the second derivative transiently approaching zero (Figure 36E). Taken together, these findings highlight the sensitivity of the OSN to respond to both the speed and the acceleration of the stimulus.

When comparing the activity of the OSN in response to an odor stimulus (Figure 36 panels A-E middle) to the activity elicited by light (Figure 36 panels A-E bottom it can be appreciated that the patterns of OSN activity induced by light throughout all conditions is similar to the one induced by the odor, aside from the OSN firing rate ensuing a rapid transient (linear stimulation Figure 36A) where the activity decreases instead of reaching a plateau, as is the case for the equivalent odor stimulation.

OSN responses to slow changes of the stimulus

How does the OSN respond to slowly evolving stimuli? Is the OSN response profile conserved over different time scales?

To assess the response elicited by a slowly evolving stimulus time course, the quadratic, sigmoid, and exponential light stimulation protocols were stretched to last twice as long as the original stimulation protocol (16 s rising phases as opposed to 8 s rising phases). In order to emphasize the similarities of the responses, Figure 37 depicts both conditions (middle panels 'fast' and bottom panels 'slow') simultaneously while compressing the time axis of the 16 s-time courses to match the slower stimulation time course qualitatively.

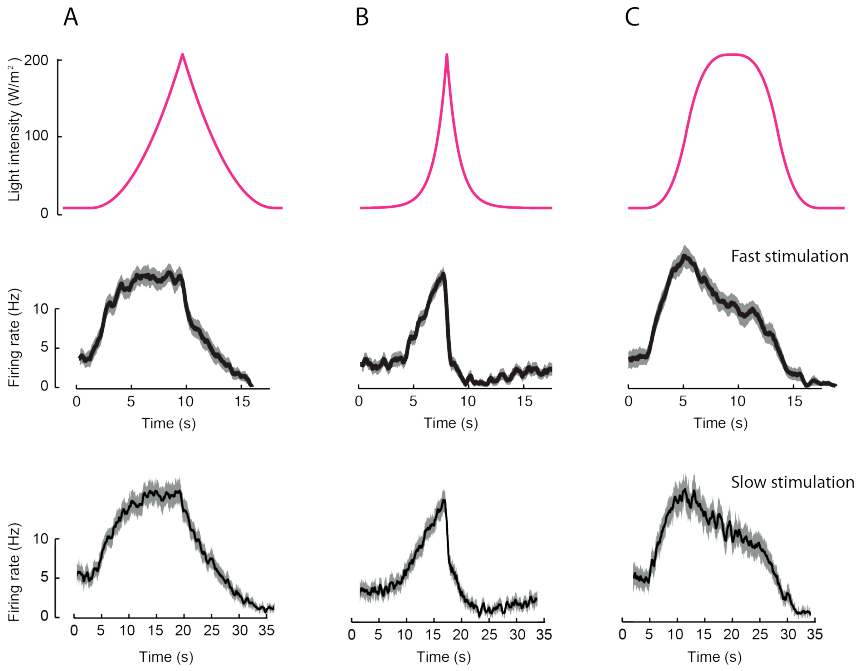

Figure 37. (A) Response to three light ramps on variable time scales. The ramps tested have the following characteristics: (A) quadratic, (B) exponential, and (C) sigmoid. The light stimulation was derived from the (idealized) odor profile shown in Figure 36 (panels B-D) with an intensity ranging between 15 W/m² and 207 W/m². The PSTH was computed on a pool of 12 recordings conducted on minimum 4 preparations; shades surrounding PSTHs represent standard deviations.

It can be appreciated from the firing rate obtained throughout all conditions, that the shape of the 'slow' response, when compressed, is still conserved in all cases. These findings support the notion that the response profile of the OSN seems to be constant over a wide range of stimulus time scales.

Modeling the OSN activity: System identification approach

To model the *Or42a* OSN input-output relationship, a standard systems identification approach was attempted by stimulating the OSN with an M-sequence (discretized version of white noise). Since fluctuations in odor concentration with high-frequency components are difficult to achieve in liquid phase, neural activity was elicited by light. The M-sequence was based on a discretization of the light intensity range 15 – 207 W/m^2 into the following 5 values: 15, 50, 100, 150 and 207 W/m^2. It featured all possible 4-element combinations of these 5 intensities.

The *Or42a*>ChR2 OSN produces consistent patterns of neural activity when stimulated with an M-sequence (Figure 38A). Rearrangement of the input and output signals in Fourier space yields a standard biphasic filter (Chichilnisky 2001; Nagel and Wilson 2011) (Figure 38 panels B and C). To test the accuracy of this filter, the activity elicited by a shorter light ramp featuring an exponential rise and decay was predicted.

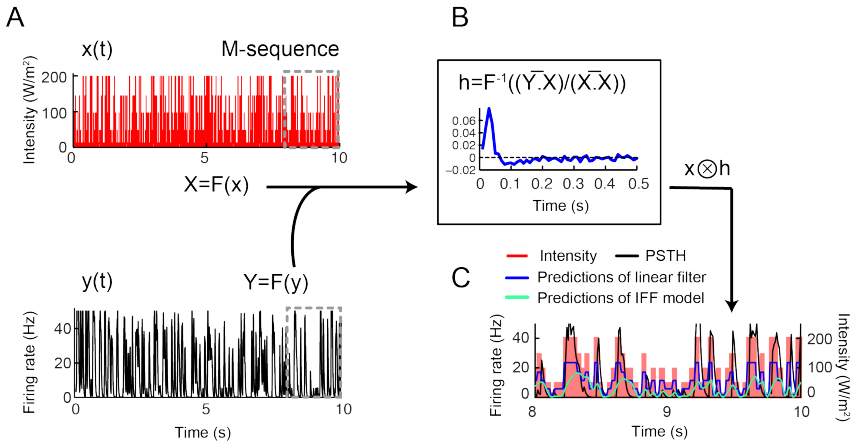

Figure 38. A linear filter alone is insufficient to account for the transfer function of the OSN.

(A) Stimulation of the *Or42a*>ChR2 OSN by a maximum-length M-sequence generated with light. In the experiments, changes in light intensity occurred with time steps of 33 ms. (Bottom) PSTH of the neural response computed over 10 trials (10 preparations) and for a bin size of 10 ms.

(B) Computation of the linear filter, h, through the operations described in panel B (Chichilnisky 2001; Nagel and Wilson 2011). Function *F* represents the Fourier transform from the time domain to the frequency domain; *F*-1 represents the inverse transformation from the frequency domain to the time domain. The bar above the variables in frequency space denotes the complex conjugate transformation. To cancel any DC drifts in the OSN response, the filter was computed on windows of 5 s slid over the entire duration of stimulus (20 s). An average filter was computed from this series (dark blue). The linear filter was used to make predictions about particular stimulus time courses.

(C) Neural activity predicted from the linear filter in response to the M-sequence. The prediction was obtained by convolving the filter with the time course of the stimulus. The resulting activity was normalized to have the same mean as the experimental activity. The result of the prediction is shown for a 2 s window of the complete stimulus (dashed gray box in panel Figure 38A). The activity predicted from the linear filter (dark blue) is compared to the predictions of the IFF model that will be introduced in Figure 40 (green). The correlation coefficient (r) of the predicted and the experimental activities is 0.37 for the linear filter reconstruction compared to 0.57 for the IFF model (the overall goodness of fit of the IFF is presented in Table 4).

Given the discrepancy between the experimentally observed activity and the prediction of the model (Figure 39 panels A and B), it was concluded that the olfactory transduction pathway within the OSN does not operate in a way that can be approximated by a linear filter.

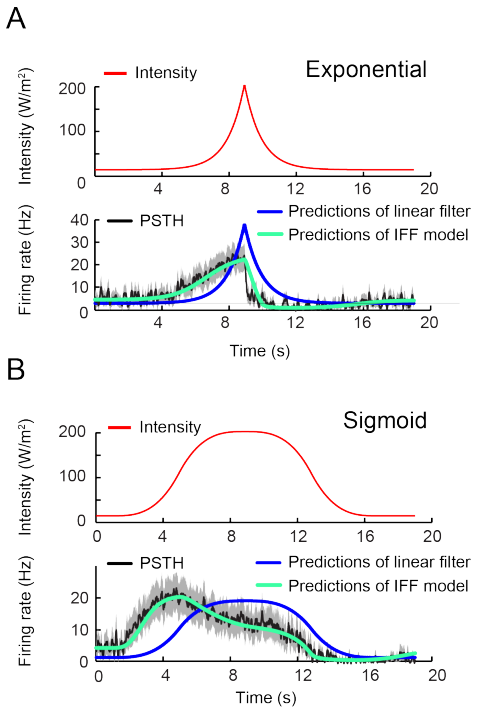

Figure 39. A linear filter alone is insufficient to account for the transfer function of the OSN.

(A) Application of the linear filter (derived from figure 38 panel C) for the M-sequence to stimulation by an exponential ramp (red). The linear filter (dark blue) fails to predict the PSTH that was observed experimentally (black line; gray shades represent the standard deviation) (r=0.56). PSTH calculated on the same set of light recordings presented in Figure 36 panels C and D for a bin size of 10 ms. Prediction of the IFF model, which will be introduced in Figure 40 shown in green (r=0.93) (the overall goodness of fit of the IFF is presented in Table 4).

(B) Application of the linear filter derived in panel C to a sigmoid ramp (red). As in panel A, the linear filter (dark blue) fails to reproduce the experimental PSTH (r=0.54) while the IFF model leads to a good fit (green, r=0.98). PSTH calculated on the same set of light recordings presented in Figure 36 panels C and D for a bin size of 10 ms. Shades surrounding PSTHs represent standard deviations.

As a consequence of the poor fit, it was decided to systematically investigate the dynamical features encoded in the activity patterns of the *Or42a*>ChR2 OSN stimulated by odor pulses, linear and nonlinear ramps.

Phenomenological model for the olfactory function of a single OSN

Given that a systems identification approach resulted in an incomplete description of the input-output relationship of the OSN, a different modeling formalism was adopted to predict the OSN firing rate. Following studies of the biophysical basis of olfactory transduction in moth and flies (Gu et al., 2009; K. I. Nagel & Wilson, 2011) a kinetic description of this input output relationship based on ordinary differential equations (ODE) was established and is discussed in the following sections[1]. Although these models represent a coarse-grained approximation of the underlying biophysical processes, a more detailed representation would not be possible due to our limited knowledge of the molecular basis of olfactory transduction and spike generation in the *Drosophila* larva. Even though the nature of the molecular mechanism driving the transduction of the ion channels formed by odorant receptor (OR) remains widely unknown, it has been suggested that negative feedback regulates olfactory transduction in adult flies — a model with strong experimental support (K. I. Nagel & Wilson, 2011).

[1] All models presented in this chapter (IFF, IFB and IFF+IFB combined) were developed by Alex Gomez-Marin and Matthieu Louis. Marco Musy and Matthieu Louis accomplished the parameter optimization of the model.

In addition, research in the moth described the dual effect of an increase in the OR activity on the spike rate (Gu et al., 2009): The primary effect takes place immediately upon the onset of the stimulus, on a short timescale, by which the inflow of cations increases the firing rate; the secondary effect kicks in on a longer timescale where an increasing concentration of intracellular calcium ions starts to decrease the firing rate through an inhibitory effect involving the binding of calcium with calmodulin. In agreement with a similar model proposed by Bargmann and colleagues (S. Kato, Xu, Cho, Abbott, & Bargmann, 2014), it was hypothesized that calcium increases the OSN firing rate by gating voltage-dependent ion channels (L-type) while decreasing the OSN activity through a delayed inhibitory effect mediated by the calcium-calmodulin complex (see 'Introduction section; The transformation of a chemical into an electrical signal: Odor transduction in ORs'). These considerations motivate a model in which the OSN activity is dynamically regulated by a combination of a negative feedback loop (or integral feedback, IFB) together with an incoherent feedforward loop (IFF) featuring fast activation and slow negative inhibition (Figure 40). Using a mass-action-kinetics formalism (Ackers, Johnsontt, & Shea, 1982; Bintu et al., 2005), the two regulatory motifs were combined in a system of 3 ODEs featuring 8 free parameters (Figure 40B, bottom).

The three variables are: x the stimulus strength (input: odor concentration or light intensity), y the instantaneous firing rate of the OSN (output), u a phenomenological intermediate variable that might represent the intracellular concentration of calcium (Figure 40D).

The stimulus strength x for the odor experiments was globally adjusted according to the phase mapping achieved through the phase conversion calcium imaging experiments (Figure 25):

$$x = x_{liquid}$$

$$x_{liquid} = x_{gas} * \rho^{\text{liquid-gas}}$$

where x_{gas} denotes the gas phase concentration that larvae were exposed to in behavioral experiments, and x_{liquid} the stimulus strength in liquid phase in which all electrophysiology experiments were conducted.

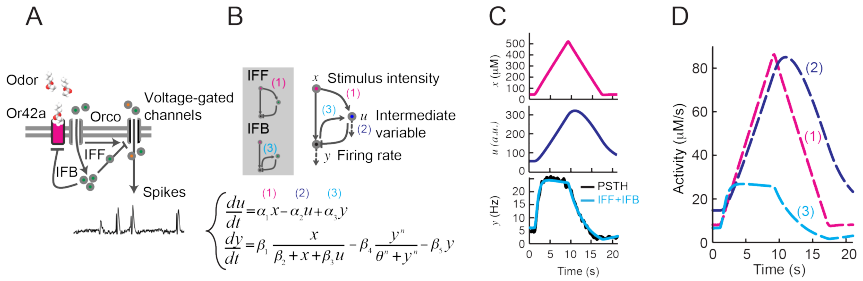

Figure 40. (A) Hypothetical physiological processes underlying the olfactory transduction pathway and spike generation. The integral feedback (IFB) motif is built on the assumption that an inhibitory feedback modulates the activity of the odorant receptor, as was proposed in the adult fly (Nagel and Wilson 2011). The incoherent feedforward (IFF) relies on the hypothetical existence of a delayed inhibitory effect on voltage-gated calcium channels, as was proposed for the transduction cascade of C. elegans (Kato, Xu et al. 2014).

(B) Abstract regulatory network combining the IFF and IFB circuit motifs described in panel A (individual motifs outlined in the gray box). Variable x represents the stimulus intensity, u the activity or concentration of the intermediate variable and y the firing rate of the neuron. The three pathways regulating the activity of u are outlined by numbers (1)-(3). Pathway (3) is specific to the IFB motif (light blue). (Bottom) ODE system providing a phenomenological description of the reaction scheme outlined in panel A for the combination of the IFF and IFB regulatory motifs.

(C) Decomposition of the predicted activity of individual pathways contributing to the regulation of u for a 8s-linear odor ramp with the stimulus variable x shown in magenta (top). Simulated concentration of u (middle) and firing rate y (bottom) upon integration of the ODE system. The PSTH is the same as the one shown in the middle panel of Figure 41.

(D) Activity computed from the terms (1) - (3) outlined in panel B for: the stimulus feedforward activation (1), first order decay (2), and coupling of the firing rate with the intermediate variable (3).

The parameters of the model were derived through a Simplex algorithm (Nelder & Mead, 1964) aiming at optimizing the fit of the model's predictions and the experimental observations for the naturalistic odor stimulation and the family of ramps considered in Figure 36. The results of the modeling are shown in Figure 41 et seq.

Incoherent feedforward (IFF) and integral feedback (IFB) motifs

The dynamics of the IFF motif described in Figure 40 can be described by a 3-variable ordinary differential equation (ODE) system. It was hypothesized that the firing rate of the OSN (*y*) results from the combined effects of direct excitation and indirect inhibition of the OSN activity. The excitation is mediated by the gating of the odorant receptor (OR) by the binding of odorant molecules or the absorption of photons by ChR2. By analogy to the olfactory transduction cascade in the moth (see 'Introduction section; The transformation of a chemical into an electrical signal: Odor transduction in ORs'), the model proposes that the indirect inhibition is mediated by an intermediate variable (*u*) that could represent the concentration of calcium bound to calmodulin. The dynamics of variable *u* results from a production term proportional to the stimulus *x* and a first-order decay term.

To model the direct excitation and indirect inhibition of the OSN activity, a control function (*d(x,u)* was used (*d* denotes depolarization) inspired from the cis-regulatory logic of gene transcription (Goentoro and Kirschner 2009):

$$d(x,u) = \beta_1 \frac{x}{\beta_2 + x + \beta_3 u}$$

This expression was built from thermodynamic considerations about the state of a promoter occupied by transcription factors (Ackers, Johnson et al. 1982; Bintu, Buchler et al. 2005). Here, it was hypothesized that a similar function is suitable to describe the depolarizing effects of the opening of the OR (or ChR2), and the

indirect hyperpolarizing effects that calcium bound to calmodulin might have on the OSN membrane. The contribution of each trend is described by x and $b_3 u$, respectively.

In addition, it was assumed that the intermediate variable u and the OSN activity y undergo a first order decay. For the OSN activity, the introduction of such a decay can be justified by speculating about the existence of ion pumps that restore the membrane to resting potential after an initial increase of cations following the gating of the OR (or ChR2) (Gu, Lucas et al. 2009). Through simulations, it was discovered that an additional constitutive decay (offset) term was needed that vanishes at a low firing rate. Although the molecular correlate of this offset remains undefined, it could be explained by the homeostatic function of ion pumps. The combined effects of the two decays is mathematically described as:

$$h(y) = -\beta_4 \frac{y^2}{y^2 + \theta^2} - \beta_5 y$$

Where h stands for hyperpolarization. To keep the model as simple as possible, the membrane potential was not modeled explicitly. Instead it was assumed that depolarizing $d(x,u)$ and hyperpolarizing $h(x)$ effects on the OSN membrane can be translated into excitatory and inhibitory effects on the OSN firing rate. While the current knowledge about the olfactory transduction cascade in *Drosophila* was insufficient to justify these assumptions, the goodness of fit resulting from the integration of the ODE model demonstrated that the OSN dynamics could be captured by the combination of $d(x,u)$

and *h(x)*. By combining the previous relationships, the following systems of ODEs were obtained:

$$\begin{aligned} \frac{du}{dt} &= \alpha_1 x - \alpha_2 u \\ \frac{dy}{dt} &= \beta_1 \frac{x}{\beta_2 + x + \beta_3 u} - \beta_4 \frac{y^2}{y^2 + \theta^2} - \beta_5 y \end{aligned} \quad (1)$$

The second regulatory motif that was considered is a negative integral feedback loop (IFB). This motif has been implicated in the process of olfactory transduction and adaptation in adult flies (Nagel and Wilson 2011). It also forms the regulatory basis of the transduction pathway underlying adaptive chemoreception in bacterial chemotaxis (Yi, Huang et al. 2000; Tu, Shimizu et al. 2008). For this motif, it was assumed that the activity of the neuron had an excitatory effect on the intermediate variable *u*, which in turn has an inhibitory effect on the OSN activity. In a first approximation, the negative feedback was assumed to be linear. The difference between the IFF and IFB motif is that the production of the intermediate variable *u* is proportional to the firing rate *y*. These considerations yielded the following system of ODEs:

$$\begin{aligned} \frac{du}{dt} &= \alpha_3 y - \alpha_2 u \\ \frac{dy}{dt} &= \beta_1 \frac{x}{\beta_2 + x + \beta_3 u} - \beta_4 \frac{y^2}{y^2 + \theta^2} - \beta_5 y \end{aligned} \quad (2)$$

Parameter fitting of IFF+IFB and pure IFF model

The application of the IFF+IFB model to a linear odor ramp is illustrated in Figure 40 (panels C and D). The prediction of the model for the OSN firing rate (cyan) is compared to the experimentally measured OSN spiking activity (PSTH, black).

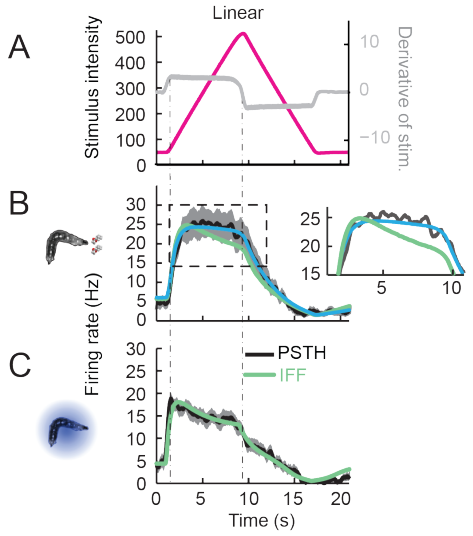

Figure 41. Fit of the solution of the ODE model on a linear stimulation ramp generated with odor and light (ramp introduced in figure 36A).

(A) Stimulus intensity given as odor concentration (uM). The time derivative of the concentration profile (gray) is represented according to the ordinate on the right of the graph. The derivative was computed after mild smoothening of the stimulus time course. The same (idealized) profile was used for the light stimulation with an intensity ranging between 15 W/m² and 207 W/m².

(B) Results of the model compared to the odor-evoked OSN activity. Close-up view of the 8 s linear ramp highlighting the difference in the behavior of the pure IFF (green) and combined IFF+IFB (cyan) circuit motifs for the odor stimulation. The PSTH of the odor response (panel in the middle) is the same as the one shown in figure 36A (middle).

(C) Comparison of the outcome of the experimental PSTH and model based on a pure IFF motif (green) for the light stimulation. The PSTH of the light ramp (bottom panel) is the same as the one shown in figure 36A (bottom). Throughout the figure, shades surrounding PSTHs represent standard deviations; parameters were obtained through a Simplex parameter optimization.

As the contribution of the IFB motif on the dynamics of variable *u* is approximately 30% that of the IFF (cyan versus magenta curves, Figure 40D), it was concluded that the IFF pathway dominates the control of the OSN spiking activity with the IFB pathway nonetheless contributing to the dynamics.

The application of the IFF and the IFF+IFB model to a linear odor and light ramp is further illustrated in Figure 41. The non-negligible contribution of the IFB motif on the odor-evoked OSN activity can be appreciated on the odor ramp which illustrates that the fitness of the model decreased when the IFB pathway was artificially disabled from the ODE model (green line, inset of Figure 41B). The prediction of the pure IFF model (green) and the combined IFF+IFB model for the OSN firing rate (cyan) is compared to the experimentally measured OSN firing rate (PSTH, black). Figures 41-43 establish that the composite model leads to a remarkably good fit over a wide range of different stimulation conditions (experimental PSTH — black line, prediction of the IFF+IFB model — blue line, prediction of the IFF model alone — green line). The goodness of fit of the IFF and the combined IFF+IFB model is quantified in Table 4.

Overall, the activity patterns elicited by light ramps was similar to those elicited by odor ramps; the pure IFF model lead to a remarkably good fit (Figures 42 and 43). As for the linear ramps, the termination of the nonlinear ramps induced a short phase of inhibition below baseline.

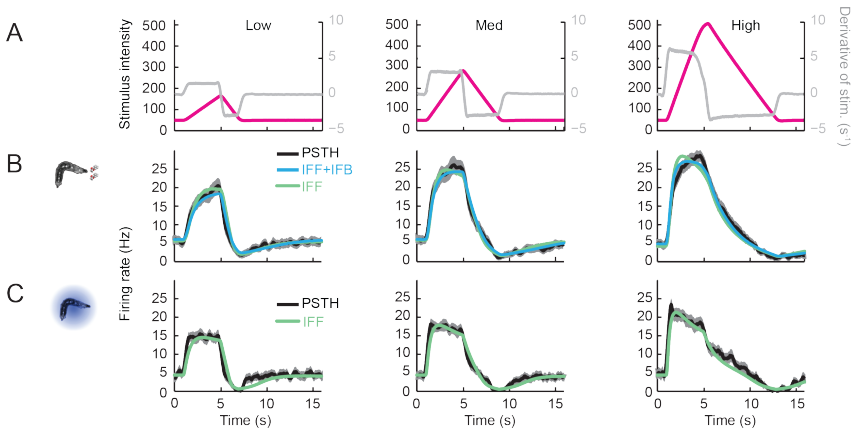

Figure 42. Fit of the solution of the ODE model for three linear stimulation ramps introduced in Figure 35A.

(A) Stimulus intensity given as odor concentration (uM). The time derivative of the concentration profile (gray) is represented according to the ordinate on the right of the graph. The derivative was computed after mild smoothening of the stimulus time course. The same (idealized) profile was used for the light stimulation with an intensity ranging between 15 W/m^2 and 207 W/m^2.

(B) Results of the model compared to the odor-evoked OSN activity: Comparison of the outcome of the model featuring a pure IFF motif (green) and a combination of the IFF and IFB motifs (cyan) for the odor stimulation. The PSTH of the odor response (panels in the middle) are the same as the ones shown in figure 35A.

(C) Results of the model compared to light-evoked OSN activity: Comparison of the outcome of the model featuring a pure IFF motif (green) for the light stimulation. Parameter optimization shows that the IFB motif does not contribute to the light-evoked OSN dynamics. The PSTH of the light ramps was computed on a pool of minimum 10 recordings conducted on minimum 10 preparations. Throughout the figure, shades surrounding PSTHs represent standard deviations; parameters were obtained through a Simplex parameter optimization.

The suppression of the OSN activity was well captured by the IFF model, even though the strength of the suppression is stronger than that observed upon stimulation by the odor (Figures 41 and 42). From the ODE system presented in Figure 40 and in equations (1)-(2), it becomes clear that the time derivative of u can be multiplied by an arbitrary scaling factor reabsorbed by the fitting parameter b_3 in the time derivative of y. For this reason it was necessary to fix one of the parameters to a constant value. For numerical convenience a_1 was set to a_1=0.1.

To infer the actual value of this parameter, one would have to experimentally access the value of the intermediate variable u, whose molecular identity remains yet unknown. For the pure IFF model, the number of free parameters was 7. In addition to these parameters, the scaling of the firing rate y elicited by individual stimulation protocols was considered via a multiplicative factor accounting for variability across experimental conditions (e.g. minute differences in the positions of the stimulation pipette).

The maximization of the likelihood function was achieved by means of the Nelder-Mead (NM) method (Nelder and Mead 1965), which proved to be fast and reliable. The result of the NM optimization was then refined through a gradient search algorithm (Brun and Rademakers 1997). For the dataset corresponding to the light stimulation, the result of the fitting procedure, yielding a probability of χ^2 very close to zero, was able to rule out the relevance of the IFB model alone. In contrast, the IFF was able to reproduce the experimental observation with good accuracy.

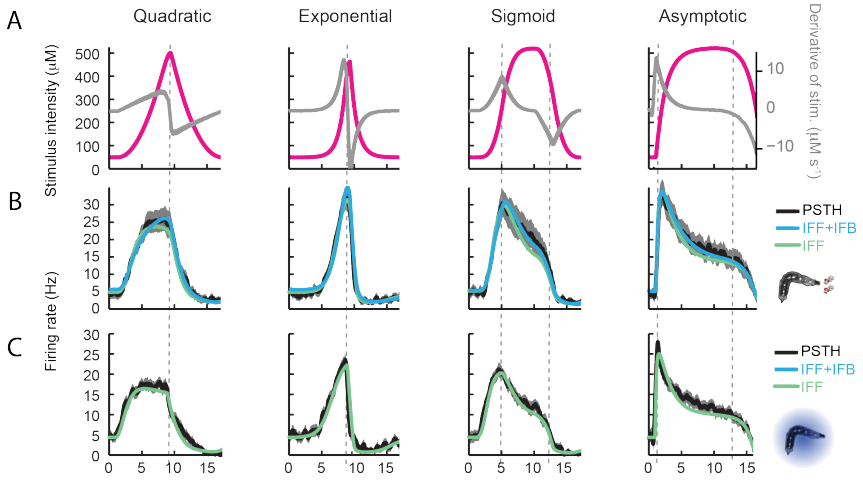

Figure 43. Fit of the solution of the ODE model for four nonlinear stimulation ramps generated with odor and light (ramps introduced in Figure 36 panels B-E).

(A) Stimulus intensity given as odor concentration (uM). The time derivative of the concentration profile (gray) is represented according to the ordinate on the right of the graph. The derivative was computed after mild smoothening of the stimulus time course. The same (idealized) profile was used for the light stimulation with an intensity ranging between 15 W/m² and 207 W/m².

(B) Results of the model compared to the odor-evoked OSN activity. Comparison of the predictions for the pure IFF (green) and combined IFF+IFB (cyan) circuit motifs for the odor stimulation. The PSTH of the odor response are the same as the ones shown in figure 36 B-E (middle).

(C) Comparison of the outcome of the experimental PSTH and model based on a pure IFF motif (green) for the light stimulation. The PSTH of the odor response are the same as the ones shown in Figure 36 B-E (bottom). Throughout the figure, shades surrounding PSTHs represent standard deviations.

In the case of the odor stimulation, a significant improvement of the model fit was obtained by adding an IFB component to the IFF motif. In the expression of the time derivative of u, the term $a_3 y$ was added. The fitted value of the composite IFF+IFB motif indicated that the IFB component was not negligible during the stimulation and could account for about 30% of the final firing rate (Figure 38). In contrast to the pure IFF model, variables u and y of the IFF+IFB

model were entangled in the structure of the ODE resulting in a coupling that allowed for a fit of the value for parameter a_1. The effect of introducing additional terms in the denominator of the function defining y, such as the product uy was also examined. Besides the test of other circuit motifs, the introduction of additional free parameters represented a qualitative test against the possibility of over-fitting. The improvements in the fitting obtained in these cases were very marginal.

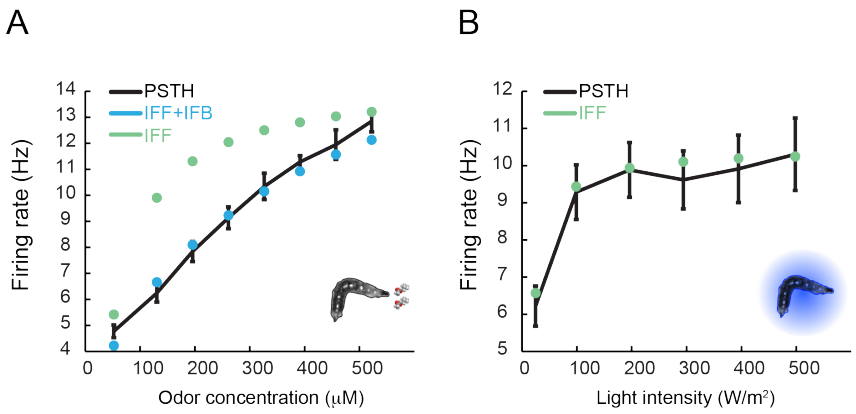

Figure 44. Predicted and experimental dose-response of the *Or42a*-expressing OSN stimulated by prolonged stationary stimulus pulses of odor (A) and light (B) (based on the electrophysiological data reported in figures 27 - 29).

(A) Dose response of the *Or42a*-expressing OSN stimulated by pulses of increasing odor concentrations (52 - 522 mM) (same data is shown in figure 33A). Activity predicted by the model for the pure IFF (green) and combined IFF+IFB (cyan) motifs upon optimization of the parameter for the linear and nonlinear ramps shown in Figures 41-43 (middle) (same data is shown in figure 33A).

(B) Dose response of the *Or42a*-expressing OSN stimulated by pulses of increasing light intensities (25 - 500 W/m²). Activity predicted by the model for the pure IFF motif (blue) upon optimization of the parameter for the linear and nonlinear ramps shown in Figures 41-43 (bottom) (same data is shown in figure 33B). Throughout the figure: Error bars represent the standard deviation.

With regards to both light and odor stimulation protocols, the data comprised stimulation patterns on diverse timescales and with varying stimulus durations: 10 linear and nonlinear ramps (Figures 41-43) lasting less than 25 s and a 'naturalistic' stimulus lasting more than 200 s (Figure 30).

It was found that the parameter set leading to a good fit during the first 30 s of the light or odor stimulation did not yield an accurate fit for longer times. By fitting the activity at the beginning and the end of the naturalistic stimulation, it was discovered that the discrepancy between both time ranges was mainly due to a change in the threshold q of the Hill term in the time derivative of y (equation 1). Therefore, the threshold q was allowed to change smoothly between the two different time ranges with the functional expression: $\theta' = \theta\ (\tau/t)^2$ for $t > \tau$ with t=30 s.

A third set of measurements of the firing rate at steady state (Figure 44) was used as an independent control of the parameter fit obtained from the fitting of the other stimulation protocols (for the detailed results of the OSN firing rate in the dose response see Figures 31-33).

Two metrics were used to quantify the goodness of fit of the model for the OSN firing rate. First, Pearson's correlation coefficient was used where the experimental observations were denoted as X_t and the output from the model as Y_t. The final correlation coefficient was computed as:

$$r = \frac{\sum_{t=1}^{n}(X_t - \overline{X})(Y_t - \overline{Y})}{s_X\, s_Y}$$

where s_X is the standard deviation of variable X and n represents the total number of time points in the dataset. The second metric used is the coefficient of variation of the root-mean-square error defined as (results of the goodness of fit are summarized in table 4):

$$CV(RMSE) = \frac{\sqrt{\frac{1}{n}\sum_{t=1}^{n}(X_t - Y_t)^2}}{\overline{X}}$$

Table 4. Quantification of the goodness of fit of the IFF and IFB models against the experimental data.

(A) Comparison between the ODE models and the experimental OSN firing rate through Pearson's correlation coefficient computed over the duration of the stimulus ramp listed in Figures 58 and 59.

(B) Comparison between the ODE models and the experimental OSN firing rate through the coefficient of variation (CV) of the root-mean-square error (RMSE) computed over the duration of the stimulus ramp listed in Figures 58 and 59.

A

Correlation coefficient	Odor, IFF	Odor, IFF +IFB	Light, IFF
Linear (4s), low	0.982	0.985	0.954
Linear (4s), med	0.994	0.994	0.980
Linear (4s), high	0.986	0.995	0.983
Linear (4s), slow	0.993	0.994	0.980
Linear (4s), fast	0.983	0.979	0.970
Linear (8s)	0.983	0.994	0.982
Quadratic	0.993	0.993	0.988
Exponential	0.990	0.984	0.965
Sigmoid	0.985	0.994	0.990
Asymptotic	0.990	0.994	0.972

B

CV(RMSE)	Odor, IFF	Odor, IFF +IFB	Light, IFF
Linear (4s), low	0.143	0.121	0.225
Linear (4s), med	0.112	0.097	0.174
Linear (4s), high	0.159	0.093	0.184
Linear (4s), slow	0.111	0.091	0.167
Linear (4s), fast	0.173	0.179	0.229
Linear (8s)	0.185	0.106	0.153
Quadratic	0.131	0.111	0.150
Exponential	0.155	0.226	0.237
Sigmoid	0.175	0.102	0.131
Asymptotic	0.124	0.080	0.193

OSN responses to rapidly changing stimuli

Before executing turns to head towards an increasing odor concentration a larva typically stops and executes a series of head casts to sample its immediate environment. Contrary to runs, where a larva experiences slowly evolving changes in odor concentration, during sampling, an animal gathers fast changes of the stimulus intensity during a short period of time. How are these fast-changing stimuli captured by the OSN?

When categorizing larval head casts during chemotaxis, they naturally come in two flavors: head casts executed in the direction of increasing intensity, and those occurring in the direction of decreasing concentration. Most head casts occur in the direction of increasing odor concentration (positive head casts) and only a minority of casts happens in the direction of decreasing intensity (negative head casts). Through a head cast, a larva is able to detect changes in concentration of 100 nM (air-phase) over a time course of 0.5 - 1.5 s (Gomez-Marin, Stephens et al. 2011). Depending on the background concentration present at the time of a given head cast the detected change of odor concentration corresponded to approximately 5 - 50% over the background concentration.

Whenever the last head cast was associated with a concentration increase exceeding 50 nM (air-phase), the likelihood of turning towards the higher odor concentration exceeds 80% indicating that the larva previously detected the increase in concentration while it was sampling its environment (Gomez-Marin, Stephens et al. 2011).

In a first set of experiments the stimulus time course during a head cast was assumed to capture

(1) a fast linear increase in odor concentration followed by a fast linear decrease bringing it back to the starting concentration (up-gradient);
(2) a fast linear decrease in odor concentration followed by a fast linear increase bringing it back to the starting concentration (down-gradient).

When presenting a real odor stimulus, the stimulus time course was governed by the technical limitation of the odor delivery system. The stimulus time course was thus chosen according to the fastest change the pressure-driven flow controller was technically able to accomplish with high reliability. The OSN response to fast linear changes in odor concentration on a time scale similar to a larval head cast is shown in Figure 45.

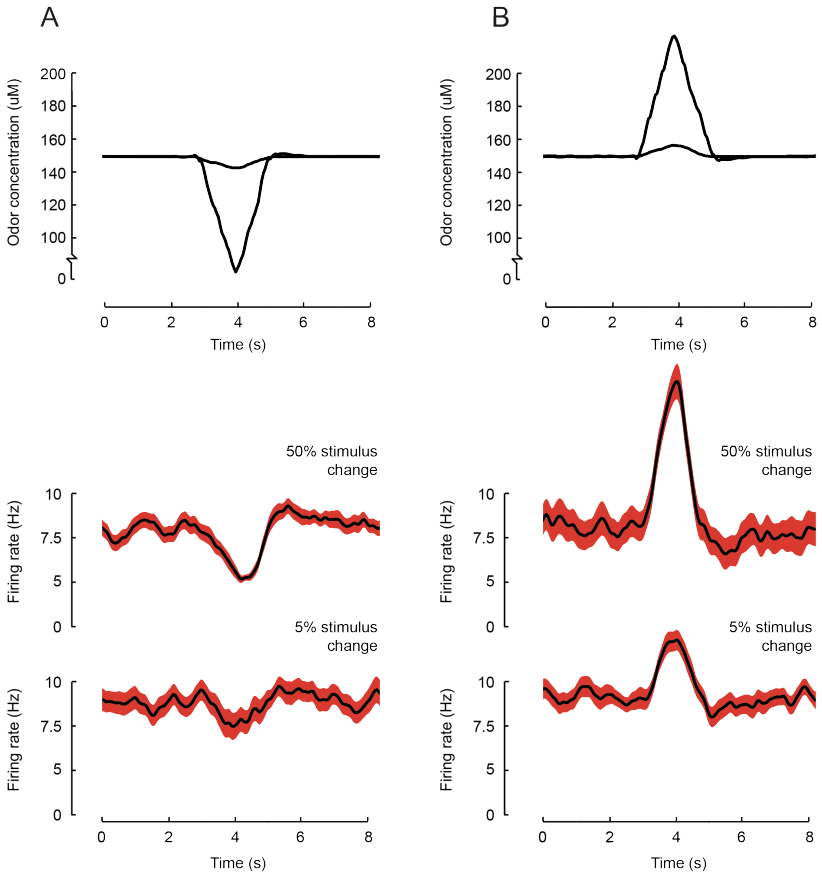

Figure 45. *Or42a*-OSN response to rapidly evolving odor stimuli. The stimulus intensity is given as odor concentration (uM). Rapid changes of the stimulus were conducted after relaxation of the neuron to steady state activity.

(A) OSN response to rapid linear negative changes of the stimulus time course (5% and 50% stimulus change with respect to the background concentration).

(B) OSN response to rapid linear positive changes of the stimulus time course (5% and 50% stimulus change with respect to the background concentration). The stimulus change is reported with respect to the background stimulation. Throughout the figure, the PSTH was computed on a pool of minimum 12 recordings conducted on minimum 4 preparations; shades surrounding PSTHs represent standard deviations.

When comparing the stimulation time course happening during a positive head cast (Figure 45B) with its negative counterpart (negative head cast, Figure 45A) one can see that the OSN seems to respond more vividly to the former compared to the latter — an observation concurring with the finding that most sampling events occur first in the direction of a positive concentration change (Gomez-Marin, Stephens et al. 2011). The OSN's response appears to be asymmetric with regards to positive and negative changes of the stimulus intensity with a minor bias towards positive changes.

Building upon the remarkable resemblance of the OSN response dynamics in response to both odor and light stimuli, a more intricate investigation of the encoding of rapidly evolving stimuli was performed using light evoked activity as approximation of odor-evoked activity. This approach granted both superior temporal resolution and a more precise control of the stimulus time course compared to the liquid phase odor delivery system used in this project. Figure 46 shows the OSN response experienced during a positive head cast. The stimulus features a rapid (500 ms) positive linear change over the background intensity (2.5 - 20 % with respect to the background intensity).

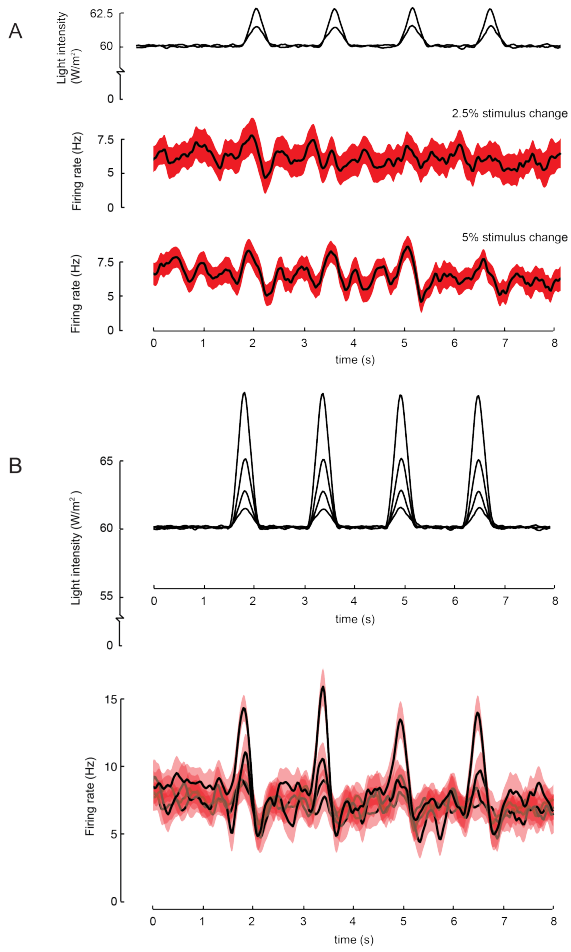

Figure 46. *Or42a*-OSN response to rapidly evolving positive light stimuli. The stimulus intensity is given as light intensity (W/m^2). The stimulus change is reported with respect to the background stimulation. Rapid changes of the stimulus were conducted after relaxation of the neuron to steady state activity.

(A) OSN response to rapid linear positive changes of the stimulus time course (2.5% and 5% stimulus change). A detectable OSN response is only observed for minimum 5% change of the stimulus (same observation as in Figure 47).

(B) OSN response to rapid linear positive changes of the stimulus time course (2.5, 5, 10, and 20% stimulus change). Throughout the figure, the PSTH was computed on a pool of minimum 10 recordings conducted on minimum 2 preparations; shades surrounding PSTHs represent standard deviations.

Figure 47 shows the corresponding response profile corresponding to a negative head cast. The minimum change of the stimulus intensity to cause a detectable change of the OSN firing rate appears to be 5% for both positive and negative head casts (Figure 46A and 47A). The notion that the OSN responds asymmetrically to positive and negative stimuli is likewise supported by these findings.

When observing larval behavior during chemotaxis it becomes clear that the categorization of head casts into 'left'or 'right' does not hold true for all head casts. Instead, there are a number of casting events that are not rightfully captured by this metric: i.e. in cases where a first sweeping to the left continues towards the right without interrupting the movement at all. When considering these cases (Gomez-Marin, Stephens et al. 2011), head casts can be categorized into

(1) those experiencing positive changes followed by negative changes (up-down);
(2) those experiencing negative changes followed by positive changes (down-up).

Figure 48 shows the observed OSN firing rate for both cases (5 % and 10 % changes over the background concentration, respectively) while Figure 49 illustrates the corresponding more simple only-up or only-down casts.

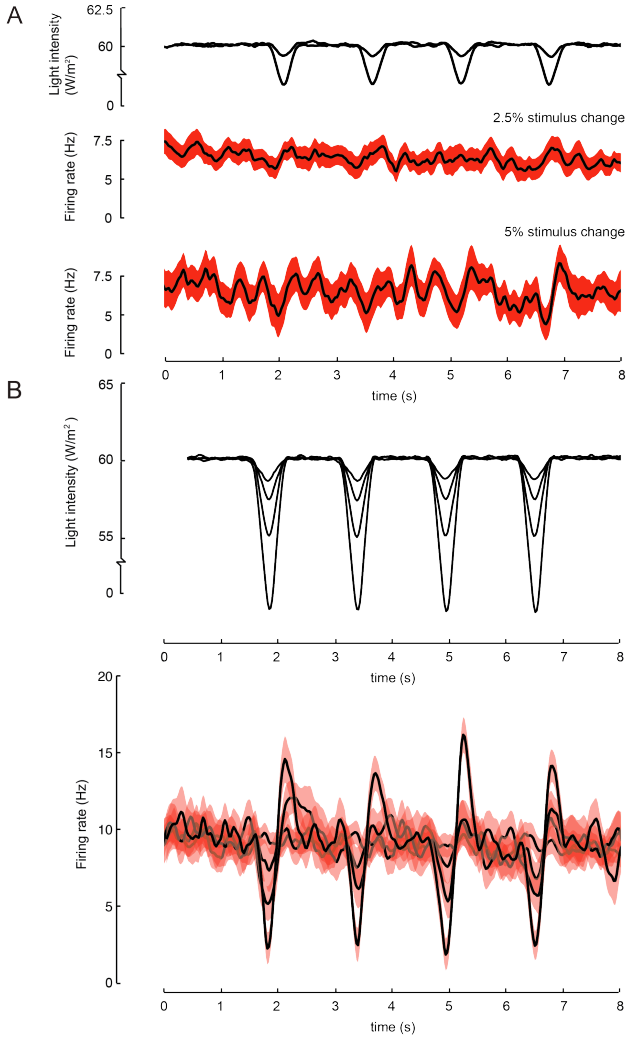

Figure 47. *Or42a*-OSN response to rapidly evolving negative light stimuli. The stimulus intensity is given as light intensity (W/m²). The stimulus change is reported with respect to the background stimulation. Rapid changes of the stimulus were conducted after relaxation of the neuron to steady state activity.

(A) OSN response to rapid linear positive changes of the stimulus time course (2.5% and 5% stimulus change). A detectable OSN response is only observed for minimum 5% change of the stimulus (same observation as in Figure 46).

(B) OSN response to rapid linear negative changes of the stimulus time course (2.5, 5, 10, and 20% stimulus change). Throughout the figure, the PSTH was computed on a pool of minimum 10 recordings conducted on minimum 2 preparations; shades surrounding PSTHs represent standard deviations.

In the first case (1) the OSN response features a more prominent inhibition of the activity in response to the stimulus transition from high to low. In the second case (2) the OSN shows less inhibition and stronger activation in response to the stimulus transition from low to high.

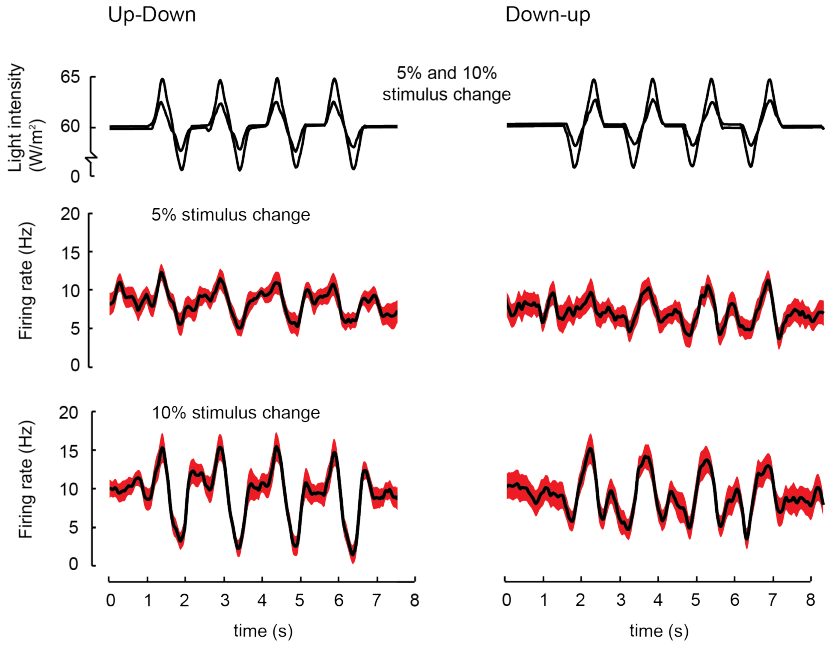

Figure 48. Probing the symmetry of the *Or42a*-OSN response to rapidly evolving light stimuli through inverted stimulus time courses (up-down and down-up). The stimulus intensity is given as light intensity (W/m^2). The stimulus change is reported with respect to the background stimulation. Rapid changes of the stimulus were conducted after relaxation of the neuron to steady state activity.

(Left) OSN response to rapid linear changes (up-down) of the stimulus time course (5% and 10% stimulus change).

(Right) OSN response to rapid linear changes (down-up) of the stimulus time course (5% and 10% stimulus change). Throughout the figure, the PSTH was computed on a pool of minimum 10 recordings conducted on minimum 2 preparations; shades surrounding PSTHs represent standard deviations.

While the maximum firing rate reached by the OSN is identical in both cases, the overall change in neural activity is more prominent in the first case (1) where the difference of the minimum and maximum activity for 10 % changes over the background is 14 Hz.

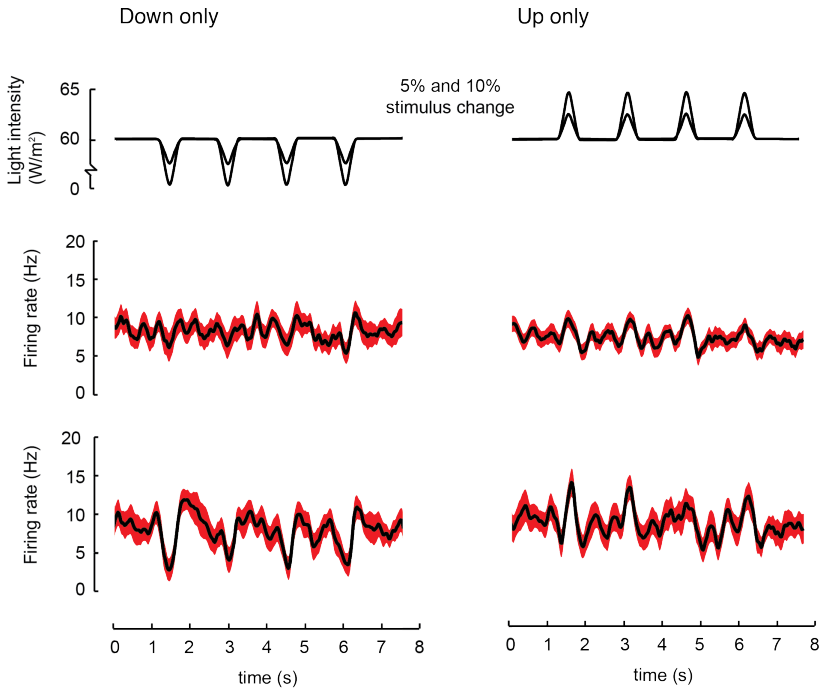

Figure 49. Probing the symmetry of the *Or42a*-OSN response to rapidly evolving light stimuli through inverted stimulus time courses (down-only and up-only). The stimulus intensity is given as light intensity (W/m^2). The stimulus change is reported with respect to the background stimulation. Rapid changes of the stimulus were conducted after relaxation of the neuron to steady state activity.

(Left) OSN response to rapid linear changes (down-only) of the stimulus time course (5% stimulus change: middle panel, and 10% stimulus change: bottom panel).

(Right) OSN response to rapid linear changes (up-only) of the stimulus time course (5% and 10% stimulus change). Throughout the figure, the PSTH was computed on a pool of minimum 10 recordings conducted on minimum 2 preparations; shades surrounding PSTHs represent standard deviations.

In the latter (2) case the difference between the minimum and maximum activity for 10 % changes over the background is only 10 Hz. Once again, these results coincide with the observation that the majority of head casts occur towards the side of higher concentration. When comparing the responses to the more simple up-only and down-only head casts, the OSN response is crisper in the case of uninterrupted up-down and down-up casts. Overall it seems that larvae adopt a sampling pattern, which optimizes the detectability of a changes in the stimulus intensity as sensed by OSNs.

Does the OSN perform fold-change detection?

Larvae carrying only a single pair of functional OSNs are still able to efficiently perform chemotaxis over a broad range of odor concentrations. How are OSNs capable of detecting changes of the odor gradient that allow animals to accurately track odors over this broad range of concentrations?

More than 150 years ago, the physician Ernst Heinrich Weber proposed that in observing the disparity between things that are compared, it is not the difference between the things that is perceived, but rather the ratio of this difference to the magnitude of things compared. As a result, the discrimination threshold, or the threshold for detecting an increment in the intensity, changes depending on how much intensity there is i.e. in the background before the increment occurs (Fancher and Rutherford 2012). Experiments in the visual system have shown that the retina

produces approximately the same response for two visual displays that are related by a simple proportional scaling of all intensity values according to Weber's Law (Barlow and Levick 1969; Meister and Berry 1999). Recently, Goentoro et al. studied cellular responses that depended on the fold-change in the input signal, and not on its absolute level (Goentoro and Kirschner 2009). They found a fold-change detection feature in signaling systems in cells and identified it as a feature of Weber's Law; a response proportional to the fold-change in the stimulus relative to the background. As a result, the amplitude and duration of such a response would depend only on fold changes in input and not on absolute levels of the stimulus (Shoval, Goentoro et al. 2010). It should be noted that although fold-change detection generally entails Weber's law, this is not necessarily true for the reverse case. Weber's law — even with exact adaptation — does not always enable to fold-change detection (Shoval, Goentoro et al. 2010).

Is a single OSN capable of performing fold-change detection?

To assess whether the OSN encodes relative rather than absolute changes of the stimulus intensity, experiments featuring three sigmoidal stimulus time courses — all starting off at different baseline intensities — were conducted. The light stimulation profile with the shape of a sigmoid was designed such that the relative change in intensity (3 fold) was kept constant throughout all three stimulation conditions:

(1) 15 W/m^2 to ramp up to 45 W/m^2
(2) 75 W/m^2 to ramp up to 225 W/m^2,
(3) 150 W/m^2 to ramp up to 450 W/m^2

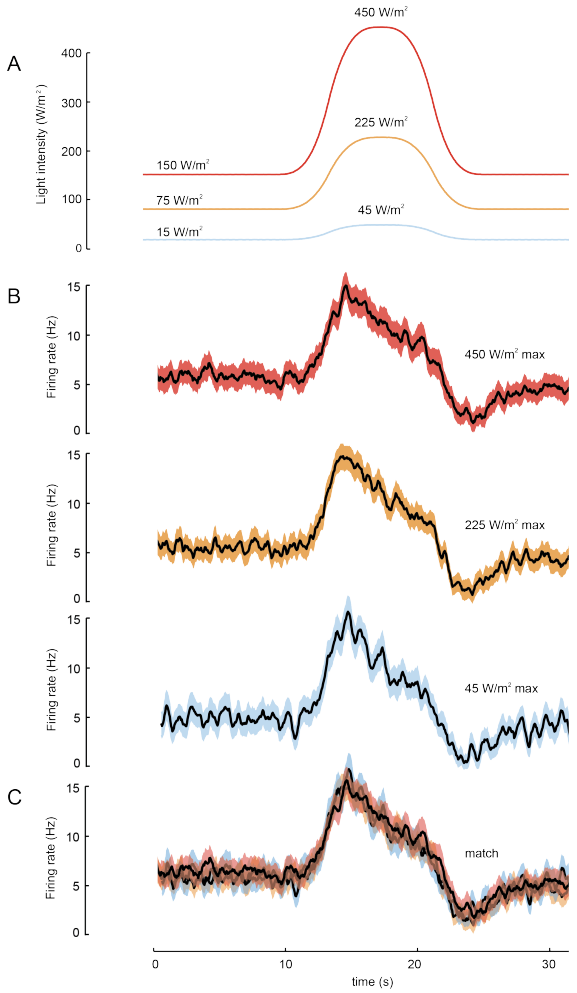

Figure 50. Testing the *Or42a* OSN response to whether it encodes relative rather than absolute changes of the stimulus intensity (light).

(A) The stimulus intensity is given as light intensity (W/m²). The sigmoid light stimulation was conducted after relaxation of the neuron to steady state activity.

(B) OSN response (PSTH) to a sigmoid stimulation featuring a three fold increase of the stimulus intensity starting from different baseline intensities (top: 15 - 45 W/m², middle: 75 -225 W/m², bottom: 150 - 450 W/m²).

(C) Superimposition of all three PSTHs while correcting for the small offset of the baseline activity. The individual OSN responses become literally indistinguishable from one another. Throughout the figure, the PSTH was computed on a pool of minimum 20 recordings conducted on minimum 8 preparations; shades surrounding PSTHs represent standard deviations.

As can be seen from the PSTHs shown in Figure 50B, the OSN response dynamics are similar both qualitatively and quantitatively in all conditions. When superimposing the OSN response while correcting for the small offset of the baseline activity, they are almost indistinguishable from one another (Figure 50C).

In a second set of experiments the stimulus intensity was elevated sequentially in a staircase-like fashion. As a result, the neural activity was allowed to adapt after the first stimulus increase. The second increase then triggered a neural response starting from a new (elevated) background intensity. The staircase featured different types of stimulation protocols (step, linear, and sigmoid) to test how qualitatively different stimulus time courses impact the neural response profile.

The neural activity is most vividly elevated in response to the first step-like increase in stimulus intensity (Figure 51A). The second stimulus increase, although identical to the first one in absolute terms, triggers a response that is smaller compared to the first one. Since the second stimulus increase starts off from much higher baseline intensity, this observation is to be expected considering Weber's proposition of keeping track of the relative increase in intensity rather than the absolute.

Beyond the notion of fold-change detection, the results shown in Figure 51 also emphasize that the main component affecting the neural response profile is the temporal shape of the stimulus time course. While a step-like stimulus triggers a spiky, rapidly adapting response, the neural responses are more graded and smoother in response to a linear and sigmoidal increase (Figure 51).

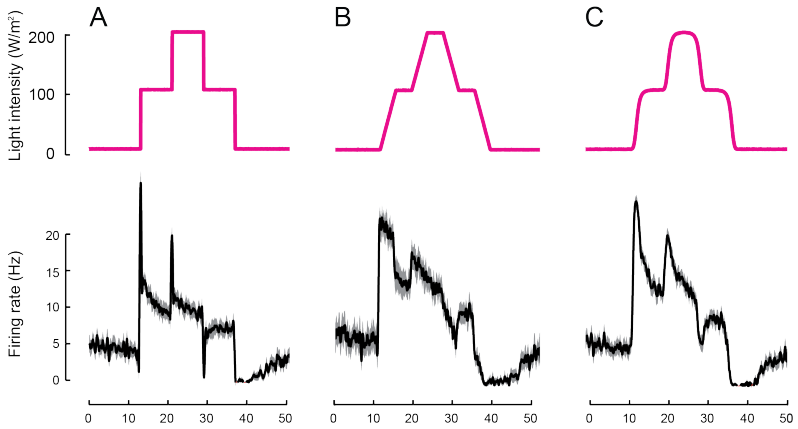

Figure 51. Assessing the ability of the *Or42a* OSN response to track relative changes of the stimulus intensity through staircases of light stimulation. The stimulus intensity is given as light intensity (W/m^2). The staircase stimulation was conducted after relaxation of the neuron to steady state activity. OSN response (PSTH) to an ideal (A), linear (B), and sigmoid (C) staircase light stimulation featuring a fixed increase of the stimulus intensity. Throughout the figure, the PSTH was computed on a pool of minimum 10 recordings conducted on minimum 2 preparations; shades surrounding PSTHs represent standard deviations.

Taken together, these results support the notion that even a single OSN is capable of tracking relative changes of the stimulus intensity making it possible for animals to successfully navigate through a broad range of odor gradients. Future work will have to show whether these findings, which were obtained with light recordings, also hold for real odors.

Behavior

Controlling larval behavior: Closed loop tracking experiments

Can we make predictions about larval behavior purely on the basis of the known neural activity of a single OSN? The preceding sections discussed the most prominent dynamic features found to comprise the activity pattern of the *Or42a*>ChR2 OSN in response to both odor and light stimuli:

(1) rapid increases in neural activity triggered by abrupt positive changes in the stimulus intensity;
(2) a tendency of the neural activity to reach a plateau value when the stimulus does not accelerate;
(3) decreases in neural activity associated with strong stimulus decelerations;
(4) complete inhibition of the neural activity upon abrupt negative changes in stimulus intensity (e.g. exponential decrease).

Theses observations are further supported by the model predictions (Figures 41-45). This section will focus on taking the findings of the previous sections one level further: The neural activity will be used as the basis to model larval behavior during chemotaxis.

What features found in the neural activity of the OSN affects the control of run-to-turn transitions? A larval tracker capable of monitoring the position and behavioral state of a single larva in real-time at a rate of 30 Hz was built to tackle this question. Equipped with blue LEDs, the tracker was conceived to evoke predictable

patterns of neural activity in the *Or42a*>ChR2 OSN in freely behaving larvae (Figure 52). Unlike other tracking systems (Faumont, Rondeau et al. 2011), this setup was designed to keep the stage on which the larva evolves fixed by mounting the camera and stimulation LEDs on a moving stage whose position was continuously updated to stay locked with the animal's position (Figures 21 and 52).

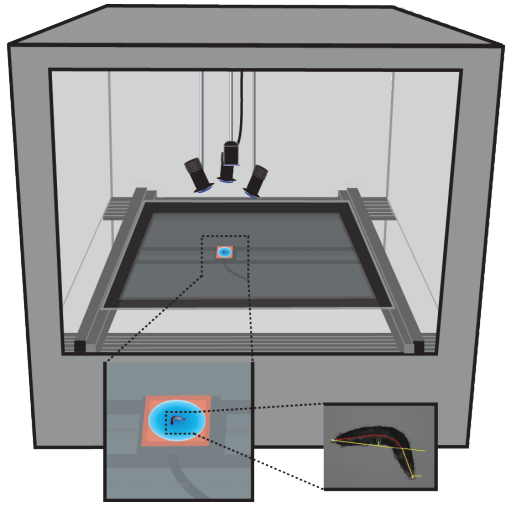

Figure 52. Schematic drawing of the closed-loop tracker. The blue LEDs and the camera are mounted on a moving stage that follows the larva while it crawls on an agarose slab (40x40 cm or approximately 120x120 body lengths of the larva).

Using empirical classifiers (Figure 22), the behavior of the larva was classified runs and non-runs on a frame-by-frame basis (state including head casts, turns and stops). Coupled with the physiological characterization of the *Or42a*>ChR2 OSN, the tracker allowed for the creation of virtual olfactory realities that were used to study the behavioral responses they produce. To avoid the innate

light avoidance behavior of larvae (Sawin-McCormack, Sokolowski et al. 1995; Kane, Gershow et al. 2013), experiments were conducted in blind larvae (see 'Materials and Methods section; Fly stocks'). Blind animals carried a genetically ablated, non-functional Bolwig's organ (*GMR*>hid) and a knocked out *TrpA1* gene (Xiang, Yuan et al. 2010). To make sure that blind larvae did not react to light stimuli, freely behaving blind larvae (*GMR*>hid;*TrpA1*[1]) were exposed to a series of pseudo-random light flashes, with a minimum inter-flash interval of 5 s. The behavior resulting from the flash was characterized by computing the flash-triggered averages of the amplitude of the absolute head angle and its time derivative. From Figure 53 it can be appreciated that, while WT animals (black) show a strong light response manifesting through an increase in head motion following the flash (release of head cast), blind *GMR*-hid;*dtrpA1*[1] larvae (red) were not affected by the light flashes. These findings are in agreement with controls reported by Gepner et al. who tested genetically blinded larvae (*GMR*-hid/+;UAS-CsChrimson/*Or42a*-Gal4) expressing CsChrimson in the *Or42a* OSN and found that they were unresponsive to blue light (Gepner, Skanata et al. 2015).

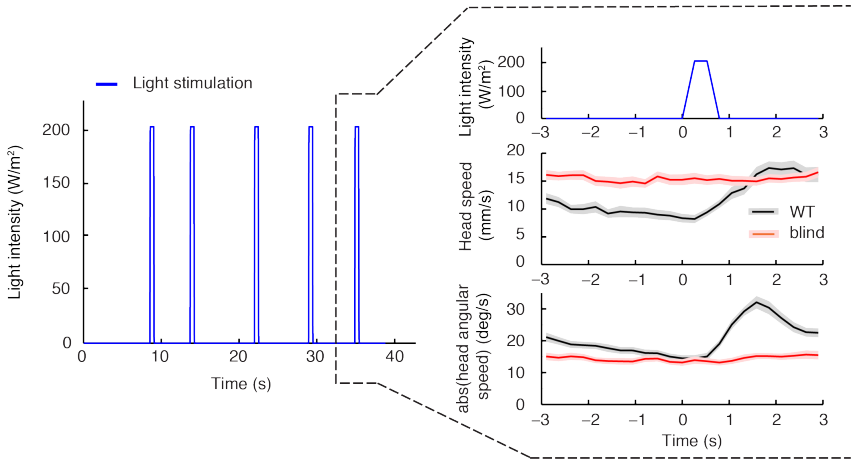

Figure 53. Abolishment of photophobic behavior in blind larvae. Stimulation of larvae with light flashes of 0.5 s (intensity: 207 W/m^2). Light flashes were interspaced by a time interval picked from a Poisson distribution with mean 7.7 s. The behavior resulting from the flash was characterized by computing the flash-triggered averages of the amplitude of the absolute head angle and its time derivative. Wild type larvae (black) display an increase in head motion following the flash (release of head cast). Blind *GMR*-hid;*dtrpA1*[1] larvae (red) were not affected by the light flashes. The graph represent the means of the kinematic variables computed across trajectories; the error bar denotes the SEM.

From stimulus to neural to behavior: Building a generalized linear model (GLM) to predict larval behavior

Building upon the ODE model developed for the OSN activity (Figure 40), the control of run-to-turn transitions was modeled by assuming a linear relationship. Matthieu Louis developed the behavioral model that is presented here in conjunction with Alex Gomez-Marin and Shaul Druckmann. Based on the observation that the turn probability remains the same when the OSN activity is constant (Figure 51) it was hypothesized, that the relationship between the OSN activity and run-to-turn transitions could be captured by a simple model where the time-varying probability of turning is described as a linear combination of a constant, a basal

turn rate term (λ_0) and a term proportional to the current OSN firing rate:

$$\lambda_0 + \lambda_1 * y(t)$$

Combined with a logit transformation to map the linear combination (which may be positive or negative) onto the definition domain of probability of turning, the turn probability was modeled by a generalized linear model (GLM) (Myers, Montgomery et al. 2002). In Figure 54, the integrated GLM model is outlined for the turn rate as a function of the predicted OSN activity. The model was trained on a set of light stimulation patterns identical to the linear and nonlinear ramps used to characterize the OSN response (Figures 58 and 59).

The predicted probability of turning was computed from a generalized linear model (GLM) based on a linear function of the firing rate of the OSN y.

This led to the following relationship:

$$\ln\left(\frac{\lambda(\mathrm{t})}{1-\lambda(\mathrm{t})}\right) = \gamma_0 + \gamma_1 \mathrm{y}(\mathrm{t}) \qquad (13)$$

The two parameters of the model, the basal turn rate γ_0 and γ_1, were computed from the open-loop experiments listed in Figures 58 and 59. The values of these parameters are reported in Table 5.

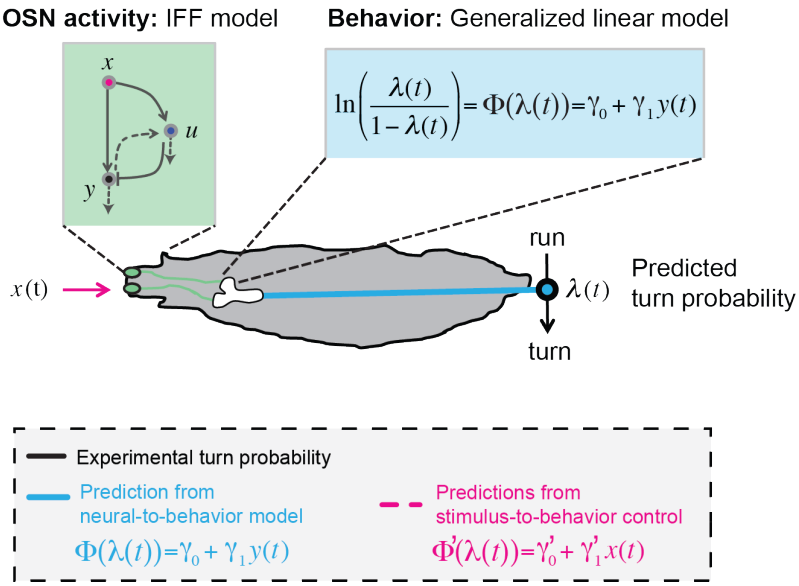

Figure 54. Quantitative model for the modulation of turn probability as a function of the sensory experience (integrate neural-to-behavior model). The turn probability is predicted from a linear combination of the predicted neural activity (g_1) and a constant basal turning rate (g_0). This linear combination is then fed into a Logit transformation to convert the domain of definition of the neural activity into probabilities ranging from 0 to 1. The two parameters of the model, g_0 and g_1, are determined from a linear regression on the experimental turning rate. The OSN activity driven by light, *y*, is predicted from the pure IFF model described in Figure 40. The raw stimulus intensity (not processed by the OSN) was used as the input into the control model. The parameters of this control model are denoted as g_0' and g_1'.

For each ramp, the results of the predicted turn rate are displayed in Figures 58 and 59 (cyan line). For the linear and nonlinear ramps, the GLM accurately reproduces the time course of the experimental turn probability (cyan line, Figures 58 - 59), indicating that the OSN firing rate was sufficient to predict the control of run-to-turn transitions. From a given firing rate of the OSN y, the turn rate was obtained as:

$$\lambda(t) = \frac{1}{1 + e^{-(\gamma_0+\gamma_1 y(t))}}$$

The goodness of fit of the model was evaluated by applying it to the closed-loop experiments described in Figures 60-67. The performance of the test model was compared to a control model where the turn probability was directly predicted from the stimulus intensity without any sensory processing achieved by the OSN (dashed magenta line, Figures 58 and 59).

For this control model, the same form of GLM was independently fitted with the firing rate replaced by the stimulus intensity. The values of the parameters of the test and control models are reported in Table 5. The goodness of fit of the GLM was found to be contingent on the nonlinear transformation achieved by the OSN (Table 6). However, for the majority of ramps, this improvement did not match the quality of the fit produced by the integrated neural-to-behavior model (Table 6), suggesting that circuits downstream from the OSNs are controlling run-to-turn transitions by processing the present OSN activity without substantial temporal integration. It appears that the turn probability alone is sufficient to predict the sensorimotor control resulting from the virtual reality paradigm.

For the probability of turning, two metrics were used to quantify the goodness of fit of the model. First, Pearson's correlation coefficient was used where the experimental observations were denoted as X_t and the output from the model as Y_t (Table 6 last column).

The final correlation coefficient was computed as:

$$r = \frac{\sum_{t=1}^{n}(X_t - \overline{X})(Y_t - \overline{Y})}{s_X\, s_Y}$$

where s_X is the standard deviation of variable *X* and n represents the total number of time points in the dataset.

The second metric represents the coefficient of variation of the root-mean-square error defined as:

$$\mathrm{CV(RMSE)} = \frac{\sqrt{\frac{1}{n}\sum_{t=1}^{n}(X_t - Y_t)^2}}{\overline{X}}$$

The integrated GLM predicts the time course of the experimental turn probability with good accuracy. The goodness of fit is greatly enhanced upon processing of the stimulus intensity by the OSN (IFF model for light-driven activity elicited in the *Or42a*>ChR2 OSN).

Three conclusions can be drawn from the successful application of the integrated GLM model of Figure 54:

(1) A stationary OSN activity leads to inherently stochastic transitions from run to turn. When the OSN activity remains constant, the probability of turning at a given time is largely independent of the time during which the larva has already been running;
(2) a high OSN firing rate induces strong suppression of turning (rising phase of the ramps);
(3) inhibition of the OSN activity induces strong facilitation of turning (most evident during the falling phase of the exponential ramp);

These results indicate that the nonlinear response characteristics of the OSN contribute to behavioral control in a significant way.

Challenging the GLM: Controls for closed-loop behavioral experiments

For the control model, the relationship (13) was:

$$\ln\left(\frac{\lambda(t)}{1-\lambda(t)}\right) = \gamma'_0 + \gamma'_1 x(t) \qquad (14)$$

where the parameters γ'_0 and γ'_1 were computed from a linear regression on the open-loop experiments listed in Figures 58 and 59.

Consistent with the findings that the OSN activity is sensitive to the slope of the ramp, it was found that the performance of the stimulus-to-behavior GLM was improved by combining the light intensity (*x*) with its first derivative (*dx*/*dt*) (Figure 55).

The contribution of the first derivative of the stimulus intensity was assessed in the following control model:

$$\ln\left(\frac{\lambda(t)}{1-\lambda(t)}\right) = \gamma''_0 + \gamma''_1 x(t) + \gamma''_2 \frac{dx}{dt}(t) \qquad (14)$$

The time derivative of the stimulus was defined by the change in stimulus intensity that occurred during the frame (33 ms) preceding the present time point *t*.

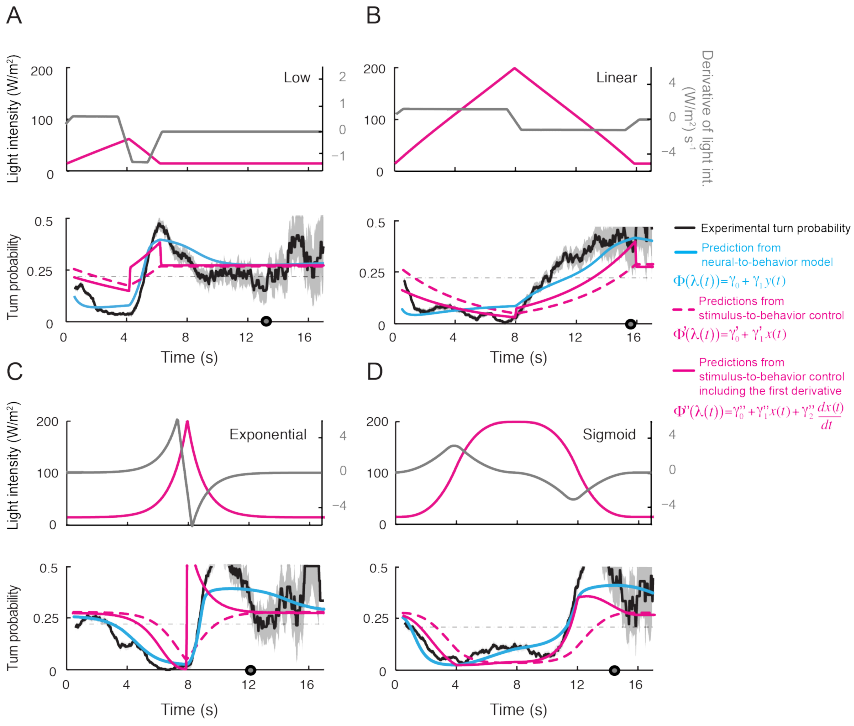

Figure 55. Comparison of the predictions of the stimulus-to-behavior controls with and without the first derivative of the stimulus for four representative light ramps (A-D). Time courses of the stimulus intensity (magenta, top) and its time derivative (gray, top). The turn probability estimated from the experimental data is shown in black (bottom). The prediction of the integrated neural-to-behavior model is shown in cyan (bottom). The performance of the stimulus-to-behavior control based on the stimulus intensity alone (dashed magenta line, bottom) improves by linearly combining the light intensity with its first derivative. It was noted that the stimulus-to-behavior control outperforms the neural-to-behavior model in all presented cases. The discrepancies between the controls and the test model are particularly pronounced during the beginning of the upward phase of the ramp. The goodness of fit is quantified in Table 6.

In closed-loop experiments conducted in light and odor gradients (Figures 61-71), the predictions of the GLM described in (13) were analyzed by computing the turn-triggered average of the turn probability. This average time course was compared to two controls. The first control consisted in achieving turn predictions based on a sensory experience whose relation to the corresponding behavior was uncoupled. The time course of the light (odor) intensity was inverted and associated with the forward time course of the behavior. This first control preserved the statistics of the stimulus intensity experienced by the larva. The second control was based on the assumption that the OSN firing rate was constant over time and corresponded to the mean activity predicted by a typical trajectory. Given that each larva experienced a different time course of light intensity, the mean OSN firing rate was computed on a trajectory-by-trajectory basis. The stimulus-based GLM derived in equation (14) for the open-loop light ramps (Figures 58 and 59) was deemed inadequate to predict closed-loop behaviors in odor gradients because of the mismatch between the dynamic range of the stimulus in the light ramps and in the odor gradient. The values of the parameters of both test and control models are reported in Table 5. The goodness of fit of the stimulus-based GLM and the two test models is reported in Table 6.

Table 5. Parameters of the GLM obtained upon optimization of model on the closed-loop behaviors listed in Figures 58 and 59. The first two columns of the table report the value of the stimulus-to-behavior control without (left) and with (center) the contribution of the first derivative of the stimulus. The last column reports the value of the integrated neural-to-behavior model fed with the predicted firing rate of the OSN.

	Control without 1st derivative of stimulus	Control with 1st derivative of stimulus	Test model with predicted neural activity
γ_0 (constant)	-0.8156	-0.8200	-0.3534
γ_1 (input variable)	-0.0114	-0.0013	-0.1523
γ_2 (derivative of input variable)	0	-0.0214	0

Table 6 Quantification of the goodness of fit of the control and test GLM against the experimental data.

(A) Comparison between the integrated neural-to-behavior and stimulus-to-behavior GLMs and the experimental estimate of the turn probability through the application of Pearson's correlation coefficient on the time course of the experimental turn probability and the predicted turn probability.

(B) Comparison between the integrated neural-to-behavior and stimulus-to-behavior GLMs and the experimental estimate of the turn probability through the coefficient of variation of the RMSE on the time course of the experimental turn probability and the predicted turn probability. The quantification was restricted to the first 12 s of the ramp where the experimental estimate of the turn probability is reliable. The goodness of fit was computed over the entire duration of the ramp across conditions and is reported at the bottom of the table for both metrics.

A

Correlation coefficient	Control without derivative	Control with derivative	Test model
Linear (4s), low	0.69	0.75	0.89
Linear (4s), med	0.62	0.90	0.90
Linear (4s), high	0.67	0.96	0.95
Linear (4s), slow	0.54	0.92	0.91
Linear (4s), fast	0.65	0.76	0.90
Linear (8s)	-0.05	0.66	0.78
Quadratic	0.11	0.70	0.88
Exponential	0.29	0.43	0.92
Sigmoid	0.13	0.61	0.60
Asymptotic	-0.10	0.25	0.03
All conditions (all time points included)	*0.53*	*0.74*	*0.86*

B

CV(RMSE)	Control without derivative	Control with derivative	Test model
Linear (4s), low	0.59	0.54	0.33
Linear (4s), med	0.60	0.41	0.32
Linear (4s), high	0.75	0.41	0.33
Linear (4s), slow	0.56	0.34	0.27
Linear (4s), fast	0.53	0.45	0.31
Linear (8s)	1.06	0.71	0.59
Quadratic	1.06	0.73	0.55
Exponential	0.84	0.85	0.39
Sigmoid	0.95	0.65	0.58
Asymptotic	0.85	0.52	0.97
All conditions (all time points included)	*0.65*	*0.51*	*0.39*

Triggering behavioral transitions: Optogenetic stimulation in open-loop conditions

Taking advantage of the tracker's ability to produce stereotyped light ramps, reproducible patterns of neural activity were elicited in the *Or42a*>ChR2 OSN (Figures 41-43, bottom). In a first series of optogenetic behavioral experiments an open-loop paradigm was used to associate each run with a light ramp. For example, the onset of each run was associated with either an exponential ramp (test condition) or constant basal light intensity (control).

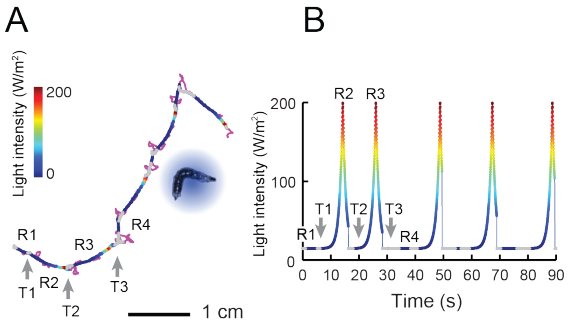

Figure 56. (A) Presentation of the run-locked light stimulation paradigm where runs are randomly assigned to constant stimulation (control) or to a test ramp with an exponential profile similar to that introduced in Figure 43.

(B) Midpoint position of the larva during a trajectory with the light intensity color-coded according to the colorbar on the left. Illustrative runs denoted as R1-4 are interspaced by turns T1-3 denoted by arrows.

For successive runs, the two stimulation conditions — ramp and constant stimulation — were picked at random. This approach allowed for the correlation of the predicted OSN firing rate with the control of run-to-turn transitions.

When an exponential ramp was played to the larva, the pattern of light stimulation was maintained exclusively for the duration of a run state. It was eventually interrupted as soon as the larva initiated a turning maneuver, an event triggering the immediate reset of the light intensity back to basal levels. As the motion of the larva had no influence on the stimulation pattern it experienced during a run, this experimental protocol features a sensorimotor loop that is essentially open. The alternation between the ramps and constant stimulation is illustrated in Figure 56 where runs R1 and R4 are associated with basal stimulation and runs R2 and R3 are associated with the exponential ramp. The majority of the runs associated with an exponential ramp did not terminate before the falling phase of the ramp. This trend was quantified through the turn probability, which was defined as the relative number of runs that switched to a turn during a sliding time window of 1 s. Upon constant light stimulation, the turn probability was largely independent of the duration of the ongoing run (light gray line, Figure 57). In contrast, the turn probability was strongly modulated by the exponential light ramp. During the rising phase of the ramp (0-8 s), turning was strongly inhibited: the turn rate dropped below the value corresponding to basal stimulation (light gray line). During the 2 s that precede the end of the rising phase (6-8 s), the turn rate almost approaches values close to 0. Conversely, a sharp increase in turning was observed during the falling phase of the ramp (black line, Figure 57). The estimation of the turn probability remained accurate until the number of remaining runs became too small. The dot on the x-axis indicates the time point where fewer than 10% of the initial runs are left.

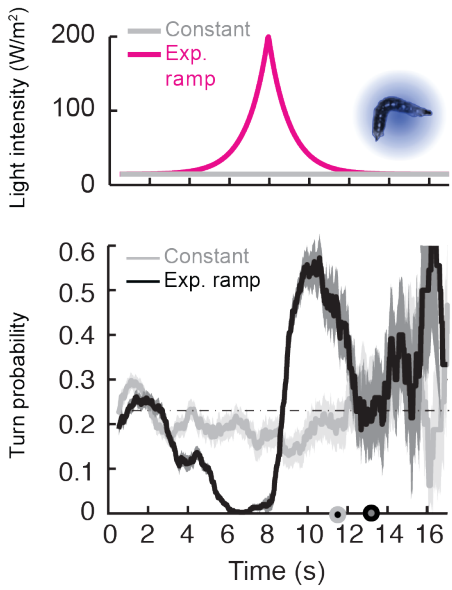

Figure 57. Turn probability estimated from an experimental set of trajectories upon constant stimulation (light gray) and stimulation by an exponential light ramp (black). The turn probabilities are reported as the fraction of turns occurring during a 1-s window centered on the time point of interest. Error bars are estimated by resampling the initial distribution 100 times without replacement and with a sample containing half of the original set (error bars represent standard deviations). The dashed line depicts the mean turning rate computed for the constant stimulation condition. It can be seen that the turning rate is largely independent of the run duration. The small disks on the x-axis indicates the time point after which fewer than 10% of the total number of runs are left for the constant stimulation (light gray) and exponential ramp (dark gray). Beyond these time points, the estimate of the turn probability becomes unreliable.

Beyond this indicative value, a large fluctuation in the turn rate was observed due to the low number of long-lasting runs available for analysis. The modulation of the turn probability by the light evoked neural activity supported the idea that a strong activation of the OSN efficiently suppresses turning whereas inhibition of the neural activity promotes turning. These results indicate that certain behavioral transitions are indeed strongly dependent on context specific modulations of the OSN activity.

To explore the modulation of the turn probability by the OSN activity in greater depth, larvae were exposed to different light stimulation protocols in open-loop conditions (stimulation exclusively during a run-mode). The behavioral experiments were designed to employ the same linear and non-linear functions that had been used to characterize the OSN response dynamics by means of electrophysiology (Figures 41-43). When exposed to a linear increase in light intensity the turn probability is suppressed whenever the OSN firing increases (Figure 58). The suppression seems to be slightly slope dependent: the steeper the increase, the stronger the suppression of turning. A strong facilitation of turning (turn probability highest) is triggered whenever the OSN firing rate drops significantly. This drop in neural activity coincides with a transition of the stimulus from a linear increase to a linear decrease in light intensity (Figure 58).

The results obtained in animals exposed to non-linear light ramps in open-loop conditions highlight the importance of the OSN activity in controlling the turn probability (Figure 59). In the case of the sigmoid stimulation protocol, the turn probability is slightly elevated during a time where the stimulus reaches its maximum light intensity.

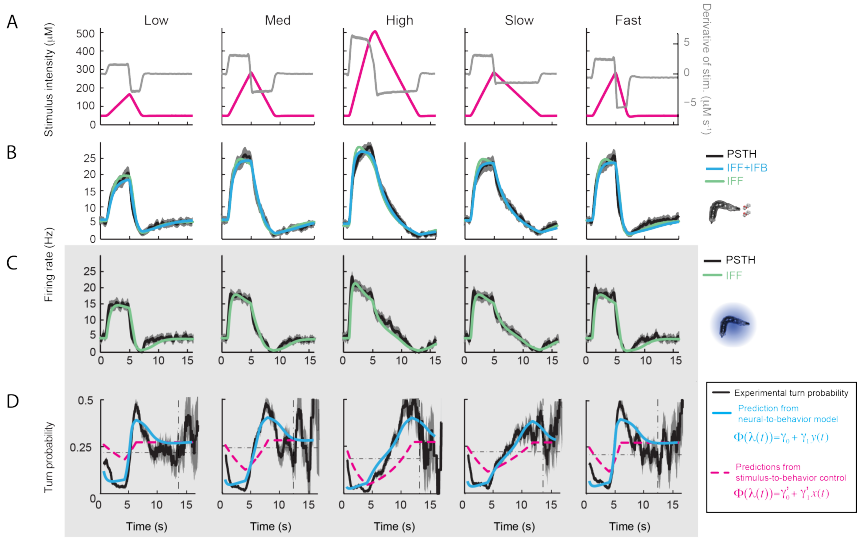

Figure 58. Fit of the stimulus-to-neural (ODE) model and predictions of the integrated neural-to-behavior model for the linear ramps.

(A) Stimulus intensity given as odor concentration (uM, magenta). The same (idealized) profile was used for the light stimulation with an intensity ranging between 15 W/m² and 207 W/m². Fit of the solution of the ODE model for the linear stimulation ramps generated with odor and light. Upon mild smoothening of the stimulus time course trajectories with a Savitzky-Golay filter, the time derivative (gray) of the concentration profile is represented according to the ordinate on the right of the graph.

(B) Modeling of the OSN activity elicited by odor ramps. Comparison of the experimental PSTH (black) with the outcome of the model featuring a pure IFF motif (green) and a combination of the IFF and IFB motifs (cyan).

(C) Same as B for the light ramps. Comparison of the experimental PSTH with the outcome of the model based on a pure IFF motif (green). For all conditions shown in this figure, the PSTHs were computed on a pool of minimum 10 recordings conducted on minimum 10 preparations.

(D) Application of the stimulus-to-behavior integrated model to predict behavior to stereotyped light ramps (model introduced in Figure 54). The test model (cyan) is based on the neural activity modeled by the IFF motif (green, panel C). As indicated in the textbox on the right, the control model is purely based on the stimulus (dashed red). The black dashed line in the background represents the average turn probability observed upon stimulation at constant intensity. The integrated stimulus-to-behavior model clearly outperforms the predictions of the control model. For all test conditions, the experimental turn probability was estimated on a sample of 490 to 970 runs.

This counter intuitive observation, however, starts to make sense when the actual neural firing rate is considered: the OSN activity starts to drop as soon as the rising stimulus passes its turning point where the 2nd derivative (acceleration) of the stimulus time course starts to turn negative (compare to 'Results section; Non-linearly evolving stimuli: changing both speed and acceleration). Also in the case of the non-linear ramps it can be seen that turn facilitation is strongest when the drop in OSN activity is strongest (as is the case after the exponential light stimulation in Figure 59). Conversely, over periods of mild decreases in neural activity, the turn probability raises only mildly (as can be seen for the asymptotic stimulation in Figure 59).

Is a linearly dissected version of a non-linear ramp able to reproduce behavioral results similar to the ones obtained for non-linear ramps? A linear piecewise approximation of an exponential, an asymptotic and a combination of the two stimulation protocols were tested in larvae behaving in open-loop conditions as outlined above. While the behavior elicited by an asymptotic stimulation is well recapitulated by its piecewise linear approximated version (Figure 60), in the case of the piecewise exponential the behavior is slightly different from the actual exponential. Turning is temporarily suppressed in response to each boost of neural activity triggered at each stimulus' positive inflection point (0 s and 4 s into the stimulation) (Figure 60). Overall, discrete features of the piecewise linear approximations are translated into measurable behavior.

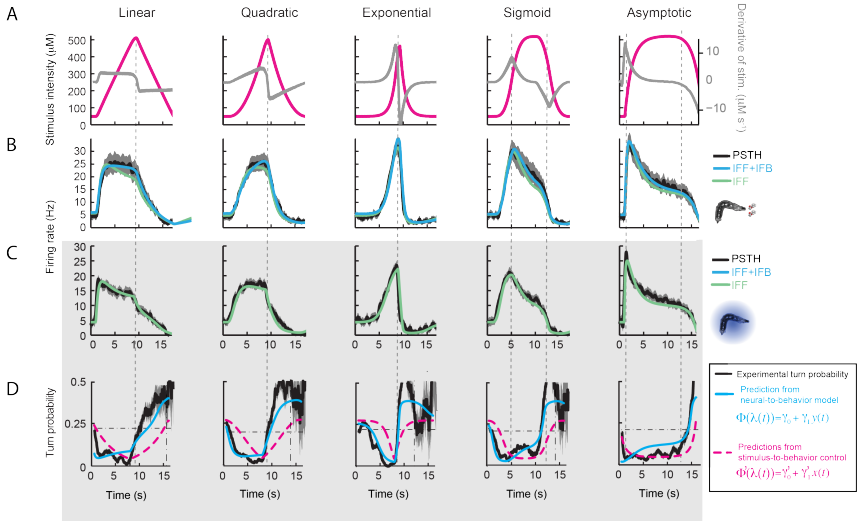

Figure 59. Fit of the stimulus-to-neural (ODE) model and predictions of the integrated neural-to-behavior model for nonlinear ramps.

(A) Stimulus intensity given as odor concentration (uM, magenta). The same (idealized) profile was used for the light stimulation with an intensity ranging between 15 W/m² and 207 W/m². Fit of the solution of the ODE model for the nonlinear stimulation ramps generated with odor and light. Upon mild smoothening of the stimulus time course with a Savitzky-Golay filter, the time derivative (gray) of the concentration profile is represented according to the ordinate on the right of the graph.

(B) Modeling of the OSN activity elicited by odor ramps. Comparison of the experimental PSTH (black) with the outcome of the model featuring a pure IFF motif (green) and a combination of the IFF and IFB motifs (cyan).

(C) Same as B for the light ramps. Comparison of the experimental PSTH with the outcome of the model based on a pure IFF motif (green). For all conditions shown in this figure, the PSTHs were computed on a pool of minimum 10 recordings conducted on minimum 10 preparations.

(D) Application of the stimulus-to-behavior integrated model to predict behavior to stereotyped light ramps (model introduced in Figure 54). As indicated in the textbox on the right, the test model (cyan) is based on the neural activity modeled by the IFF motif (green, panel C). The control model is purely based on the stimulus (dashed red). The dashed horizontal line in the background represents the average turn probability observed upon stimulation at constant intensity. Dashed vertical lines indicate time points associated with abrupt changes in the first derivative of the stimulus. The integrated stimulus-to-behavior model clearly outperforms the predictions of the control model. Experimental turn probabilities estimated on samples of 490 to 970 runs.

It is noteworthy that the different stimulus segments specific to the piecewise linear dissected ramps transitioned very abruptly, a fact rendering this kind of stimulation impossible when using real odors. The stimulation was therefore solely conducted with light.

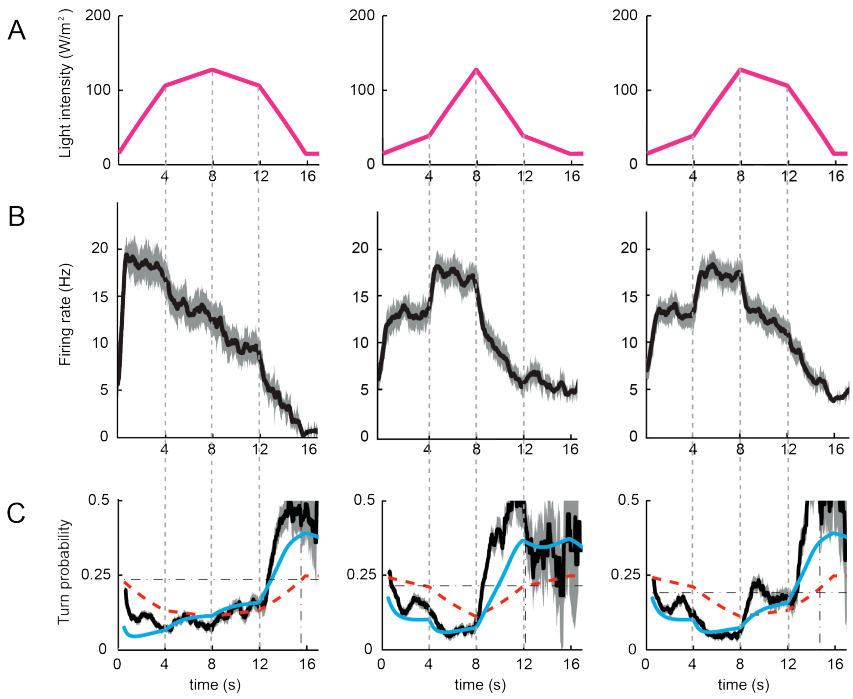

Figure 60. Predictions of the integrated neural-to-behavior model for the linear piecewise approximated ramps.

(A) Stimulus intensity given as light intensity (15 W/m², magenta).

(B) Experimental PSTHs (black) were computed on a pool of minimum 10 recordings conducted on minimum 10 preparations.

(C) Application of the stimulus-to-behavior integrated model to predict behavior to stereotyped light ramps (model introduced in Figure 54). The test model (cyan) is based on the neural activity. As indicated in the textbox on the right, the control model is purely based on the stimulus (dashed red). The black dashed line in the background represents the average turn probability observed upon stimulation at constant intensity. The integrated stimulus-to-behavior model clearly outperforms the predictions of the control model. For all test conditions, the experimental turn probability was estimated on a sample of 490 to 970 runs.

Validating the GLM: Studying unconstrained behavior in simple virtual olfactory gradients (closed-loop)

Is the GLM model able to make accurate behavioral predictions in conditions of unconstrained larval behavior in simple virtual light gradients?

The control of run-to-turn transitions is inherently stochastic in nature. Therefore, the predictive power of the integrated neural-to-behavior model (Figure 54) needed to be tested by experiments involving animals behaving in virtual olfactory gradients in conditions where the sensorimotor loop was closed (closed-loop).

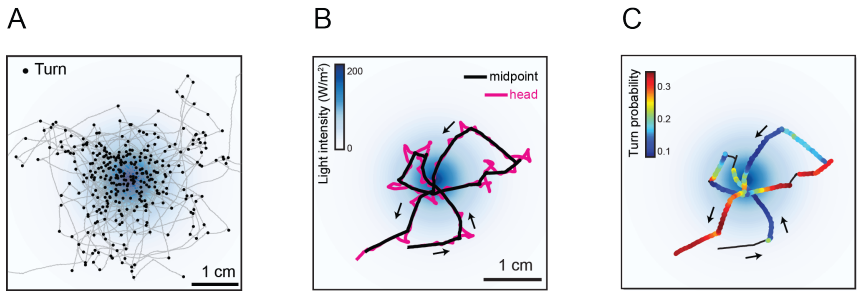

Figure 61. Synthetic chemotaxis in a virtual odor gradient produced by light stimulation. The larva experiences a light intensity determined by a predefined stimulus landscape. The landscape displayed in the background is an exponential gradient centered on a point 'source'.

(A) Overlay of 10 trajectories recorded in the exponential light gradient. Turns are indicated as small black circles. Larvae evolving in this light gradient accumulate at the peak of the gradient as observed for odor gradients.

(B) Illustrative trajectory of the midpoint (black) and head (magenta). Black arrows indicate the direction of motion.

(C) Overlay of the trajectory of the midpoint with the predicted instantaneous turning rate color-coded according to the colorbar on the left. The turn probability tends to increase (red color range) when the larva is moving away from the gradient's peak whereas it decreases (blue color range) when the larva is moving towards the peak.

In this paradigm, a light gradient with a fixed geometry comparable to the odor gradient was used (Figure 61). In this virtual environment a larva experienced a light intensity defined by the position of its head according to a predefined virtual light landscape.

Unlike in the open-loop paradigm, the light stimulation was continuously modulated by the larval behavior. Figure 61B illustrates the trajectory of an *Or42a*>ChR2 larva in the exponential light gradient. In a way similar to the odor-driven behavior (Figure 29, panels A and B) (Gomez-Marin, Stephens et al. 2011), the larva ascends the light gradient, overshoots the gradient's peak, implements a sharp turn and returns to the gradient's peak — a behavior termed 'circling'. Figure 62B explores how the *Or42a*>ChR2 OSN responds to the light time course reconstructed from an animal's behavior in a virtual exponential gradient.

The experimental PSTH obtained from the electrophysiological recording is reported in the middle panel (black trace) and well recapitulated by the predictions of the IFF model (green trace). The neural activity was subsequently fed into the GLM model to predict the turn probability associated with individual runs (Figure 62C, cyan line). In Figure 61C the resulting turn probability is shown color-coded on top of the trajectory of the midpoint. As a general trend, the termination of a run is preceded by an increase in the predicted probability of turning.

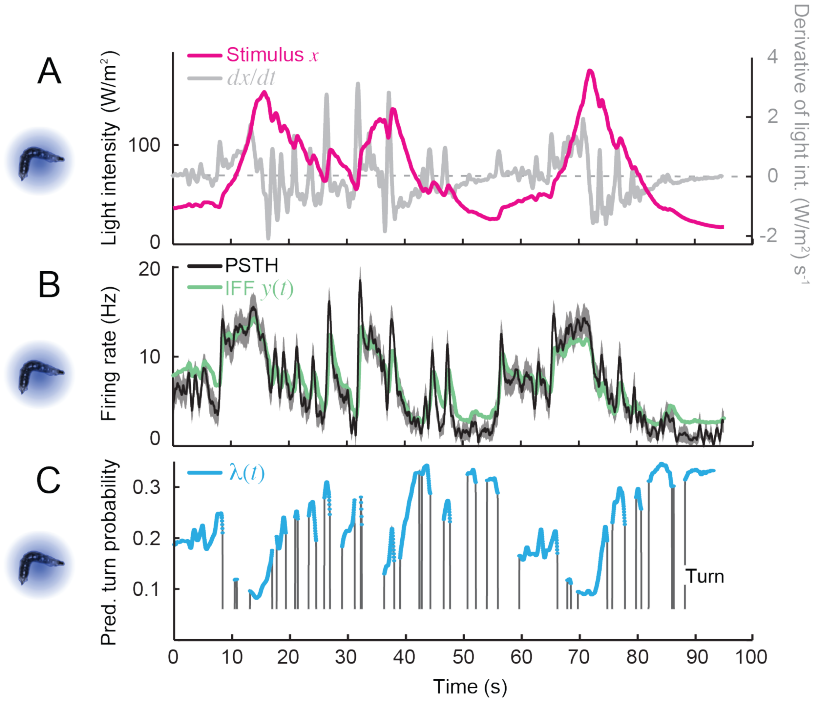

Figure 62. (A) Time course of the light intensity associated with the trajectory displayed in Figure 61 (panels B and C). To compare to data obtained in a real odor gradient see Figure 71.

(B) PSTH of the OSN activity measured experimentally upon a replay of the intensity time course at the electrophysiology rig (black). Neural activity predicted by the model based on the IFF motif (green) presented in Figure 40.

(C) Turn probability (cyan) predicted from the integrated neural-to-behavior model presented in Figure 54. The predicted turn probability is only shown for the behavioral sequences associated with runs.

When comparing behavior elicited by a linear and by an exponential ramp in open-loop conditions, it appears that the behavior elicited by a linear gradient is different from that generated by an exponential gradient: in the exponential gradient (Figure 57), run-to-turn transitions are more stereotypic and more precise than in the linear gradient (Figure 58). This comes as a result of an increased suppression of turning when moving down gradient while

experiencing a more drastic decrease of stimulus intensity. To test this prediction, closed-loop experiments with freely moving animals were carried out in virtual light gradients with an exponential and a linear geometry (Figure 63).

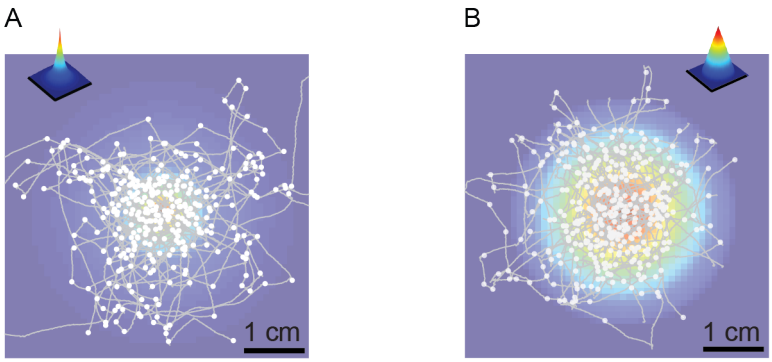

Figure 63. (A) Overlay of 10 consecutive trajectories recorded in the exponential light gradient shown in panel A. Each trajectory corresponds to a different larva. Turns are indicated as small circles. Scale bar represents 1 cm.

(B) Overlay of 10 consecutive trajectories recorded for a linear light gradient with the same peak value as the exponential gradient shown in panel A.

In both light gradients, larvae accumulated around the gradient's peak. However, as expected, the spread of the trajectories with respect to the peak was larger for the linear light gradient (Figure 64A). With regards to the duration of runs, no noticeable increase was found between the two gradients (Figure 64B).

Next, by focusing on runs lasting longer than the mean (cutoff: 4 s), the average stimulus input (turn-triggered average) and the corresponding predicted OSN activity preceding a turn was computed (Figure 65).

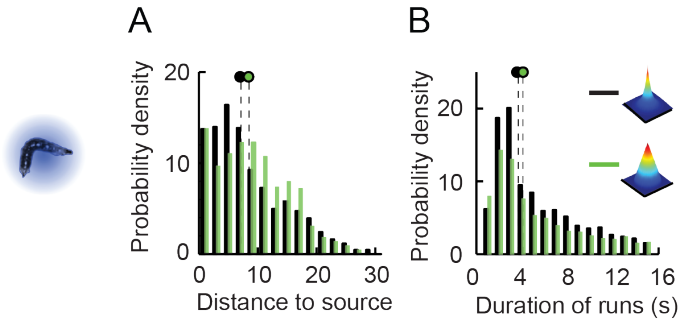

Figure 64. Radial distribution of distances to the source and the run durations during closed-loop behavioral experiments in two virtual light landscapes (exponential and linear). Larvae tend to accumulate more closely to the peak of the exponential gradient, even though the average run duration is the same in both light gradients. Distribution computed on runs with a minimal duration of 1s.

(A) Comparison of the distribution of distances to the source (peak intensity) between the run set obtained for the exponential light gradient (black) and the linear light gradient (green). The circles indicate the median distance (median distance for the exponential light gradient: 7.7 mm).

(B) Comparison of the distributions of the run durations between the run set obtained for the exponential light gradient (black) and the linear light gradient (green). The circles indicate the median run duration (median rund duration for the exponential light gradient: 3.8 s).

For both the linear and exponential gradients, it was found that the average stimulus intensity decreases monotonically for several seconds before a turn is implemented (Figure 65 panels A and B). The rate of stimulus decrease, however, is slightly larger for the exponential gradient than the linear gradient. In the case of the exponential gradient, the stimulus deceleration prior to turning is more prominent. As a result, the predicted OSN activity, although showing a monotonic decrease for both conditions, is more strongly suppressed for the exponential gradient (Figure 65 panels A and B).

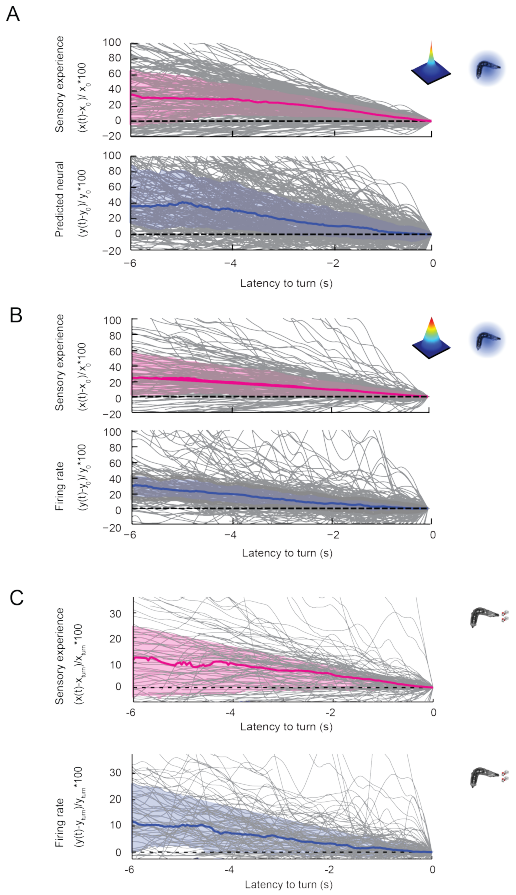

Figure 65. (A) Turn-triggered average of the sensory experience (top, magenta) and predicted OSN activity (bottom, blue) for the runs observed in the exponential light gradient. Shown is the relative change in stimulus intensity or firing rate upon normalization by the value observed at the end of the run (x_0 or y_0). Analysis restricted to the set of runs lasting longer than 1 s.

(B) Same as A for the runs observed in the linear light gradient.

(C) Turn-triggered average of the sensory experience (top, magenta) and the predicted OSN activity (bottom, blue) for the runs observed in the odor gradient. Shown is the relative change in stimulus intensity or firing rate upon normalization by the value observed at the end of the run (x_0 or y_0). Analysis restricted to the set of runs lasting longer than 1 s.

In all three cases both the stimulus intensity and neural intensity decreases prior to the initiation of a turn. However, the amplitude of the decrease is reduced by a factor two when comparing the turn-triggered average observed in the odor gradient to the turn-triggered average of the light gradients.

The turn-triggered average of the predicted turn rate suggested a similar conclusion: prior to a turn, the probability of turning increases steadily over the course of several seconds. This increase tends to be shorter and slightly steeper for the exponential gradient, which might explain why larvae are able to pinpoint the gradient's peak more accurately in the exponential landscape (Figures 63, 64, and 66).

For both light landscapes, the modulation of the predicted turn probability was compared to two controls:

(1) behavioral predictions based on the assumption that the OSN spiking activity remained constant (use of average firing rate predicted on a trajectory-by-trajectory basis) and
(2) behavioral predictions upon uncoupling of the stimulus and the behavior by inverting the reconstructed temporal evolution of the stimulus.

In contrast to the test model, neither control displayed substantial increases in turn probability prior to turning (Figure 66). From the results in this section it can be seen that the integrated neural-to-behavior model built on controlled conditions of stimulation (open-loop paradigm) was sufficient to predict run-to-turn transitions arising from free behavior in a virtual odor gradient (closed-loop paradigm).

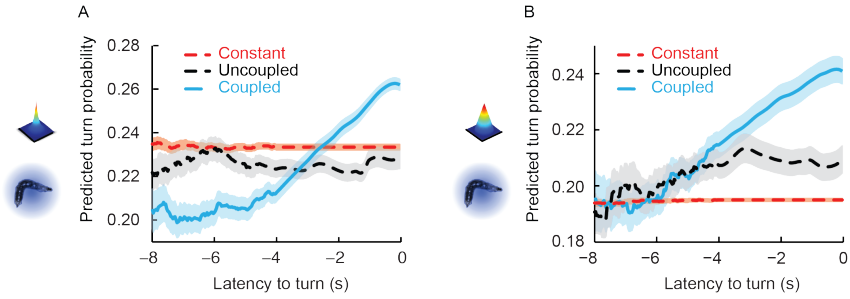

Figure 66. Predicted turn probability in different light landscapes.

(A) Turn-triggered average of the predicted turning rate for the exponential light gradient. A comparison is made between the predictions based on the OSN activity driven by the real stimulus intensity (cyan), predictions using the OSN activity driven by the time-reversed stimulus time course (uncoupled control, black) and predictions based on the assumption that the neural activity stays constant over the course of each trajectory (constant control, red). The stimulus-to-behavior model was trained on the experiments described in Figures 58 and 59. Analysis restricted to the set of runs lasting between 4s and 10s. It was observed that the predicted turning rate steeply increases 4 s before the turn, highlighting the stereotypy in the sensorimotor control of run-to-turn transitions.

(B) Same as A for the linear light gradient. It was observed that the predicted turning rate increases more steadily prior to the turn, which is due to the shallower change in sensory experience associated with movements in the linear landscape.

Validating the GLM: Studying unconstrained behavior in complex virtual olfactory gradients (closed-loop)

Through behavioral experiments in open-loop conditions (Figures 58 and 59) it was demonstrated that inhibition of OSN activity facilitates turning whereas sustained high levels of OSN activity suppresses turning. In addition, it was shown that larvae are able to navigate simple virtual light gradients through a behavior reminiscent to chemotaxis (Figures 61-66).

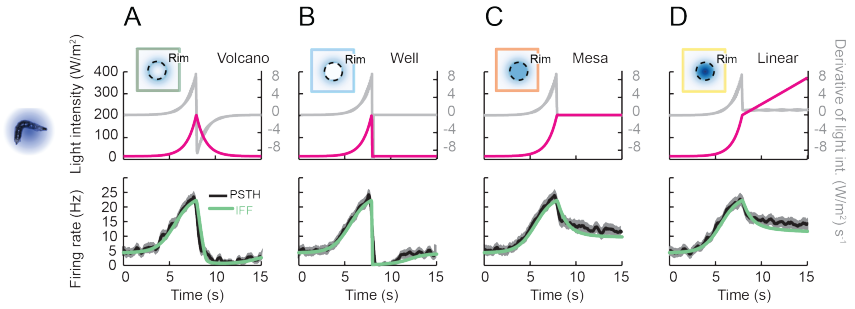

Figure 67. Experimental and predicted OSN activity elicited by 4 stimulus time courses starting with a common 8s exponential increase (stimulus shown in magenta; first derivative of the stimulus shown in gray).

(A) The stimulus ramp ends with a symmetrical exponential decrease ('volcano').

(B) The stimulus ramp ends with an abrupt drop to baseline intensity ('well'). A strong inhibition of neural activity is observed upon the instantaneous decrease of intensity to baseline level.

(C) The stimulus ramp ends with a maintenance of the maximum intensity ('mesa'). The transition from an exponential increase in the stimulus intensity to a constant intensity leads to a transient decrease in neural activity before a steady state value is reached.

(D) The stimulus ramp ends with a linear increase ('linear'). The switch of an exponential increase to a linear increase of the stimulus intensity leads to a transient decrease in neural activity similar to the one observed for the 'mesa' (panel C).

How do changes of the OSN activity — OSN activity elicited by rapid transitions of the stimulus — modulate unconstrained behavior in more complex virtual light gradients?

Four radially symmetrical light landscapes were designed with characteristics challenging the GLM's predictions (Figures 67 and 68). The geometrical properties of the gradients were chosen to facilitate behavior with predictable modulations of run-to-turn transitions. All cases feature an exponential increase at the rim of the landscape that is transitioned into a different kind of stimulation at the center specific for each case.

(1) First, a landscape with an exponential rise interrupted 8 mm from a center point was considered. At this distance, the exponential rise was transformed into an exponential fall. The shape of this landscape is reminiscent of a 'volcano' (Figures 67A and 68Ai). Given that the average speed of a larva is 1 mm/s, the geometry of the landscape was chosen in such a way that a larva starting at 16 mm from the center and moving towards the center should experience the stimulus time course depicted in Figure 67A (volcano, magenta line). The corresponding OSN activity and model's prediction are presented below the stimulus time course (Figure 67A, black and green lines). The turning probability was expected to be lower during the rising phase of the gradient while it was expected to be higher whenever the stimulus fell. Trajectories were therefore expected to produce back-and-forth meandering along the rim of the volcano. As a result, the central area would be avoided.

(2) The second case consisted of an extreme version of the volcano comprising an extreme drop in intensity in the central area of the landscape (well). A larva moving from the periphery of the landscape towards the center would experience an exponential rise in light intensity followed by a sudden drop of stimulus intensity to a basal value. This stimulus time course is depicted in Figure 67B. In response to the abrupt transition from the rising to falling phase the OSN features a vigorous suppression of the neural activity (Figure 67B, black and green lines). The corresponding behavior was expected to be associated with a nearly deterministic release of turns as soon as the larva experienced a drop in intensity associated with the central area (crater) of the landscape. As a result, larvae were predicted to avoid the central area even more aggressively than for the volcano.

(3) The third landscape was complementary to the well: a plateau (or mesa) where the maximum light intensity reached at the rim was maintained up to the center (Figure 67C). A larva starting at a distance from the center would experience an exponential rise followed by a constant intensity. This pattern of stimulus intensity creates a rising phase followed by a small drop in neural activity before the firing rates plateaus until the end of the ramp. The IFF model accurately predicts the OSN activity (Figure 67C, black and green lines). The effect expected on the behavior was a moderate

increase in turning for inward runs that passed the rim, but no significant avoidance of the central area of the plateau (mesa).

(4) The fourth landscape featured a linear hat (cone) at its center. A run moving towards the center would be associated with an exponential rise in stimulus intensity followed by a linear increase (Figure 67D, magenta trace). In a counterintuitive way, this stimulation pattern was not expected to lead to a monotonically increasing OSN activity: the firing rate drops at the transition from an exponential increase to the linear increase — a phenomenon well recapitulated by the IFF model (Figure 67D, black and green lines). This decrease is due to a deceleration in the stimulus intensity in spite of the monotonic increase of the stimulus intensity.

A run associated with this stimulation pattern is expected to produce a behavior similar to that of the plateau (mesa) landscape.

The behavioral predictions from the qualitative model were verified by the experimental observations. For the volcano landscape, *Or42a*>ChR2 larvae meander around the rim (Figure 68Ai, middle). Inward runs are interrupted quickly when the larva reaches out beyond the rim. This point is illustrated by restricting the representation to the set of inward runs that start outside the central area of the landscape (Figure 68Ai, right). In Figure 68Aii, the stimulus time course, the predicted OSN activity and the turn rate are represented for a representative run.

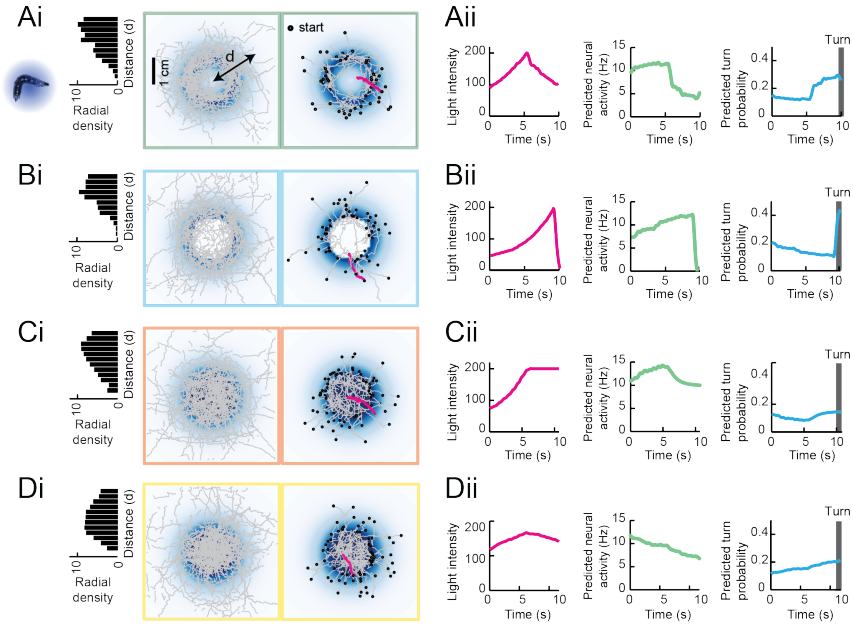

Figure 68. (Ai) Symmetrical two-dimensional light landscapes corresponding to the exponential 'volcano' profile. (Left) 15 trajectories superimposed onto the stimulus landscape. (Top-Left) Radial density distribution of all positions with respect to the center of the landscape (origin of axis). (Right) Set of 48 runs starting from the external edge of the 'volcano' and heading towards its center.

(Aii) Sensorimotor properties of the illustrative run depicted in magenta in panel Ai. (Left) Stimulus intensity time course: the peak of the rim is reached after approximately 5 s and it is followed by a decrease in stimulus intensity. (Center) Predicted neural activity: the OSN activity is expected to drop significantly after the landscape's rim has been passed. (Right) Predicted turn probability from the stimulus-to-behavior model. The probability of turning significantly increases when the larva is moving down-the-gradient and a turn follows approximately 4 s after the crossing of the rim.

(Bi) Same as Ai for the 'well' profile. For this landscape, it was observed that the crossing of the rim leads to an aversive response. Consequently, larvae avoid the well at the center of the landscape. 63 runs are shown in the right plot.

(Bii) Same as Aii. When the larva passes the rim, the light intensity drops to baseline and the OSN activity becomes inhibited. As a consequence the turning rate is predicted to spike steeply: within 1 s after the crossing of the rim, a turn is implemented.

(Ci) Same as Ai for the 'mesa' profile. For this landscape, it was observed that the crossing of the rim does not lead to an aversive response: larvae tend to maintain their ongoing run. The center of the landscape is therefore visited. 79 runs are shown in the right plot.

(Cii) Same as Aii. When the larva passes the rim, the neural activity decreases slightly as expected from the electrophysiological response in panel A. This decrease in neural activity leads to a moderate rise in turn probability, which triggers a turn approximately 4 s after the crossing of the rim.

(Di) Same as Ai for the 'linear' increase profile. For this landscape, the rate of change in the stimulus decreases when the larva crosses the landscape's rim whereas the stimulus intensity keeps increasing up to the peak of the gradient.

(Dii) Same as Aii. In agreement with panel A, the switch from an exponential to a linear increase in the stimulus leads to a moderate decrease in neural activity for the first 4 s of the run in spite of the positive light gradient experienced by the larva. This decrease becomes moderately amplified when the larva passes the peak of the landscape. Throughout the run, the turning is predicted to monotonically increase from a low starting value. As for the 'mesa', the central area the landscape is visited by larvae. 72 runs are shown in the bottom plot.

The steady increase in turn probability lasts several seconds before the run terminates. In contrast to the volcano, the well creates an even stronger repulsion for the central area that results in an exclusion zone (Figure 68Bi, middle). The predicted turn probability of the representative run shown in Figure 68Bii accounts for the nearly instantaneous release of turning when the rim is crossed. This observation is contrasted by the plateau (mesa) landscape, where the central area does not trigger any aversive behavior: upon crossing of the rim, runs do not sharply terminate; instead, the central area is widely occupied (Figure 68Ci, middle). Yet, the predicted turn probability of a representative run illustrates the modest increase in turning rate that results from the crossing of the rim (Figure 68Cii). This observation supports the notion that even a slight decrease of the OSN activity leads to a measurable increase of the turn probability. The landscape featuring a central linear hat (cone) produces a behavioral pattern reminiscent of the one elicited by the plateau (mesa) (Figure 67Di, middle). In spite of the continuously rising stimulus intensity experienced by an animal that crosses the

rim, only a moderate increase in turning is expected (first 5 seconds of illustrative run shown in Figure 68Dii). These results are also compatible with the notion that the OSN functions as a slope detector that is sensitive to the derivative of the stimulus intensity (speed).

To strengthen the previous observations, the average duration of runs directed towards the center after crossing of the rim was quantified for each landscape. This average was predicted to capture the efficiency with which turns were elicited by stereotyped changes in stimulus intensity experienced at the rim. As shown in Figure 69B, the run duration is shortest for the well landscape (average turn latency: 0.93 s) where a near-deterministic interruption of ongoing runs upon crossing of the rim was observed. Also the volcano featured a relatively short run duration (average latency: 3.48 s). Differences between the medians of the run duration were tested by applying on a Wilcoxon test with a Bonferroni correction to maintain the confidence level higher than 99%. The difference in the average latencies to turning of the well and volcano is significant. Also, the duration of the runs observed for the plateau (mesa) and linear hat (cone) is significantly larger than the well (average turn latency of mesa and linear hat: 6.6 s and 6.7 s), supporting the idea that runs are elongated whenever the OSN activity is maintained at a constant firing rate. No significant difference is found between the median of the run duration for the plateau (mesa) and the linear hat (cone). The differential effect of the landscape on the sensorimotor control of a run can be accounted for by our predictions of the average modulation of turn

rate prior to turning. Figure 69A shows that a sharp increase of the turn probability over the course of only 2 s is sufficient to induce turning in the well landscape. The volcano landscape yields a milder increase in turning over the course of approximately 4 s, a duration that is consistent with the average latency to turn found in Figure 69B. The increase of the predicted turn probability is weakest for both the plateau (mesa) and linear hat (cone). This observation explains the high prevalence of runs occurring in the central area of the landscape.

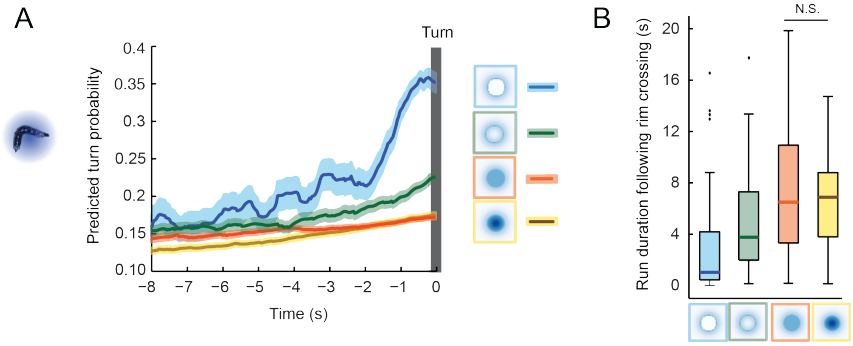

Figure 69. (A) Turn-triggered average of the predicted turn probability for the subset of runs entering the landscape's central area.

(B) Distribution of run durations following the crossing of the landscape's rim (see panel A). Analysis restricted to the subset of runs described in the left graphs of Figure 67 Ai-Di (runs entering the central area of the landscape). The experience of an abrupt decrease in light intensity promotes turning within 2 s ('well' condition) whereas runs are elongated upon experience sustained neural activity elicited by a constant or a linear increase in the stimulus intensity ('mesa' and 'linear' landscapes). The interruption of the predicted increase in turning correlates with the shortening or elongation of the runs observed for the 4 classes of tested landscapes. Differences between the medians of the run duration were tested by applying on a Wilcoxon test with a Bonferroni correction to maintain the confidence level higher than 99% (for the non-significant (N.S.) cases $p>0.05/6$; for all other pairwise comparisons $p<0.05/6$).

Comparing the odor and light gradient architectures

When comparing the behavioral results obtained in odor gradients (Figure 29) to behavioral results obtained in virtual light gradients (Figures 61-69) it is crucial to include differences between the light and odor gradient structure to put behavioral differences found between the two modalities into the context of each gradient's architecture.

Most importantly, the odor gradient is not static, yet constantly evolving over time as opposed to the light gradient that remains constant throughout the time course of an experiment. For the sake of simplicity, a snapshot of the odor landscape 60 s after the initiation of the diffusion process was chosen (Figure 70A) to compare the real odor gradient to the static exponential virtual light landscape (Figure 70B, same gradient as Figure 61). By comparing a normalized cross-section along the odor gradient's peak (Figure 70A, *f(5,y)*) to the normalized cross-section along the peak of the virtual light gradient (Figure 70B, *g(5,y)*, one can appreciate the difference between the two of them: The virtual light gradient is more narrow and represents a perfect exponential increase towards its peak (Figure 70C). The odor on the other hand is slightly broader and deviates from an ideal exponential in that it is more dispersed — likely a result of the diffusion process (Figure 70C). When comparing the derivative of the cross-sections of the odor and light gradients, df/dy and dg/dy, where y represents the variable associated with the vertical axis, one can observe that the slope of the light gradient is considerably steeper than the slope of the odor gradient (Figure 70D).

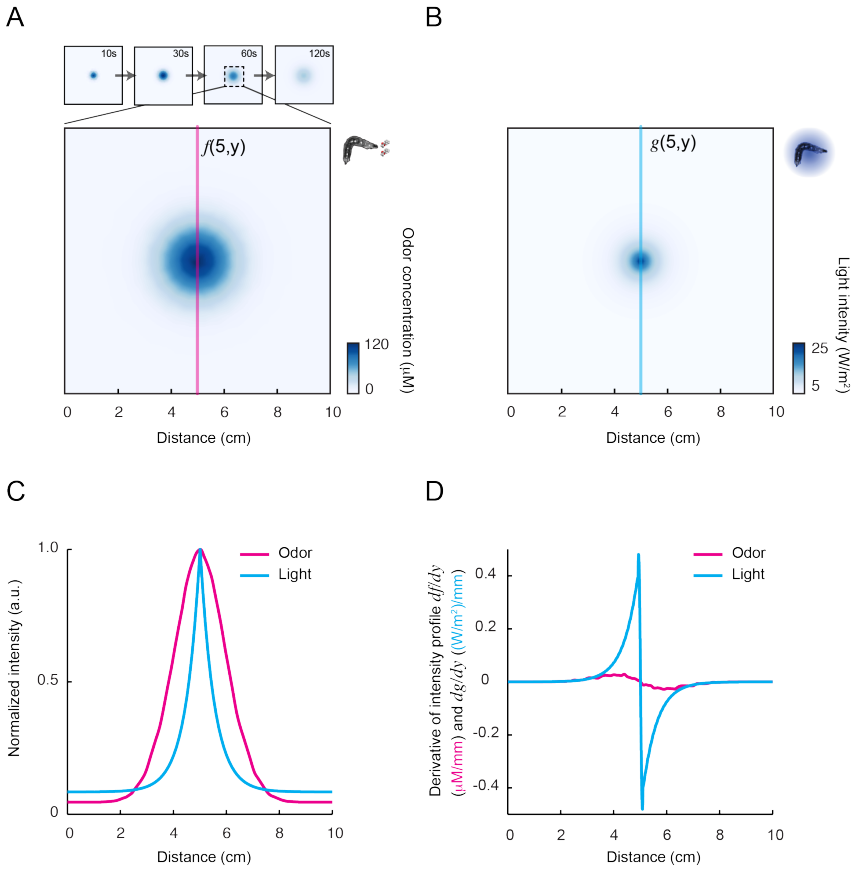

Figure 70. Comparison of geometries of the exponential light gradient and odor gradient.

(A) Reconstruction of the odor gradient displayed in Figure 29 with color-coding according to the scale on the right. Snapshot corresponding to the odor landscape 60 s after the initiation of the diffusion process. Cross-section intersecting the gradient's peak: *f(5,y)*.

(B) Same as panel A for the light gradient presented in Figure 60. Cross-section along gradient: *g(5,y)*.

(C) Comparison of the cross-sections *f* and *g* of the odor and light gradients, respectively. Each profile was normalized by its maximum value reached under gradient's peak.

(D) Comparison of the derivative of the cross-sections of the odor and light gradients: df/dy and dg/dy where y represents the variable associated with vertical axis. From this analysis, it was observed that the slope of the light gradient is considerably steeper than the slope of the odor gradient, which is expected to facilitate chemotaxis.

As a result, chemotaxis in the virtual light gradient is expected to be more effective — a notion ultimately supported by the results reported in this work (see the following section).

Validating the GLM: Studying unconstrained behavior in controlled real odor gradients (closed-loop)

Is the integrated GLM model suitable to predict larval behavior elicited by real odor gradients?

Since the GLM was built to describe open-loop behavior stimulated by synthetic light signals it does not naturally follow that it also applies to free closed-loop behavior elicited by naturalistic odor signals.

From Figure 29A it can be seen that, although the accumulation of larvae at the peak of the odor gradient is evident, the overall precision of the orientation responses seems reduced compared to the exponential light gradient (Figures 61-64). This observation is confirmed when comparing the median distances to the odor source: In the odor gradient larvae on average stayed further away from the source (median distance from odor: 13.3 mm) than in the exponential light gradient (median distance from peak intensity: 7.7 mm) (Figure 71).

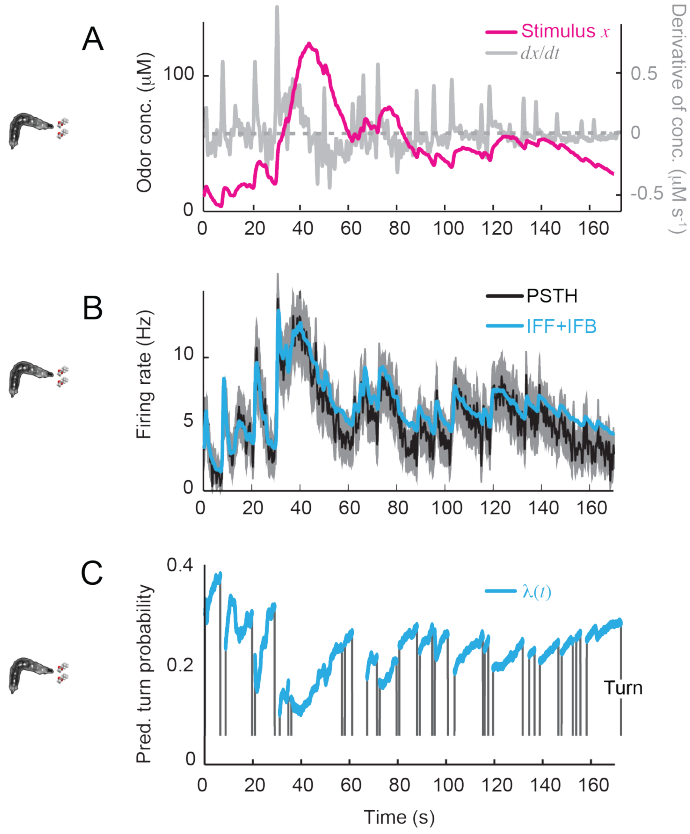

Figure 71. (A) Time course of the reconstructed odor concentration associated with the trajectory displayed in Figure 29B. To compare to data obtained in a virtual light gradient see Figure 62.

(B) PSTH of the OSN measured experimentally in response to a replay of the odor concentration course at the electrophysiology rig (black) (the same as the one presented in Figure 30). Neural activity predicted by the composite IFF+IFB model (cyan) introduced in Figure 40.

(C) Turn probability (cyan) predicted by the stimulus-to-behavior model presented in Figure 54. The predicted turn probability is only shown for the behavioral sequences associated with runs.

In agreement with this idea, the average run duration is significantly longer for the odor gradient (5.4 s) than for the exponential light gradient (3.8 s) (Figure 72 and 64). This decrease in performance is likely due to the larger width of the odor gradient resulting from the shallower nature of the odor gradient architecture (see 'Results section; Comparing the odor and light gradient architectures'). If this assumption holds true, motion in the surroundings of the odor gradient should lead to smoother changes in stimulus intensity, thus only mildly modulating both the OSN activity and the turn probability.

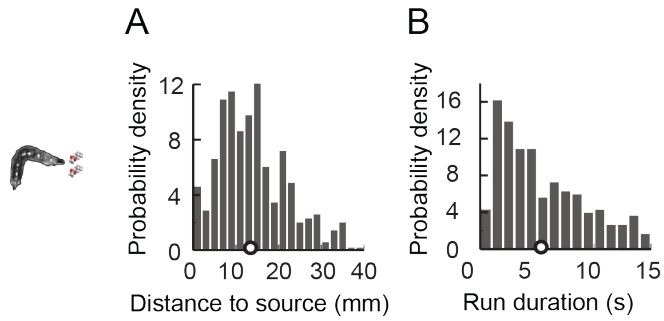

Figure 72. Distribution of distances to the source and the run durations during closed-loop behavioral experiments in an odor gradient.

(A) Radial distribution of the distance to the odor source for runs with a duration longer than 1 s**.** The circles indicate the position of the median of the distribution. Larvae tend to maintain a larger distance from the peak in an odor gradient compared to when they behave in a light gradient (Figure 64).

(B) Radial distribution of the run duration in an odor gradient for runs with a duration longer than 1 s. The circles indicate the position of the median of the distribution (median run duration: 3.8 s).

The integrated model developed for light-driven behavior can be readily adapted to responses elicited in an odor gradient by using the IFF+IFB model to predict the activity of *Or42a* OSN in response to

dynamic olfactory stimulation (Figure 40). In Figure 71B, the goodness of fit between the predictions of the IFF+IFB model (cyan line) and the experimentally observed PSTH (black line) can be appreciated for a representative trajectory. Using the IFF+IFB model, the predicted OSN activity preceding a turn was computed (Figure 71C). Similar to the light gradients tested in Figure 61 et seq., it was found that the average stimulus intensity monotonically decreases for several seconds prior to a turn (Figure 65C). This result is consistent with previous analysis of chemotaxis behavior (Gomez-Marin, Stephens et al. 2011). An analogous trend is observed for the predicted OSN firing rate prior to a turn.

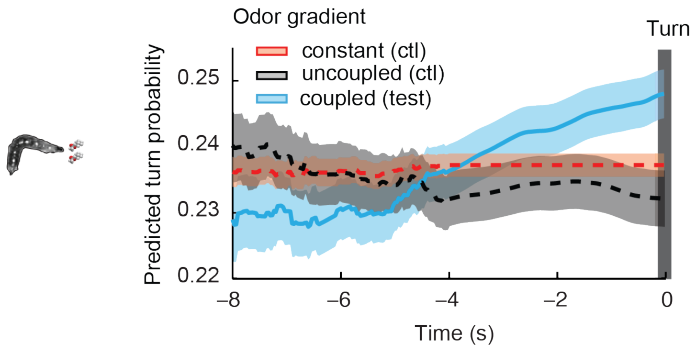

Figure 73. Turn-triggered average of the predicted turning rate for the behavior in the odor gradient. A comparison is made between predictions using the OSN activity driven by a real stimulus intensity (coupled test, cyan), predictions using the OSN activity for time-reversed stimulus time courses (uncoupled control, black) and predictions based on the assumption that the neural activity stays constant over the course of each trajectory (constant control, red). The integrated neural-to-behavior model was trained on the light-evoked behavior reported in Figures 58 and 59. The analysis was restricted to the set of runs lasting at least 4 s and maximum 30 s (53 % of original run set). The predicted turn probability can be seen to increase 4 s prior to the turn.

As a consequence, the average predicted turn probability monotonically increases for several seconds prior to a turn (Figure 73). Since the increase in turn probability is caused by a decreasing OSN activity, we understand why most turning events are found to take place during runs happening down gradient.

Taken together, these results establish that the structure and parameters of the GLM model developed on the basis of the open-loop light stimulations are relevant to predict the behavior produced in controlled odor gradients. The model forms a good conceptual basis to explain how run-to-turn transitions are modulated by the detection of naturalistic olfactory stimuli by the peripheral olfactory system.

Validating the GLM and extending the single OSN paradigm: Navigating virtual light gradients in animals with intact olfactory systems (closed-loop)

All behavioral results shown to this point were obtained in single *Or42a* functional animals. As a consequence, the tested animals are able to sense their olfactory environment with only one functional channel — an extremely unnatural situation. Are these findings also relevant in animals with an intact olfactory system?

To address this question, animals expressing ChR2 in the *Or42a* OSN with the rest of the olfactory system intact were tested through optogenetic behavioral experiments using the open-loop paradigm. As described previously, the onset of a given run was either associated with the test condition (an 8s-linear light ramp) or the

control condition (constant basal light intensity). Figure 74 shows the evolution of the resulting turn probability during the linear light stimulation in single functional animals (compare to Figure 57D left) and *Or42a* functional within the WT background.

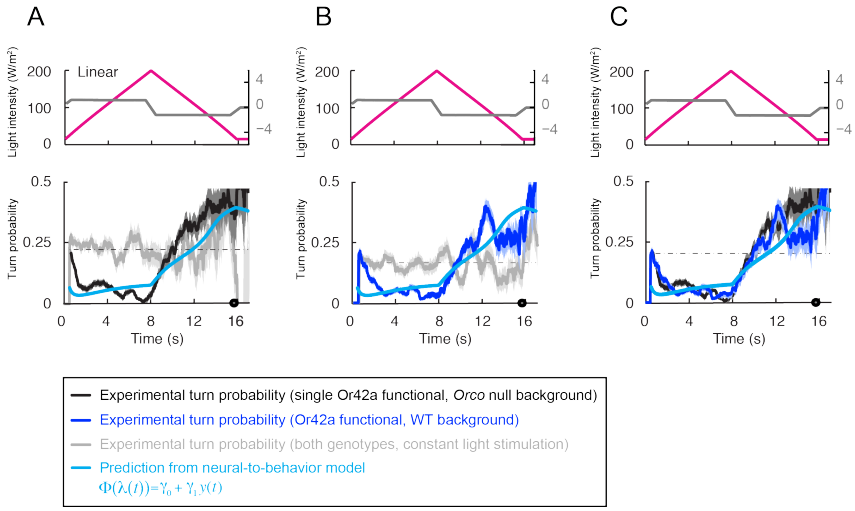

Figure 74. Application of the stimulus-to-behavior integrated model to predict behavior to a linear light ramp (model introduced in Figure 54). The test model (cyan) is based on the neural activity modeled by the IFF motif. The dashed horizontal line in the background represents the average turn probability observed upon stimulation at constant intensity.

(A) Turn probability estimated from an experimental set of trajectories obtained in *Or42a* single functional animals upon constant stimulation (light gray) and stimulation by a linear light ramp (black) (same data as Figure 59D left).

(B) Turn probability estimated from an experimental set of trajectories obtained in *Or42a* functional, WT background animals upon constant stimulation (light gray) and stimulation by a linear light ramp (blue).

(C) Turn probability estimated from an experimental set of trajectories obtained in both genotypes shown in panels A and B (single *Or42a* functional, black; WT OSN background, blue) upon stimulation by a linear light ramp. The turn probabilities obtained in both genotypes are very similar.

Interestingly, the turn probabilities are very similar in both cases, suggesting that even in animals with a fully functional olfactory system an animal's behavior — when stimulated — is mainly governed by the signal it receives through the one *Or42a* OSN expressing ChR2.

Or42a functional, WT background animals were subsequently tested in a virtual light gradient in closed-loop conditions. Consistent with the findings obtained in open-loop conditions (Figure 74), WT background larvae are attracted to the highest light intensity of the virtual light gradient (Figure 75).

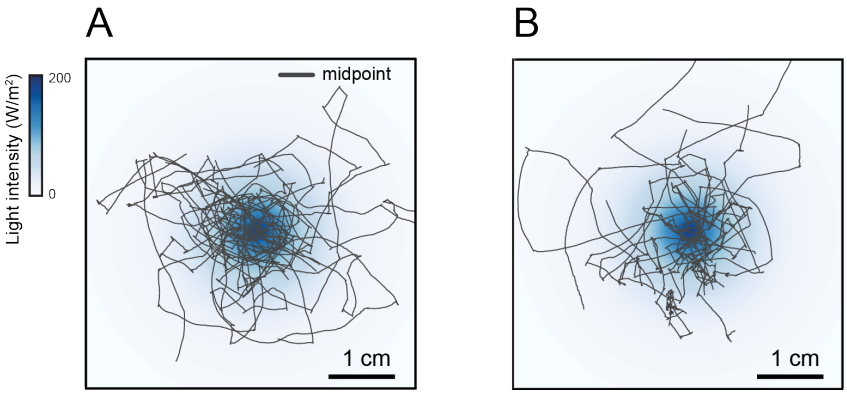

Figure 75. Synthetic chemotaxis of larvae in a virtual odor gradient produced by light stimulation. Each larva experiences a light intensity determined by a predefined stimulus landscape. The landscape displayed in the background is an exponential gradient centered on a point 'source' (light gradient identical to the one shown in Figure 60).

(A) Overlay of 10 trajectories of *Or42a* single functional animals recorded in the virtual light gradient (same data as Figure 60A). Larvae evolving in this light gradient accumulate at the peak of the gradient.

(B) Overlay of 10 trajectories of *Or42a* functional, WT background animals recorded in the virtual light gradient. Similar to single functional animals, larvae accumulate at the peak of the gradient.

With regards to their overall navigation, WT background larvae appear to be slightly less precise compared to *Or42a* single functional animals. The results of these control experiments underline the relevance of the findings obtained for single *Or42a* functional animals by putting them into the context of an overall intact olfactory system.

Likelihood analysis of larval behavior in controlled olfactory environments

How good are the behavioral predictions obtained from the GLM?

To assess the quality of the behavioral predictions obtained from the GLM described in equation (13), the likelihood associated with the observation of the entire set of runs obtained in the closed-loop light and odor gradients was calculated (analysis performed by Matthieu Louis). The likelihood of the ensemble of runs observed in the odor and light gradient was calculated on the time course of the predicted turn probability (Figure 73 and 77A for the odor gradient, Figure 76A for the light gradient). Considering that the total number of runs observed in a particular gradient was *N*, the likelihood of the i^{th} run was computed based on the turn probability predicted on bins of 1 s. Since relationship (13) gives the turn probability in seconds, the probability of observing a turn between time *t* and (*t* + 1 s) is: $\lambda_i(t)$ where the index *i* refers to the sensory experience associated with the i^{th} run. The probability of not turning during the same time interval is: $1 - \lambda_i(t)$. The probability of observing a given run lasting 5.6 s can be estimated as:

$$p_i = \left(1 - \lambda_i(0.6)\right) * \left(1 - \lambda_i(1.6)\right) * \left(1 - \lambda_i(2.6)\right) * \left(1 - \lambda_i(3.6)\right) * \lambda_i(4.6) \quad (16)$$

Finally, using relationship (15), the likelihood of the entire set of runs was calculated as:

$$L = \prod_{i=1}^{N} p_i \quad (17)$$

The value reported in Figures 76B and 77B is the logarithm of *L*. Next, the log-likelihoods (logL) of the predictions associated with the test model and the two controls were calculated (see also Table 6 and 'Results section; From stimulus to neural to behavior: Building a generalized linear model (GLM) to predict larval behavior'). To evaluate the reliability of differences between the test model and controls, a standard bootstrap approach (Martinez and Martinez 2001) was applied. From the original collection of runs, 10,000 independent new samples of runs were generated based on random resampling with replacement. For each sample, the logL of the test model and the controls was computed.

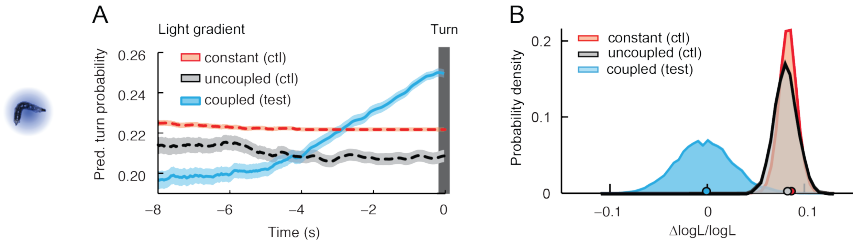

Figure 76. (A) Turn-triggered average of the predicted turn probability for the exponential light gradient. A comparison is made between predictions based on the OSN activity driven by the stimulus intensity (test model, cyan), predictions using the OSN activity driven by the time-reversed stimulus time course (uncoupled control, black) and predictions based on the assumption that the neural activity stays constant over the course of each trajectory (constant control, red). The stimulus-to-behavior model was trained on the stimulation protocols presented in Figures 58 and 59. The turn probability can be seen to steeply increases 4 s before the turn, highlighting the stereotypy in the sensorimotor control of run-to-turn transitions.

(B) Log-likelihood of the predictions of the neural-to-behavior model compared to the controls. Bootstrap analysis of the difference in log-likelihood (logL) between the test model and the controls normalized by the log-likelihood of the test model ($DlogL/logL_{test}$). Distribution of the relative difference in logL is shown for the test model against the constant neural activity control (red), and the uncoupled stimulus control (gray). The median of the distribution is equal to the value obtained from the original full set of runs; the median is indicated by a dot in the x-axis. As an internal control, the neural-to-behavior model was tested against itself (blue). Out of 10,000 resampled subsets of runs, none of the controls were found to be more likely than the test model ($p<0.0001$). The analysis was restricted to the set of runs with a duration comprised between 4 s and 30 s (44 % of original run set).

Next, the relative difference in logL of the model and control was computed:

$$\frac{\Delta \log L}{\log L_{test}} = \frac{(\log L_{test} - \log L_{control})}{\log L_{test}}$$

The distribution of this variable is reported in Figure 76 for the behavior induced by light and Figure 77 for the behavior induced by the odor gradient. Finally, the number of instances where $\frac{\Delta \log L}{\log L_{test}}$ is lower than 0 (control outperforming the test model) was computed. A p-value was derived for the hypothesis that the test model yields a larger likelihood than the controls. Overall, it was found that the test model generates predictions that are more likely than the controls where the OSN activity is assumed to be constant or the sensory experience is uncoupled with the behavior.

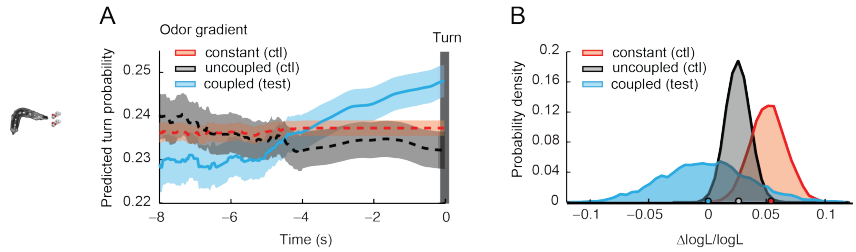

Figure 77. (A) Turn-triggered average of the predicted turning rate for the behavior in the odor gradient. A comparison is made between predictions using the OSN activity driven by a real stimulus intensity (coupled test, cyan), predictions using the OSN activity for time-reversed stimulus time courses (uncoupled control, black) and predictions based on the assumption that the neural activity stays constant over the course of each trajectory (constant control, red). The integrated neural-to-behavior model was trained on the light-evoked behavior reported in Figures 58 and 59. The analysis was restricted to the set of runs lasting at least 4 s and maximum 30 s (53 % of original run set). The predicted turn probability can be seen to increase 4 s prior to the turn.

(B) Log-likelihood of the predictions of the integrated neural-to-behavior model compared to the controls. Bootstrap analysis of the difference in log-likelihood (logL) of the test model and the controls normalized by the log-likelihood of the test model ($DlogL/logL_{test}$). Distribution of the relative difference in logL computed for the test model against itself (cyan), against the constant neural activity control (red), and against the uncoupled stimulus control (gray). The median of the distribution is equal to the value obtained from the original full set of runs; the median is indicated by a dot in the x-axis. Based on 10,000 resampled subsets of runs, it was concluded that the test model is significantly larger than both controls ($p=0.0026$ for the constant neural activity control and $p<0.0001$ for the uncoupled stimulus control). The analysis was restricted to the set of runs with a duration comprised between 4 s and 30 s.

Discussion

Navigation through natural environments presents a crucial and constant challenge that most living organisms (unless they are plants) need to take up. Sensory-guided orientation strategies provide the means to continuously challenge this problem. The accumulation of successful navigation maneuvers (i.e. avoiding predators or navigating towards more nutrient rich environments) will ultimately result in augmenting the life span of individual organisms and thereby directly contribute to the long-term survival of any given species.

Larval chemotaxis is a perfect example of a sensory-guided orientation maneuver that largely depends on a very specific part of the sensory system: Olfaction[1]. This makes chemotaxis ideally suited to examine the impact of continuous olfactory stimuli on behavioral transitions driving the orientation of larvae ascending odor gradients. Simple sensory-guided behavior can be even further simplified by studying *Drosophila* larvae in which the control of olfactory behavior is reduced to the information mediated by a single pair of OSNs (single OSN functional animals). This approach is viable, as the capacity of single OSNs to direct orientation decisions remains comparable to wild type (Fishilevich, Domingos et al. 2005; Louis, Huber et al. 2008). This work focused on the OSN expressing the *Or42a* odorant receptor whose response profile has been characterized in detail in response to pulses of various odors (Kreher, Kwon et al. 2005; Kreher, Mathew et al. 2008;

[1] In addition there is crosstalk between other sensory modalities that is affecting the function of the olfactory system.

Asahina, Louis et al. 2009; Mathew, Martelli et al. 2013). IAA was chosen as a representative odor as it is known to elicit robust chemotaxis in single functional *Or42a* OSN larvae (Fishilevich, Domingos et al. 2005; Louis, Huber et al. 2008; Gomez-Marin, Stephens et al. 2011). In addition, IAA elicits neural activity of the *Or42a* OSN with relatively low firing rates that are well reproducible with ChR2.

The first aim of this project was to examine how naturalistic olfactory stimuli, as larvae experience them during free chemotactic behavior, are encoded in the activity pattern of the *Or42a* OSN.

The second aim was to reverse engineer the neural signal elicited by naturalistic odor stimuli with the help of optogenetics. This objective was achieved by deploying light intensity as a proxy representing the odor concentration in animals expressing the light gated ion channel ChR2. By varying the light intensity in real time OSN activity patterns very similar odor-evoked activity were achieved.

The third aim was to accomplish larval chemotaxis behavior in response to purely light evoked OSN activity, and to use this approach to identify relevant features of OSN activity triggering behavioral transitions during chemotaxis.

To record the firing rate of single functional OSNs, a new extracellular recording technique was devised to obtain responses from a single functional larval OSN (Figures 4 and 5). This technique advanced pioneering recordings from fully intact olfactory systems (Oppliger, P et al. 2000; Kreher, Kwon et al. 2005). Recordings from the antennal nerve required to carefully discard

spikes originating from non-olfactory sensory neurons — neurons innervating the dome of the dorsal organ that might be implicated in functions related to gustation, thermosensation and mechanosensation (Gerber and Stocker 2007). Spike sorting was achieved by taking advantage of optogenetics to identify the waveform of the action potentials originating from the OSN of interest (Figure 5). Unlike previous studies that concluded that odor representations are inherently fuzzy in the peripheral olfactory system of the larva (Hoare, McCrohan et al. 2008; Hoare, Humble et al. 2011), the activity of the *Or42a* OSN was found to be highly reproducible across trials and preparations (Figures 30 and 34). The trial-to-trial reproducibility of the recordings might be explained by the enhanced stability of the recording technique that, in principle, permits to record the activity of any neuron that can be both easily accessed and genetically targeted.

Most primary sensory neurons operate differently from simple proportional counters (Rieke 1997; Song, Postma et al. 2012). When stimulated by an odor ramp, the activity pattern of the OSNs captures features associated with the time derivative of the stimulus. As an extreme case, the OSNs of *C. elegans* and cockroaches operate as bipolar ON or OFF detectors that respond to either increases or decreases in stimulus intensity (Tichy, Hinterwirth et al. 2005; Chalasani, Chronis et al. 2007). In adult flies, it has been demonstrated that the activity pattern of a single OSN comprises features pertaining to complex dynamical features of the airborne odor stimulus (Martelli, Carlson et al. 2013). It has also been shown that adult fly OSNs represent changes in the stimulus derivative

(Kim, Lazar et al. 2011) — a property that can be partially accounted for by a linear-nonlinear (LN) model (Nagel and Wilson 2011). In agreement with these observations, the results presented here indicate that the larval *Or42a* OSN realizes an unsuspected degree of information processing. The OSN activity exhibited a high sensitivity to in response to the first derivative of the stimulus (speed) as well as its temporal variation (acceleration). In addition, a high degree of nonlinearity was uncovered since the OSN response to increases and decreases in stimulus intensity was proven to be strongly asymmetrical (Figures 34 and 35). The OSN response pattern appears to be conserved over a wide timescale. The activity level of the OSN in response to the light ramps seems to be proportional to the background intensity enabling the neuron to perform fold-change detection (Figure 50).

Attempts to model the *Or42a* OSN response properties with an LN model proved unsatisfactory (Figures 38 and 39), as was the case for adult OSN (Kim, Lazar et al. 2011). This result is not surprising in the light of the nonlinearity of the larval OSN response characteristics (Figures 34-36). As a consequence, an alternative modeling formalism was explored to capture the core regulatory mechanisms underlying olfactory transduction and spike generation (work of Matthieu Louis and Alex Gomez-Marin) (Figure 40 et seq.). Inspired by models describing sensory adaptation in bacterial chemotaxis (Barkai and Leibler 1997; Tu, Shimizu et al. 2008), a system of ordinary differential equations (ODEs) was explored and a coarse-grained mathematical description of the olfactory transduction cascade of the *Or42a* OSN established (Figure 40 et

seq.). To date, the olfactory transduction cascade in *Drosophila* is still widely uncharacterized; the firing rate was therefore modeled phenomenologically as the function of the stimulus intensity. The model relied on the combination of two regulatory motifs known to play a role in chemosensation:

(1) a negative integral feedback motif (IFB) that also forms the core mechanism regulating bacterial chemotaxis (Yi, Huang et al. 2000) and
(2) an incoherent feedforward loop (IFF) (Kato, Xu et al. 2014) that was used in *C. elegans* to describe the transfer function converting an olfactory input into the OSN activity.

The negative IFB mechanism (1) has been hypothesized to directly contribute to the olfactory transduction pathway in adult flies (Nagel and Wilson 2011).

The two motifs are outlined in Figure 40A-B. The type-1 IFF (2) features a dual effect of the stimulus on the OSN activity: fast excitation and delayed inhibition (Alon 2007). In invertebrate olfaction, it is plausible that the molecular correlate of the IFF involves the negative effect of calcium bound to calmodulin on cation channels (Gu, Lucas et al. 2009). The IFB motif (1) would thus act directly on the odor transduction pathway of the odorant receptor (OR) whereas the IFF motif would act on voltage-gated ion channels further downstream.

As shown in Figure 40B, the IFF and IFB motifs can be described by two simple 3-element circuits (Milo, Shen-Orr et al. 2002; Alon 2007). To delineate the contribution of each motif, a non-biased approach was adopted by optimizing the parameters of a circuit that

combines the IFF and IFB motifs. In the past, this approach was successfully applied to reverse engineer the regulatory circuits controlling developmental processes (Cotterell and Sharpe 2010; Lim, Lee et al. 2013). Similarly, a lot of contributions leading to a deeper understanding of neural circuit functions were attained by screening circuit motifs and corresponding parameter values (Prinz, Bucher et al. 2004; Dunn, Conery et al. 2007). Starting with experimental patterns of odor-driven activity, the model was trained against the stereotyped ramps presented in Figures 35 and 36 together with the naturalistic stimulus shown in Figures 29 and 30. For the light-driven activity of the *Or42a*>ChR2 OSN, the parameters of the model were optimized separately on the ramps and naturalistic stimulus (Figures 41-43 and Figure 61B). In spite of the simplicity of the 3-element circuit describing the function of the *Or42a*>ChR2 OSN, the results of the optimized model were able to recapitulate the richness of the OSN dynamics with remarkably high accuracy (Figures 41-43, Figure 61B). Figure 40 (panels C and B) illustrates that the strength of the IFF pathway is stronger compared to the IFB. Yet the IFB contribution to the dynamics significantly contributes to the goodness of the fit for non-stationary stimulation. With regards to light evoked activity through ChR2, the parameter optimization indicates that the contribution of the IFB pathway is not required. This important observation reinforces the idea that the IFB captures a negative feedback specific to the odorant receptor that would not affect the transduction process mediated by ChR2. Odorant receptors and channelrhodopsins belong to distinct families of proteins: G-protein-coupled-receptor (GPCR) photoreceptors and non-GPCR chemoreceptor (Benton, Sachse et

al. 2006; Yau and Hardie 2009) making it unlikely that these two channels share the same signaling pathway. On the other hand, both insect ORs and channelrhodopsins are known to be ionotropic channels, a feature that could explain why the response dynamics elicited by both odor and light bears such a striking resemblance. How can this similarity be explained? Excitation and inhibition of the OSN activity could be due to direct channel gating. The channel gating process would spark an ionotropic spike-generation mechanism shared by the light and odor pathways. In the *Or42a* OSN, the activity elicited by odor and light was similar enough to replace naturalistic patterns of odor concentration by time-varying patterns of light. While the involvement of a metabotropic signaling cascade appears unlikely in the case of ChR2 there is mounting evidence that it may play an important role in ORs (Wicher, Schäfer et al. 2008; Nakagawa and Vosshall 2009; Wicher 2010; Martin 2011; Stengl and Funk 2013; Wicher 2013). The necessity to include the IFB motif to achieve a good fit of the modeled odor response hints at the presence of a metabotropic signal transduction cascade in *Drosophila* OSNs.

Although surprisingly complex at first, the computation achieved by a single OSN is reminiscent of the operation performed by a single cell controlling chemotaxis or sensing developmental factors (Goentoro and Kirschner 2009; Shimizu, Tu et al. 2010; Shoval, Goentoro et al. 2010). It has been shown in adult *Drosophila* that OSNs are in fact sensitive to the stimulus speed, (Kim, Lazar et al. 2011). Two salient characteristics of the OSN transfer function are that the OSN displays strong inhibition in response to a rapid decay

of the stimulus intensity; sustained OSN activity on the other hand is only observed when the stimulus undergoes constant acceleration. Such accelerations are typically encountered in single-odor-source gradients with Gaussian profiles where runs directed towards the odor source will generate exponential increases in stimulus intensity. To test this working hypothesis, one would have to study behavior in response to controlled and repeatable patterns of OSN activity. The limitations inherent to the control of airborne odorant molecules rendered this approach untenable for real odors. However, through the use of optogenetics and by substituting the odor stimulus with light stimulation, an unprecedented control over the activity elicited in a single OSN was achieved. In a novel tracker (Figures 21 and 52), *Drosophila* larvae were exposed to light patterns with a fixed temporal profile of ramps whose OSN response had previously been characterized by means of electrophysiology. In such 'virtual olfactory realities' the behavioral effect of reproducible patterns of the OSN firing rate on run-to-turn transitions was thoroughly tested. To allow comparison across trials, the beginning of the light ramp was always locked with the onset of a run. The ramp was terminated as soon as the larva switched from a run to a turning maneuver (actions including stop, head cast and turn). Through this approach, generic features in OSN activity sufficient to elicit behavioral transitions could be characterized: OSN inhibition promotes turning whereas a sustained or rising activity of the OSN suppresses turning (Figures 56-59). The analysis also revealed that the activity of the OSN could be fully inhibited by negative odor gradients.

Based on the experimental findings of this work, an integrated mathematical model quantitatively describing this control rule was developed for run-to-turn transitions (Figure 54) (work of Matthieu Louis and Alex Gomez-Marin). This model spans different levels of organization of the neural circuitry controlling chemotaxis: the encoding of the stimulus by the peripheral OSNs and the conversion of this information into a binary decision between the maintenance and the interruption of an ongoing run. To establish the validity of the behavioral predictions of the model to closed-loop unconstrained behavior, the stimulation paradigm was modified in such a way as to give larvae full control over their sensory experience. The geometrical properties of the gradients were chosen to permit larvae to collect sensory information leading to predictable modulations of run-to-turn transitions. Light landscapes were designed with a common geometrical configuration: a radial symmetry similar to odor gradients, and an exponential slope leading to a rim located at a fixed distance from the center of the landscape. Different geometries were tested for the area inside the rim; those geometries were chosen to create sensory experience with a predictable pattern neural activity intended to produce distinct behavioral outcomes by triggering certain behavioral transitions. For the well landscape, a transition from an exponential stimulus increase in to an abrupt decrease produces a predictable interruption of runs. The slightly milder decrease in stimulus intensity experienced by larvae in the volcano landscape induces turning in a predictably smoother way. Runs are elongated when the OSN activity is maintained at a moderately high level in the mesa landscape. The experimental results also support the

counterintuitive prediction that run-to-turn transitions found in the plateau case should be undistinguishable from the ones found in a linear increase in light intensity. Thus, the integrated model — developed in open–loop conditions — was successfully validated by findings obtained in freely behaving animals in closed-loop settings (Figures 67 and 68). It clarifies how features encoded in the activity of peripheral sensory neurons regulate the probability of run-to-turn transitions — a conceptual advance that complements recent work in *C. elegans* (Kato, Xu et al. 2014) and the *Drosophila* larva (Klein, Afonso et al. 2015). The model also corroborates the idea that sensory representations are rapidly transformed into motor representations in the circuit controlling chemotaxis (Luo, Wen et al. 2014). The inhibitory interneurons located in the larval antennal lobe (Gerber and Stocker 2007; Das, Gupta et al. 2013) are nonetheless expected to filter the olfactory information arising from the OSNs (Asahina, Louis et al. 2009; Larkin, Karak et al. 2010). The good performance of the model with regards to its predictions at the level of single runs, suggested that the impact of computations in neurons downstream from the OSN on the behavior seems minimal in the context of larval chemotaxis. However, the model's accuracy is expected to improve through the addition of downstream circuits of the olfactory system.

Ultimately, the model was tested on the closed-loop behavior elicited by a controlled real odor gradient. In Figure 71, it can be seen that the predicted evolution of the turning rate is on average in good agreement with the observed transitions from run to turn. This outcome is striking considering that the model underlying the

behavioral predictions was trained on data obtained in an open-loop paradigm purely using light stimulation. The basic structure of the model must therefore comprise control features that are fundamental to the selection of orientation behaviors in response to the activity of the peripheral olfactory system. Nonetheless, it is evident that the model cannot account for the entire complexity of the orientation strategies underpinning larval chemotaxis. To achieve accurate predictions on single runs, it might be necessary to integrate the contribution of weathervaning to the control of run-to-turn transitions, together with potential history-dependence effects of past runs and turns on subsequent runs. It is also plausible that the outcome of the orientation decision associated with a given turn — whether or not the larva corrects its motions towards the gradient — might influence the persistence of the following run.

To extend the relevance of the single functional *Or42a* OSN paradigm into the realm of a fully intact olfactory system, *Or42a* functional, WT background animals (with a fully functional olfactory system) were tested under both open- and closed-loop conditions (Figures 74 and 75). The obtained behavioral results were very similar for both genotypes. These observations underline the relevance of all the findings obtained for single *Or42a* functional animals by putting them into the context of an overall intact olfactory system.

The overall accuracy of the behavioral predictions achieved by the GLM depended highly on the nonlinear transformation of the stimulus by the transduction cascade of the OSN. This transformation could be partially reproduced by feeding the GLM

with a linear combination of the stimulus intensity and its first derivative (Figure 55 and Table 6). The decrease in the goodness of fit highlighted the behavioral relevance of the nonlinear processing achieved within the OSN.

The multilevel model described in this work is able to predict the control of run duration as a function of the activity transmitted by one single OSN — *Or42a*. In the future, the present model should be extended to OSNs expressing other odorant receptors. Can the neural activity in other neurons likewise be described by the IFF/IFB motif valid for the *Or42a* OSN? Do other ORs play different roles within the circuit? How is it that some OSNs seem to respond only to a handful of odors while *Or42a* is broadly tuned? In various flying insects, OSNs are capable of tracking rapid odor pulses on sub-second timescales and differentiating this signal (Kim, Lazar et al. 2011; Fujiwara, Kazawa et al. 2014; Szyszka, Gerkin et al. 2014). Whether the sensorimotor model proposed here applies to the integration of turbulent olfactory inputs happening at faster time scales remains to be defined. To this end, the OSN response was characterized in conditions inspired by those experienced during lateral head movements (Figures 45-49), yet no behavioral experiments were carried out.

In adult *Drosophila* it has been shown that at the circuit level, the net effect of lateral input to a PN is generally inhibitory (Wilson 2013). When putting the IFF/IFB circuit motif governing the OSN activity of the *Or42a* OSN (Figure 40) into the context of the broader olfactory circuit, while assuming that the outlined principles similarly hold for the larval olfactory circuit, IFF motif correctly describes the

structure of the overall olfactory circuitry up to the PN level, just beyond the antennal lobe (Figure 78). It remains to be confirmed whether the IFF/IFB motif is equally applicable to other OSNs. However, if this is so, each OSN within the olfactory circuitry may represent an independent IFF/IFB element, which, taken together forms a sum total that — as a whole — could be considered as the activating part (Figure 78 – I) of an overarching IFF motif. In this motif, PNs, transmitting the processed olfactory information, are directly activated by OSNs (Figure 78 – I, PN activity denoted as *Y*). OSNs, on the other hand, also activate LNs, which in turn inhibit PNs. The LN activity therefore represents the intermediate variable (*U*) (Figure 78 – II), acting as an inhibitor of the resulting PN activity. This observation suggests that the larval olfactory circuit may represent a nested self-similar system in which each single component is governed by the same dynamics as the embedded overarching system.

How such a system could accomplish the seemingly insurmountable task of sensing and discriminating high-dimensional signals at various time scales has been addressed in a recent study performed in adult *Drosophila* by Kim et al. in which the authors characterize the response of PNs combined with the dynamic sensory encoding by OSNs (Kim, Lazar et al. 2015). The study finds that PNs signal the rate of change and the acceleration of odor concentration signals to higher brain centers.

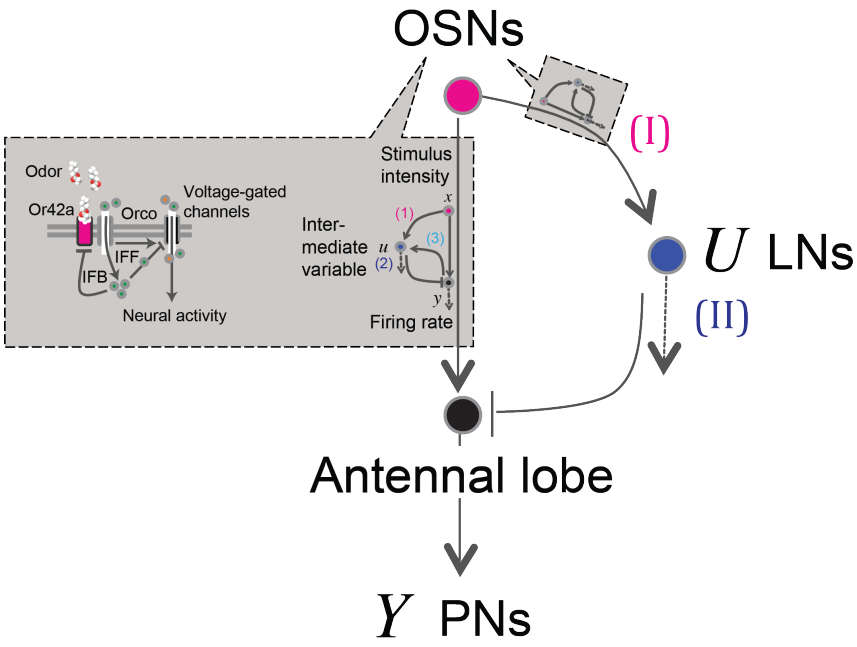

Figure 78. Nested IFF circuit motif applied at the at the circuit level of the larval olfactory system. The IFF motif correctly recapitulates the dynamics of the neural activity as it is seen at the circuit level (Wilson 2013). OSNs form synapses with both PNs and LNs. OSNs activate both PNs and LNs (I). LNs on the other hand mainly inhibit PNs (II) thus creating the inhibitory arm of an overarching IFF motif.

These findings support the notion that even at a circuit level the sensory information processing — though through entirely different cellular mechanisms — appears to be governed by similar principles as odor intensity information processed in a single OSN. However, the signal converging from the concerted activity of multiple OSN at the level of the antennal lobe conveys an even higher dimensionality, as in addition to odor intensity, information with regards to the odor quality is embedded within the neural population activity. The decoding of both quantitative and qualitative odor information at the level of the antennal lobe and

how it relates to population coding, gain control and signal amplification is currently a highly researched topic. To elucidate all of the ALs processing functions it will be needed to examine and functionally dissect the neural circuitry down to the single synapse level. This is especially needed for the highly heterogenic and all interconnecting local interneurons that are likely involved in a multitude of difference processing functions each of which could be tailored to a different network state.

When taking an evolutionary perspective it is at least perceivable that the olfactory system slowly evolved from autonomous sensors. Over time they would have started to come together to form a circuitry mirroring the dynamics governing each element of the circuitry. The resulting self-similar dynamics of the odor processing circuitry definitely seems well suited to perceive odors from the outside world whose statistics also exhibit self-similar multi-timescale features extending over several orders of magnitude.

The *Drosophila* larva offers a unique opportunity to examine how neural circuits implement sensorimotor algorithms underpinning a wide range of behaviors (Ohyama, Jovanic et al. 2013; Vogelstein, Park et al. 2014). In the future, interdisciplinary approaches combining behavioral screens, electrophysiology, functional imaging, and circuit reconstruction with virtual sensory realities on the one hand (Yao, Macara et al. 2012), and computational modeling and robotics on the other hand (Grasso, Consi et al. 2000; Webb 2002; Izquierdo and Lockery 2010; Ando, Emoto et al. 2013), could bring about major improvements in our understanding of how

brains with reduced numerical complexity exploit streams of sensory information to guide behavior.

Conclusion

While this project started off by developing a new extracellular recording technique with which OSN responses to simple, static odor pulses were characterized. However, with the advent of optogenetics, the my thesis work quickly progressed into the quantitative study of the peripheral olfactory system that you see in front of you.

The very first behavioral experiments that took advantage of a simple static light gradient were performed with larvae that were not blind. Although the light avoidance reaction was not abolished, it was transiently overridden in animals that showed temporary attraction to the virtual odor stimulus. These early findings represented the first reassuring hint that changing the light intensity could approximate a change in odor concentration. Still, the innate light avoidance reaction was too strong to be superseded by an attractive virtual odor stimulus. It thus became clear that virtual chemotactic behavior in response to light stimuli could only be elicited in animals that were truly blind. To this end two alleles (GMR-hid and dtrpA1[1]) were crossed into an anosmic background while at the same time expressing Chr2 and rescuing the function in one single OSN through *Orco*. Astonishingly, larvae expressing ChR2 in a blind background showed in fact a clear attraction to blue light stimuli.

The light stimulation was quickly set up at the electrophysiology rig and put into action to record the first responses evoked by light flashes. A thorough characterization of the ChR2 evoked light

response to different light flashing patterns followed suit. In the meantime the quantitative odor stimulation at the electrophysiology rig was made possible through the employment of a new microfluidic pressure pump in conjunction with custom multi-barrel pipettes. In order to get a better handle on the OSN response dynamics a new stimulation program was written to support the stimulation of more complex linear and non-linear ramps. The same ramps were subsequently transformed into light intensities to elicit light evoked neural activity comparable to the one elicited by isoamyl acetate.

In the end, by taking advantage of the closed-loop tracker, the different building blocks of the project were finally assembled to build a quantitative model not only describing the neural activity in response to both odor and light stimuli, yet that would use the modeled neural activity to predict larval behavior.

This work outlines tools and techniques necessary to successfully extract and reverse engineer behaviorally relevant features of sensory information in the context of a given behavior, a very powerful approach when applied to studying sensory systems. It allows closing the sensorimotor loop for a robust, well-defined behavior and to study it as the function of a sensory stimulus. In the case of the larval olfactory system, however, to know the stimulus time course was not enough: The non-linear transfer function governing the activity of sensory neurons required the development of a model suited to quantitatively describe the relationship between the stimulus and the elicited neural activity. This relationship was established through the introduction of optogenetics while testing

the neural response to both odor and light stimuli. Once the activity of the sensory neuron was modeled accurately, quantitative behavioral predictions turned out to be possible. In principle, this approach should be applicable to any well-defined, genetically manipulable sensory system.

The journey through this project has been an incredible endeavor, an infinite learning process and a truly challenging multidisciplinary effort. Through the simplification of the already simple olfactory system of *Drosophila* larvae I was humbled to experience the incredible amount of complexity still present in a simplified neural system that, in principle, receives input from only one OSN. I learned how a single OSN acting as a slope detector is able to sense both the speed and the acceleration of the stimulus time course, and I was surprised that even animals with very small brains show highly individual behavior that is remarkably hard to predict. But to see larvae chemotacting in a virtual light gradient, hence proving that the reverse engineering approach was succeeding was among the most astonishing experiences I was allowed to live through in this project.

Abbreviations

A	Absorbance
AC	Alternating current
AL	Antennal lobe
Ca	Calcium
CaM	Calmodulin
CaMKII	Calmodulin-dependent protein kinase II
cAMP	Cyclic adenosine monophosphate
ChR2	Channelrhodopsin-2
DAC	Digital-to-analog converter
DAG	(1,2)-diacylglycerol
DO	Dorsal organ
EAG	Electro-antennography
eLN	excitatory local interneuron
GLM	Genleralized linear model (behaviour)
FT	Fourier transform
GABA	gamma-Aminobutyric acid
GFP	Green fluorescent protein
Glu	Glutamate
HEPES	4-(2-hydroxyethyl)-1-piperazineethanesulfonic acid
iLN	inhibitory local interneuron
IAA	Isoamyl acetate (a.k.a. isopentyl acetate, IUPAC: 3-methylbut-1-yl ethanoate)
ICD	In-Circuit Debugging
ID	Inner diameter
IFB	Incoherent feedback
IFF	Incoherent feed forward
IP3	Inositol (1,4,5)-trisphosphate
$InsP_3R$	Inositol (1,4,5)-trisphosphate receptor
IR	Infrared
ISI	Inter-spike-interval
LED	Light emitting diode
LFP	Local field potential
WT	Wild type (throughout this work WT refers to the genotype W1118)
LN	Local interneuron
LTCU	Larval tracker control unit

MB	Mushroom body
MFCS	Microfluidic control system
Na	Sodium
OD	Outer diameter
OR	Olfactory receptor
Orco	Odorant receptor co-receptor (formerly known as Or83b)
OSN	Olfactory sensory neuron
ORN	Olfactory receptor neuron (see OSN)
PC	Personal computer
PDE	Partial differential equation
PIC	Programmable Interface Controller
PID	Photoionization detector
PN	Projection neuron
PSTH	Peristimulus time histogram
RJ	Registered Jack
SQP	Sequential Quadratic Programming
TTL	Transistor–transistor logic

Bibliography

Abraham, N. M., H. Spors, et al. (2004). "Maintaining accuracy at the expense of speed: stimulus similarity defines odor discrimination time in mice." Neuron **44**(5): 865-876.

Ache, B. W. and J. M. Young (2005). "Olfaction: diverse species, conserved principles." Neuron **48**(3): 417-430.

Ackers, G. K., A. D. Johnson, et al. (1982). "Quantitative model for gene regulation by lambda phage repressor." Proc Natl Acad Sci U S A **79**(4): 1129-1133.

Alon, U. (2007). An introduction to systems biology : design principles of biological circuits. Boca Raton, FL, Chapman & Hall/CRC.

Ando, N., S. Emoto, et al. (2013). "Odour-tracking capability of a silkmoth driving a mobile robot with turning bias and time delay." Bioinspir Biomim **8**(1): 016008.

Armstrong, C. M. (1981). "Sodium channels and gating currents." Physiological reviews **61**(3): 644-683.

Asahina, K., M. Louis, et al. (2009). "A circuit supporting concentration-invariant odor perception in Drosophila." J Biol **8**(1): 9.

Bargmann, C. I. (2006). "Comparative chemosensation from receptors to ecology." Nature **444**(7117): 295-301.

Barkai, N. and S. Leibler (1997). "Robustness in simple biochemical networks." Nature **387**(6636): 913-917.

Barlow, H. and W. Levick (1969). "Changes in the maintained discharge with adaptation level in the cat retina." The Journal of physiology **202**(3): 699-718.

Bathellier, B., O. Gschwend, and A. Carleton (2010). "Temporal coding in olfaction."

Beckingham, K. M., M. J. Texada, et al. (2005). "Genetics of Graviperception in Animals." Adv Genet **55**: 105-145.

Bellen, H. J., Tong, C., & Tsuda, H. (2010). "Bellen, Hugo J., Chao Tong, and Hiroshi Tsuda. "100 years of Drosophila research and its impact on vertebrate neuroscience: a history lesson for the future." Nature Reviews Neuroscience **11**(7): 514-522.

Bellmann, D., A. Richardt, et al. (2010). "Optogenetically Induced Olfactory Stimulation in Drosophila Larvae Reveals the Neuronal Basis of Odor-Aversion behavior." Front Behav Neurosci **4**: 27.

Benton, R., S. Sachse, et al. (2006). "Atypical Membrane Topology and Heteromeric Function of <italic>Drosophila</italic> Odorant Receptors In Vivo." PLoS Biol **4**(2): e20.

Benton, R., S. Sachse, et al. (2006). "Atypical membrane topology and heteromeric function of Drosophila odorant receptors in vivo." PLoS Biol **4**(2): e20.

Berg, H. C., and Douglas A. Brown (1972). "Chemotaxis in Escherichia coli analysed by three-dimensional tracking." Nature **239**(5374): 500-504.

Berndt, A., P. Schoenenberger, et al. (2011). "High-efficiency channelrhodopsins for fast neuronal stimulation at low light levels." Proc Natl Acad Sci U S A **108**(18): 7595-7600.

Berndt, D. J. and J. Clifford (1994). "Using Dynamic Time Warping to Find Patterns in Time Series." KDD workshop **10**(6).

Berridge, M. (1995). "Capacitative calcium entry." Biochem. j **312**: 1-11.

Bhandawat, V., Johannes Reisert, and King-Wai Yau (2005). "Elementary response of olfactory receptor neurons to odorants." Science **308**(5730): 1931-1934.

Bintu, L., N. E. Buchler, et al. (2005). "Transcriptional regulation by the numbers: models." Curr Opin Genet Dev **15**(2): 116-124.

Borst, A., and Martin Heisenberg (1982). "Osmotropotaxis inDrosophila melanogaster." Journal of comparative physiology **147**(4): 479-484.

Borst, A. a. H., M. (1982). "Osmotropotaxis in Drosophila Melanogaster." Journal of Comparative Physiology A: Neuroethology, Sensory, Neural, and Behavioral Physiology **147**(4): 479-484.

Brand, A. H., and Norbert Perrimon (1993). " Targeted gene expression as a means of altering cell fates and generating dominant phenotypes." Development **118**(2): 401-415.

Brenner, N., W. Bialek, et al. (2000). "Adaptive rescaling maximizes information transmission." Neuron **26**(3): 695-702.

Brun, R. and F. Rademakers (1997). "ROOT—an object oriented data analysis framework." Nuclear Instruments and Methods in Physics

Research Section A: Accelerators, Spectrometers, Detectors and Associated Equipment **389**(1): 81-86.

Butts DA, G. M. (2006). "Tuning Curves, Neuronal Variability, and Sensory Coding." PLoS Biology **4**(4).

Cachero, S. and G. S. Jefferis (2008). "Drosophila olfaction: the end of stereotypy?" Neuron **59**(6): 843-845.

Chalasani, S. H., N. Chronis, et al. (2007). "Dissecting a circuit for olfactory behaviour in Caenorhabditis elegans." Nature **450**(7166): 63-70.

Chichilnisky, E. J. (2001). "A simple white noise analysis of neuronal light responses." Network **12**(2): 199-213.

Chu, I. W. and R. C. Axtell (1971). "Fine structure of the dorsal organ of the house fly larva, Musca domestica L." Zeitschrift für Zellforschung und Mikroskopische Anatomie **117**(1): 17-34.

Clapham, D. E. (2003). "TRP channels as cellular sensors." Nature **426**(6966): 517-524.

Cobb, M. (1999). "What and how do maggots smell?" Biological Reviews **74**(4): 425-459.

Cotterell, J. and J. Sharpe (2010). "An atlas of gene regulatory networks reveals multiple three-gene mechanisms for interpreting morphogen gradients." Mol Syst Biol **6**: 425.

Csete, M. E., and John C. Doyle (2002). "Reverse engineering of biological complexity." Science **295**(5560): 1664-1669.

Das, A., T. Gupta, et al. (2013). "Neuroblast lineage-specific origin of the neurons of the Drosophila larval olfactory system." Dev Biol **373**(2): 322-337.

Das, A., T. Gupta, et al. (2013). "Neuroblast lineage-specific origin of the neurons of the Drosophila larval olfactory system." Dev Biol **373**(2): 322-337.

Das, A., S. Sen, et al. (2008). "Drosophila olfactory local interneurons and projection neurons derive from a common neuroblast lineage specified by the empty spiracles gene." Neural Dev **3**: 33.

Deng, Y., W. Zhang, et al. (2011). "The stimulatory Galpha(s) protein is involved in olfactory signal transduction in Drosophila." PLoS One **6**(4): e18605.

Deshpande, M., Venkatesh, K., Rodrigues, V., & Hasan, G. (2000). "The inositol 1, 4, 5-trisphosphate receptor is required for maintenance of olfactory adaptation in Drosophila antennae." Journal of neurobiology **43**(3): 282-288.

Dugue, G. P., W. Akemann, et al. (2012). "A comprehensive concept of optogenetics." Prog Brain Res **196**: 1-28.

Dunn, N. A., J. S. Conery, et al. (2007). "Circuit motifs for spatial orientation behaviors identified by neural network optimization." J Neurophysiol **98**(2): 888-897.

Eschbach, C., C. Cano, et al. (2011). "Associative learning between odorants and mechanosensory punishment in larval Drosophila." J Exp Biol **214**(Pt 23): 3897-3905.

Fairhall, A. L., G. D. Lewen, et al. (2001). "Efficiency and ambiguity in an adaptive neural code." Nature **412**(6849): 787-792.

Fancher, R. E. and A. Rutherford (2012). "'The Sensing and Perceiving Mind.' Pioneers of Psychology." New York: W.W. Norton: 167-171.

Faumont, S., G. Rondeau, et al. (2011). "An image-free opto-mechanical system for creating virtual environments and imaging neuronal activity in freely moving Caenorhabditis elegans." PLoS One **6**(9): e24666.

Fishilevich, E., A. I. Domingos, et al. (2005). "Chemotaxis behavior mediated by single larval olfactory neurons in Drosophila." Curr Biol **15**(23): 2086-2096.

Freeman, W. H. (2006). "Infrared Spectroscopy, chapter 16

French, A. S., P. H. Torkkeli, et al. (2011). "Dynamic characterization of Drosophila antennal olfactory neurons indicates multiple opponent signaling pathways in odor discrimination." J Neurosci **31**(3): 861-869.

Frey, B. J. and D. Dueck (2007). "Clustering by passing messages between data points." Science **315**(5814): 972-976.

Fry, S. N., N. Rohrseitz, et al. (2008). "TrackFly: virtual reality for a behavioral system analysis in free-flying fruit flies." J Neurosci Methods **171**(1): 110-117.

Fujiwara, T., T. Kazawa, et al. (2014). "Odorant concentration differentiator for intermittent olfactory signals." J Neurosci **34**(50): 16581-16593.

Galili, D. S., A. Ludke, et al. (2011). "Olfactory trace conditioning in Drosophila." J Neurosci **31**(20): 7240-7248.

Gaudry, Q., E. J. Hong, et al. (2013). "Asymmetric neurotransmitter release enables rapid odour lateralization in Drosophila." Nature **493**(7432): 424-428.

Gepner, R., M. M. Skanata, et al. (2015). "Computations underlying Drosophila photo-taxis, odor-taxis, and multi-sensory integration." Elife: e06229.

Gerber, B. and R. F. Stocker (2007). "The Drosophila larva as a model for studying chemosensation and chemosensory learning: a review." Chem Senses **32**(1): 65-89.

Gershow, M., M. Berck, et al. (2012). "Controlling airborne cues to study small animal navigation." Nat Methods **9**(3): 290-296.

Goentoro, L. and M. W. Kirschner (2009). "Evidence that fold-change, and not absolute level, of beta-catenin dictates Wnt signaling." Mol Cell **36**(5): 872-884.

Gomez-Marin, A., B. J. Duistermars, et al. (2010). "Mechanisms of odor-tracking: multiple sensors for enhanced perception and behavior." Front Cell Neurosci **4**: 6.

Gomez-Marin, A. and M. Louis (2012). "Active sensation during orientation behavior in the Drosophila larva: more sense than luck." Curr Opin Neurobiol **22**(2): 208-215.

Gomez-Marin, A. and M. Louis (2014). "Multilevel control of run orientation in Drosophila larval chemotaxis." Front Behav Neurosci **8**: 38.

Gomez-Marin, A., N. Partoune, et al. (2012). "Automated tracking of animal posture and movement during exploration and sensory orientation behaviors." PLoS One **7**(8): e41642.

Gomez-Marin, A., G. J. Stephens, et al. (2011). "Active sampling and decision making in Drosophila chemotaxis." Nat Commun **2**: 441.

Grant, A. J., and Robert J. O'Connell (1996). "Electrophysiological responses from receptor neurons in mosquito maxillary palp sensilla." Olfaction in Mosquito-Host Interactions: 233-253.

Grasso, F. W., T. R. Consi, et al. (2000). "Biomimetic robot lobster performs chemo-orientation in turbulence using a pair of spatially

separated sensors: Progress and challenges." Robotics and Autonomous Systems **30**(1): 115-131.

Gu, Y., P. Lucas, et al. (2009). "Computational model of the insect pheromone transduction cascade." PLoS Computational Biology **5**(3): e1000321.

Haining, W. N., Carboy-Newcomb, C., Wei, C. L., and Steller, H. (1999). "The proapoptotic function of Drosophila Hid is conserved in mammalian cells." Proceedings of the National Academy of Sciences **96**(9): 4936-4941.

Hallem, E. A. and J. R. Carlson (2004). "The odor coding system of Drosophila." Trends Genet **20**(9): 453-459.

Hallem, E. A. and J. R. Carlson (2006). "Coding of odors by a receptor repertoire." Cell **125**(1): 143-160.

Herculano-Houzel, S. (2009). " The Human Brain in Numbers: A Linearly Scaled-up Primate Brain." Frontiers in Human Neuroscience **3**(31).

Herculano-Houzel, S., K. Avelino-de-Souza, et al. (2014). "The elephant brain in numbers." Front Neuroanat **8**: 46.

Hildebrand, J. G. and G. M. Shepherd (1997). "Mechanisms of olfactory discrimination: converging evidence for common principles across phyla." Annual review of neuroscience **20**(1): 595-631.

Hill, R. W., G. A. Wyse, et al. (2012). Animal Physiology, Sinauer Associates, Incorporated Publishers.

Hille, B. (2001). Ion channels of excitable membranes, Sinauer Sunderland, MA.

Hoare, D. J., J. Humble, et al. (2011). "Modeling peripheral olfactory coding in Drosophila larvae." PLoS One **6**(8): e22996.

Hoare, D. J., C. R. McCrohan, et al. (2008). "Precise and fuzzy coding by olfactory sensory neurons." J Neurosci **28**(39): 9710-9722.

Hodgkin, A. L. and A. F. Huxley (1952). "A quantitative description of membrane current and its application to conduction and excitation in nerve." The Journal of physiology **117**(4): 500-544.

Honda, T., C. Y. Lee, et al. (2014). "Induction of associative olfactory memory by targeted activation of single olfactory neurons in Drosophila larvae." Sci Rep **4**: 4798.

Hopfield, J. J. (1995). "Pattern recognition computation using action potential timing for stimulus representation." Nature **376**(6535): 33-36.

Huston, S. J. and V. Jayaraman (2011). "Studying sensorimotor integration in insects." Curr Opin Neurobiol **21**(4): 527-534.

Iino, Y. and K. Yoshida (2009). "Parallel use of two behavioral mechanisms for chemotaxis in Caenorhabditis elegans." J Neurosci **29**(17): 5370-5380.

Isaacson, J. S. and M. Scanziani (2011). "How inhibition shapes cortical activity." Neuron **72**(2): 231-243.

Izhikevich, E. M. (2007). "Dynamical systems in neuroscience." MIT press.

Izquierdo, E. J. and S. R. Lockery (2010). "Evolution and analysis of minimal neural circuits for klinotaxis in Caenorhabditis elegans." J Neurosci **30**(39): 12908-12917.

Jan, L. Y. and Y. N. Jan (1989). "Voltage-sensitive ion channels." Cell **56**(1): 13-25.

Jan, L. Y. and Y. N. Jan (1992). "Structural elements involved in specific K+ channel functions." Annual review of physiology **54**(1): 537-555.

Jenett, A., G. M. Rubin, et al. (2012). "A GAL4-driver line resource for Drosophila neurobiology." Cell Rep **2**(4): 991-1001.

Jiang, Y., A. Lee, et al. (2002). "Crystal structure and mechanism of a calcium-gated potassium channel." Nature **417**(6888): 515-522.

Kaiser, M., C. C. Hilgetag, et al. (2010). "Hierarchy and dynamics of neural networks." Front Neuroinform **4**.

Kane, E. A., M. Gershow, et al. (2013). "Sensorimotor structure of Drosophila larva phototaxis." Proc Natl Acad Sci U S A **110**(40): E3868-3877.

Kato, H. E., F. Zhang, et al. (2012). "Crystal structure of the channelrhodopsin light-gated cation channel." Nature **482**(7385): 369-374.

Kato, S., Y. Xu, et al. (2014). "Temporal responses of C. elegans chemosensory neurons are preserved in behavioral dynamics." Neuron **81**(3): 616-628.

Kelly-Zion, P., C. Pursell, et al. (2011). "Evaporation of sessile drops under combined diffusion and natural convection." Colloids and Surfaces A: Physicochemical and Engineering Aspects **381**(1): 31-36.

Kendeigh, S. C. (1961). "Animal ecology." Animal ecology.

Kim, A. J., A. A. Lazar, et al. (2011). "System identification of Drosophila olfactory sensory neurons." J Comput Neurosci **30**(1): 143-161.

Kim, A. J., A. A. Lazar, et al. (2015). "Projection neurons in Drosophila antennal lobes signal the acceleration of odor concentrations." Elife: e06651.

Klein, M., B. Afonso, et al. (2015). "Sensory determinants of behavioral dynamics in Drosophila thermotaxis." Proc Natl Acad Sci U S A **112**(2): E220-229.

Kocabas, A., C. H. Shen, et al. (2012). "Controlling interneuron activity in Caenorhabditis elegans to evoke chemotactic behaviour." Nature **490**(7419): 273-277.

Kreher, S. A., J. Y. Kwon, et al. (2005). "The molecular basis of odor coding in the Drosophila larva." Neuron **46**(3): 445-456.

Kreher, S. A., D. Mathew, et al. (2008). "Translation of sensory input into behavioral output via an olfactory system." Neuron **59**(1): 110-124.

Kwon, Y., H. S. Shim, et al. (2008). "Control of thermotactic behavior via coupling of a TRP channel to a phospholipase C signaling cascade." Nat Neurosci **11**(8): 871-873.

Larkin, A., S. Karak, et al. (2010). "Central synaptic mechanisms underlie short-term olfactory habituation in Drosophila larvae." Learn Mem **17**(12): 645-653.

Larsson, M. C., A. I. Domingos, et al. (2004). "Or83b encodes a broadly expressed odorant receptor essential for Drosophila olfaction." Neuron **43**(5): 703-714.

Lazova, M. D., Ahmed, T., Bellomo, D., Stocker, R., & Shimizu, T. S. (2011). "Response rescaling in bacterial chemotaxis." Proceedings of the National Academy of Sciences **108**(33): 13870-13875.

Lecar, H. and R. Nossal (1971). "Theory of threshold fluctuations in nerves: I. Relationships between electrical noise and fluctuations in axon firing." Biophys J **11**(12): 1048.

Lecar, H. and R. Nossal (1971). "Theory of threshold fluctuations in nerves: II. Analysis of various sources of membrane noise." Biophys J **11**(12): 1068-1084.

Leinders-Zufall, T., C. A. Greer, et al. (1998). "Imaging odor-induced calcium transients in single olfactory cilia: specificity of activation and role in transduction." The journal of neuroscience **18**(15): 5630-5639.

Leinders-Zufall, T., Minghong Ma, and Frank Zufall (1999). "Impaired odor adaptation in olfactory receptor neurons after inhibition of Ca2+/calmodulin kinase II." The Journal of neuroscience: the official journal of the Society for Neuroscience **19**(14): RC19-RC19.

Leinders-Zufall, T., M. N. Rand, et al. (1997). "Calcium entry through cyclic nucleotide-gated channels in individual cilia of olfactory receptor cells: spatiotemporal dynamics." The journal of neuroscience **17**(11): 4136-4148.

Lim, W. A., C. M. Lee, et al. (2013). "Design principles of regulatory networks: searching for the molecular algorithms of the cell." Mol Cell **49**(2): 202-212.

Lin, J. Y. (2011). "A user's guide to channelrhodopsin variants: features, limitations and future developments." Exp Physiol **96**(1): 19-25.

Liu, W. W., and Rachel I. Wilson (2013). "Glutamate is an inhibitory neurotransmitter in the Drosophila olfactory system." Proceedings of the National Academy of Sciences **110**(25): 10294-10299.

Lockery, S. R. (2011). "The computational worm: spatial orientation and its neuronal basis in C. elegans." Curr Opin Neurobiol.

Lockery, S. R. (2011). "The computational worm: spatial orientation and its neuronal basis in C. elegans." Curr Opin Neurobiol **21**(5): 782-790.

Long, S. B., X. Tao, et al. (2007). "Atomic structure of a voltage-dependent K+ channel in a lipid membrane-like environment." Nature **450**(7168): 376-382.

Lott III, G. K., Johnson, B. R., Bonow, R. H., Land, B. R., & Hoy, R. R. (2009). "g-PRIME: a free, Windows based data acquisition and event analysis software package for physiology in classrooms and research labs." Journal of Undergraduate Neuroscience Education **8**(1): A50.

Louis, M., T. Huber, et al. (2008). "Bilateral olfactory sensory input enhances chemotaxis behavior." Nat Neurosci **11**(2): 187-199.

Louis, M., M. Phillips, et al. (2012). Behavioral Analysis of Navigation Behaviors in the Drosophila Larva. The Making and Un-Making of Neuronal Circuits in Drosophila, Springer**:** 163-199.

Lundin, C., L. Käll, et al. (2007). "Membrane topology of the Drosophila OR83b odorant receptor." FEBS letters **581**(29): 5601-5604.

Luo, L., E. M. Callaway, et al. (2008). "Genetic dissection of neural circuits." Neuron **57**(5): 634-660.

Luo, L., Q. Wen, et al. (2014). "Dynamic encoding of perception, memory, and movement in a C. elegans chemotaxis circuit." Neuron **82**(5): 1115-1128.

Luo, S. X., R. Axel, et al. (2010). "Generating sparse and selective third-order responses in the olfactory system of the fly." Proc Natl Acad Sci U S A **107**(23): 10713-10718.

Mahr, A. and H. Aberle (2006). "The expression pattern of the Drosophila vesicular glutamate transporter: a marker protein for motoneurons and glutamatergic centers in the brain." Gene Expr Patterns **6**(3): 299-309.

Malnic, B. and J. Hirono, Sato, T., & Buck, L. B. (1999). "Combinatorial receptor codes for odors." Cell **96**(5): 713-723.

Marella, S., K. Mann, et al. (2012). "Dopaminergic modulation of sucrose acceptance behavior in Drosophila." Neuron **73**(5): 941-950.

Marin, E. C., Jefferis, G. S., Komiyama, T., Zhu, H., & Luo, L. (2002). "Representation of the Glomerular Olfactory Map in the Drosophila Brain." Cell **109**(2): 243-255.

Martelli, C., J. R. Carlson, et al. (2013). "Intensity invariant dynamics and odor-specific latencies in olfactory receptor neuron response." J Neurosci **33**(15): 6285-6297.

Martin, F., and Esther Alcorta (2011). "Regulation of olfactory transduction in the Orco channel." Frontiers in cellular neuroscience **5**: 21-21.

Martinez, W. L. and A. R. Martinez (2001). Computational statistics handbook with MATLAB, CRC press.

Masse, N. Y., G. C. Turner, et al. (2009). "Olfactory information processing in Drosophila." Curr Biol **19**(16): R700-713.

Masuda-Nakagawa, L. M., N. Gendre, et al. (2009). "Localized olfactory representation in mushroom bodies of Drosophila larvae." Proc Natl Acad Sci U S A **106**(25): 10314-10319.

Mathew, D., C. Martelli, et al. (2013). "Functional diversity among sensory receptors in a Drosophila olfactory circuit." Proc Natl Acad Sci U S A **110**(23): E2134-2143.

Matthews, H. R. and J. Reisert (2003). "Calcium, the two-faced messenger of olfactory transduction and adaptation." Current Opinion in Neurobiology **13**(4): 469-475.

Meister, M. and M. J. Berry (1999). "The neural code of the retina." Neuron **22**(3): 435-450.

Milo, R., S. Shen-Orr, et al. (2002). "Network motifs: simple building blocks of complex networks." Science **298**(5594): 824-827.

Moses, K., M. C. Ellis, et al. (1989). "The glass gene encodes a zinc-finger protein required by Drosophila photoreceptor cells." Nature **340**(6234): 531-536.

Muller, M., C. Bamann, et al. (2011). "Projection structure of channelrhodopsin-2 at 6 A resolution by electron crystallography." J Mol Biol **414**(1): 86-95.

Munger, S. D., A. P. Lane, et al. (2001). "Central role of the CNGA4 channel subunit in Ca2+-calmodulin-dependent odor adaptation." Science **294**(5549): 2172-2175.

Murmu, M. S., J. Stinnakre, et al. (2010). "Presynaptic Ca2+ stores contribute to odor-induced responses in Drosophila olfactory receptor neurons." J Exp Biol **213**(Pt 24): 4163-4173.

Myers, R. H., D. C. Montgomery, et al. (2002). Generalized linear models : with applications in engineering and the sciences. New York, J. Wiley.

Nagel, G., M. Brauner, et al. (2005). "Light activation of channelrhodopsin-2 in excitable cells of Caenorhabditis elegans triggers rapid behavioral responses." Curr Biol **15**(24): 2279-2284.

Nagel, G., T. Szellas, et al. (2003). "Channelrhodopsin-2, a directly light-gated cation-selective membrane channel." Proc Natl Acad Sci U S A **100**(24): 13940-13945.

Nagel, K. I. and R. I. Wilson (2011). "Biophysical mechanisms underlying olfactory receptor neuron dynamics." Nat Neurosci **14**(2): 208-216.

Nakagawa, T., M. Pellegrino, et al. (2012). "Amino acid residues contributing to function of the heteromeric insect olfactory receptor complex." PLoS One **7**(3): e32372.

Nakagawa, T. and L. B. Vosshall (2009). "Controversy and consensus: noncanonical signaling mechanisms in the insect olfactory system." Curr Opin Neurobiol **19**(3): 284-292.

Nassif, C., A. Noveen, et al. (2003). "Early development of the Drosophila brain: III. The pattern of neuropile founder tracts during the larval period." J Comp Neurol **455**(4): 417-434.

Nelder, J. A. and R. Mead (1965). "A simplex method for function minimization." The computer journal **7**(4): 308-313.

Nichols, A. S., S. Chen, et al. (2011). "Subunit contributions to insect olfactory receptor function: channel block and odorant recognition." Chem Senses **36**(9): 781-790.

Nolte, A., Funk, N. W., Mukunda, L., Gawalek, P., Werckenthin, A., Hansson, B. S., ... & Stengl, M. (2013). "In situ tip-recordings found no evidence for an Orco-based ionotropic mechanism of pheromone-transduction in Manduca sexta." PLoS One **8**(5): e62648.

Ohashi, S., T. Morimoto, et al. (2014). "A novel behavioral strategy, continuous biased running, during chemotaxis in Drosophila larvae." Neurosci Lett **570**: 10-15.

Ohyama, T., T. Jovanic, et al. (2013). "High-throughput analysis of stimulus-evoked behaviors in Drosophila larva reveals multiple modality-specific escape strategies." PLoS One **8**(8): e71706.

Oppliger, F. Y., M. G. P, et al. (2000). "Neurophysiological and behavioural evidence for an olfactory function for the dorsal organ and a gustatory one for the terminal organ in Drosophila melanogaster larvae." J Insect Physiol **46**(2): 135-144.

Panzeri, S., N. Brunel, et al. (2010). "Sensory neural codes using multiplexed temporal scales." Trends Neurosci **33**(3): 111-120.

Pask, G. M., P. L. Jones, et al. (2011). "Heteromeric anopheline odorant receptors exhibit distinct channel properties." PLoS One **6**(12): e28774.

Pauls, D., M. Selcho, et al. (2010). "Drosophila larvae establish appetitive olfactory memories via mushroom body neurons of embryonic origin." J Neurosci **30**(32): 10655-10666.

Pellegrino, M., T. Nakagawa, et al. (2010). "Single sensillum recordings in the insects Drosophila melanogaster and Anopheles gambiae." J Vis Exp(36): 1-5.

Pfeiffer, B. D., J. W. Truman, et al. (2012). "Using translational enhancers to increase transgene expression in Drosophila." Proc Natl Acad Sci U S A **109**(17): 6626-6631.

Pierce-Shimomura, J. T., Thomas M. Morse, and Shawn R. Lockery (1999). "The fundamental role of pirouettes in Caenorhabditis elegans chemotaxis." The journal of neuroscience **19**(21): 9557-9569.

Press, W. H., Flannery, B. P., Teukolsky, S. A., and Vetterling, W. T. (1988). "14.8 Savitzky-Golay Smoothing Filters,". Numerical Recipes in C: The Art of Scientific Computing." Cambridge University Press 1992 **1992**: 650-655.

Prinz, A. A., D. Bucher, et al. (2004). "Similar network activity from disparate circuit parameters." Nat Neurosci **7**(12): 1345-1352.

Pulver, S. R., S. L. Pashkovski, et al. (2009). "Temporal dynamics of neuronal activation by Channelrhodopsin-2 and TRPA1 determine behavioral output in Drosophila larvae." J Neurophysiol **101**(6): 3075-3088.

Python, F. and R. F. Stocker (2002). "Adult-like complexity of the larval antennal lobe of D. melanogaster despite markedly low numbers of odorant receptor neurons." J Comp Neurol **445**(4): 374-387.

Ramaekers, A., E. Magnenat, et al. (2005). "Glomerular maps without cellular redundancy at successive levels of the Drosophila larval olfactory circuit." Curr Biol **15**(11): 982-992.

Restifo, L. L. and K. White (1990). "Molecular and Genetic Approaches to Neurotransmitter and Neuromodulator Systems in Drosophila." **22**: 115-219.

Rieke, F. (1997). Spikes : exploring the neural code. Cambridge, Mass., MIT Press.

Ruta, V., S. R. Datta, et al. (2010). "A dimorphic pheromone circuit in Drosophila from sensory input to descending output." Nature **468**(7324): 686-690.

Ryan, T. J. and S. G. Grant (2009). "The origin and evolution of synapses." Nat Rev Neurosci **10**(10): 701-712.

Sato, K., M. Pellegrino, et al. (2008). "Insect olfactory receptors are heteromeric ligand-gated ion channels." Nature **452**(7190): 1002-1006.

Sattig, T., Rickert, C., Bamberg, E., Steinhoff, H. J., & Bamann, C. (2013). "Inside Cover: Light-Induced Movement of the Transmembrane Helix B in Channelrhodopsin-2." Angewandte Chemie International Edition **52**(37): 9586-9586.

Sawin-McCormack, E. P., M. B. Sokolowski, et al. (1995). "Characterization and genetic analysis of Drosophila melanogaster photobehavior during larval development." J Neurogenet **10**(2): 119-135.

Schafer, R. W. (2011). "What is a savitzky-golay filter? [lecture notes]." Signal Processing Magazine, IEEE **28**(4): 111-117.

Schoenenberger, P., Y. P. Scharer, et al. (2011). "Channelrhodopsin as a tool to investigate synaptic transmission and plasticity." Exp Physiol **96**(1): 34-39.

Schroll, C., T. Riemensperger, et al. (2006). "Light-induced activation of distinct modulatory neurons triggers appetitive or aversive learning in Drosophila larvae." Curr Biol **16**(17): 1741-1747.

Shang, Y., A. Claridge-Chang, et al. (2007). "Excitatory local circuits and their implications for olfactory processing in the fly antennal lobe." Cell **128**(3): 601-612.

Shimizu, T. S., Y. Tu, et al. (2010). "A modular gradient-sensing network for chemotaxis in Escherichia coli revealed by responses to time-varying stimuli." Mol Syst Biol **6**: 382.

Shirsat, N. and O. Siddiqi (1993). "Olfaction in invertebrates." Current Opinion in Neurobiology **3**(4): 553-557.

Shoval, O., L. Goentoro, et al. (2010). "Fold-change detection and scalar symmetry of sensory input fields." Proc Natl Acad Sci U S A **107**(36): 15995-16000.

Shusterman, R., M. C. Smear, et al. (2011). "Precise olfactory responses tile the sniff cycle." Nat Neurosci **14**(8): 1039-1044.

Singh, R. N., and Kusum Singh (1984). "Fine structure of the sensory organs of Drosophila melanogaster Meigen larva (Diptera: Drosophilidae)." International Journal of Insect Morphology and Embryology **13**(4): 255-273.

Singleton, K. and R. I. Woodruff (1994). "The osmolarity of adult Drosophila hemolymph and its effect on oocyte-nurse cell electrical polarity." Developmental biology **161**(1): 154-167.

Song, Z., M. Postma, et al. (2012). "Stochastic, adaptive sampling of information by microvilli in fly photoreceptors." Curr Biol **22**(15): 1371-1380.

Sporns, O. (2006). "Small-world connectivity, motif composition, and complexity of fractal neuronal connections." Biosystems **85**(1): 55-64.

Steinbrecht, R. A. (1997). "Pore structures in insect olfactory sensilla: a review of data and concepts." International Journal of Insect Morphology and Embryology **26**(3): 229-245.

Stengl, M. (1994). "Inositol-trisphosphate-dependent calcium currents precede cation currents in insect olfactory receptor neurons in vitro." Journal of Comparative Physiology A **174**(2): 187-194.

Stengl, M. and N. W. Funk (2013). "The role of the coreceptor Orco in insect olfactory transduction." J Comp Physiol A Neuroethol Sens Neural Behav Physiol **199**(11): 897-909.

Stephenson, R. and N. H. Metcalfe (2013). "Drosophila melanogaster: a fly through its history and current use." J R Coll Physicians Edinb **43**(1): 70-75.

Stocker, R. F. (1994). "The organization of the chemosensory system in Drosophila melanogaster: a rewiew." Cell and tissue research **275**(1): 3-26.

Stocker, R. F. (2008). "Design of the larval chemosensory system." Springer New York: 69-81.

Swinehart, D. F. (1962). "The Beer-Lambert Law." Journal of Chemical Education **39**: 333.

Szyszka, P., R. C. Gerkin, et al. (2014). "High-speed odor transduction and pulse tracking by insect olfactory receptor neurons." Proc Natl Acad Sci U S A **111**(47): 16925-16930.

Tichy, H., A. Hinterwirth, et al. (2005). "Olfactory receptors on the cockroach antenna signal odour ON and odour OFF by excitation." Eur J Neurosci **22**(12): 3147-3160.

Tkačik, G. and W. Bialek (2014). "Information processing in living systems." arXiv preprint arXiv:1412.8752.

Tu, Y., T. S. Shimizu, et al. (2008). "Modeling the chemotactic response of Escherichia coli to time-varying stimuli." Proc Natl Acad Sci U S A **105**(39): 14855-14860.

Vetter, R. S., A. E. Sage, et al. (2006). "Temporal integrity of an airborne odor stimulus is greatly affected by physical aspects of the odor delivery system." Chem Senses **31**(4): 359-369.

Vogelstein, J. T., Y. Park, et al. (2014). "Discovery of brainwide neural-behavioral maps via multiscale unsupervised structure learning." Science **344**(6182): 386-392.

Voytek, B. (2013). "Are There Really as Many Neurons in the Human Brain as Stars in the Milky Way?" Scitable (Nature Education).

Waldmann, R., Champigny, G., Bassilana, F., Heurteaux, C., and Lazdunski, M. (1997). "A proton-gated cation channel involved in acid-sensing." Nature **386**(173–177).

Webb, B. (2002). "Robots in invertebrate neuroscience." Nature **417**(6886): 359-363.

Wessnitzer, J., J. M. Young, et al. (2012). "A model of non-elemental olfactory learning in Drosophila." J Comput Neurosci **32**(2): 197-212.

Wicher, D. (2010). "Design principles of sensory receptors." Front Cell Neurosci **4**.

Wicher, D. (2013). "Sensory receptors—design principles revisited." Frontiers in Cellular Neuroscience **7**: 1.

Wicher, D., R. Schäfer, et al. (2008). "Drosophila odorant receptors are both ligand-gated and cyclic-nucleotide-activated cation channels." Nature **452**(7190): 1007-1011.

Wilson, R. I. (2013). "Early olfactory processing in Drosophila: mechanisms and principles." Annu Rev Neurosci **36**: 217-241.

Wilson, R. I. and Z. F. Mainen (2006). "Early events in olfactory processing." Annual review of neuroscience **29**: 163-201.

Xiang, Y., Q. Yuan, et al. (2010). "Light-avoidance-mediating photoreceptors tile the Drosophila larval body wall." Nature **468**(7326): 921-926.

Yaksi, E. and R. I. Wilson (2010). "Electrical coupling between olfactory glomeruli." Neuron **67**(6): 1034-1047.

Yao, Z., A. M. Macara, et al. (2012). "Analysis of functional neuronal connectivity in the Drosophila brain." J Neurophysiol **108**(2): 684-696.

Yau, K. W. and R. C. Hardie (2009). "Phototransduction motifs and variations." Cell **139**(2): 246-264.

Yi, T. M., Y. Huang, et al. (2000). "Robust perfect adaptation in bacterial chemotaxis through integral feedback control." Proc Natl Acad Sci U S A **97**(9): 4649-4653.

Yizhar, O., L. E. Fenno, et al. (2011). "Optogenetics in neural systems." Neuron **71**(1): 9-34.

Zufall, F. and T. Leinders-Zufall (2000). "The cellular and molecular basis of odor adaptation." Chem Senses **25**(4): 473-481.

Appendix

Contains the reference and link to the article that resulted from the presented work:

Schulze, A., Gomez-Marin, A., Rajendran, V. G., Lott, G., Musy, M., Ahammad, P., Deogade, A., Sharpe J., Riedl , J., Jarriault, D., Trautman, E. T., Werner, C., Venkadesan, M., Druckmann, S., Jayaraman, V. & Louis, M. (2015). Dynamical feature extraction at the sensory periphery guides chemotaxis. *eLife*, *4*, e06694.